

A thermal simulation tool for CubeSats for dynamic in-orbit scenarios, verified with flight data from the nSight-1 mission.

by
Mr. Mike-Alec Kearney

Thesis presented in partial fulfilment of the requirements for the degree of Master of Engineering (Mechanical) in the Faculty of Engineering at Stellenbosch University



Supervisor: Prof Gerhard Venter
Co-supervisor: Mr Robert Dobson

March 2020

Declaration

By submitting this thesis electronically, I declare that the entirety of the work contained therein is my own, original work, that I am the sole author thereof (save to the extent explicitly otherwise stated), that reproduction and publication thereof by Stellenbosch University will not infringe any third party rights and that I have not previously in its entirety or in part submitted it for obtaining any qualification.

Mike-Alec Kearney

March 2020

Copyright © 2020 Stellenbosch University

All rights reserved

Abstract

Thermal analysis is one of the aspects of designing CubeSats that has historically received less attention than more directly mission critical aspects such as power and communications budgets, and attitude control performance. The reasons for this neglect are partly due to the complexities of doing detailed thermal analyses, and partly because of the high cost of thermal simulation software that is tailored for the unique environment of space. Typically, CubeSat teams will do simplified steady state thermal analyses for a particular satellite orientation and particular orbit. However, these analyses generally only account for the original orbit a satellite is launched in, which proves problematic. Given the fact that much of these orbits are not Sun-synchronous, and that in Low Earth Orbit (LEO) these orbits decay rapidly, these simplified analyses are only valid for a small portion of the satellite's mission lifetime.

With this in mind, this study created a method to integrate a lumped-capacitance thermal model with a high accuracy Attitude Determination and Control System (ADCS) simulation program in order to simulate the temperature of a CubeSat for dynamic orientation and orbital scenarios. To supplement this simulation, a software tool was created to simplify the process of creating a numerical model of the surfaces of a satellite, which includes geometry, links between the surfaces and lumped thermal nodes, as well as the thermal properties of the surfaces.

The study discusses the key elements of the thermal environment in Space such as direct sunlight, reflected sunlight off of the Earth (albedo), Earth infrared (IR), as well as radiation to deep space. Ray tracing capability of the ADCS program is used to simulate shadowing of parts of the satellite by deployable solar panels. A method of calculating the view factor (VF) between surfaces of the satellite and the Earth is also discussed, since this has a significant effect on the heat transferred to a satellite with varying orientation.

The validity of the simulation was tested using a thermal model of the South African built satellite nSight-1, by comparing simulation outputs with in-orbit temperature measurements. The simulation tool was used to analyse the temperature of the nSight-1 subsystems for varying orbits, in order to identify problematic cases where subsystems exceed their maximum/minimum operational temperatures. Suggestions were then made for improvements to the thermal design in order to manage these problematic temperatures, and the suggested changes were simulated to verify their effects.

Opsomming

Termiese analise is een van die aspekte van die ontwerp van CubeSats wat histories minder aandag geniet as meer direkte, missie-kritieke aspekte, soos krag- en kommunikasie begrotings en orientasie beheer. Die redes hiervoor is deels as gevolg van die kompleksiteit van gedetailleerde termiese ontledings, en deels as gevolg van die hoë koste van sagteware vir termiese simulاسie wat spesifiek aangepas is vir die unieke ruimte-omgewing. Tipies doen CubeSat-spanne vereenvoudigde termiese ontledings vir 'n spesifieke satellietoriëntasie en 'n spesifieke wentelbaan. Hierdie ontledings word gewoonlik gedoen vir die oorspronklike wentelbaan waarin 'n satelliet gelanseer word. Aangesien baie van hierdie wentelbane nie son-sinkroon is nie, en lae-aard-wentelbane wentelbane vinnig verander as gevolg van aerodinamiese wrywing, is hierdie ontledings slegs geldig vir 'n klein deel van die satelliet leeftyd.

In hierdie studie is 'n metode geskep om 'n termiese model met 'n hoë akkuraatheid (ADCS) simulاسieprogram te integreer om die temperatuur van 'n CubeSat te simuleer vir dinamiese oriëntasie- en wentelbaan scenario's. Om hierdie simulاسie aan te vul, is 'n sagteware-instrument geskep om die proses om 'n numeriese model vir die oppervlaktes van 'n satelliet te skep, te vereenvoudig. Die program neem in ag meetkunde, skakels tussen die oppervlaktes en gekoppelde termiese elemente, asook die termiese eienskappe van die oppervlaktes.

Die studie bespreek die sleutelemente van die termiese omgewing in die ruimte, soos direkte sonlig, gereflekteerde sonlig van die Aarde (albedo), Aarde geradieerde infrarooi energie, sowel as straling na diep ruimte. Die “ray-tracing” vermoë van die ADCS-program word gebruik om die skadu van dele van die satelliet deur ontplooibare sonpanele te simuleer. 'n Metode om die sieningsfaktor tussen die oppervlaktes van die satelliet en die Aarde te bereken, word ook bespreek, aangesien dit 'n beduidende invloed het op die hitte wat na verskillende oppervlaktes van 'n satelliet oorgedra word.

Die simulاسie is getoets met 'n termiese model van 'n Suid-Afrikaans-geboude satelliet nSight-1, deur simulاسie-uitsette met in-wentelbaan temperatuurmetings te vergelyk. Die simulاسie-instrument word gebruik om die temperatuur van die nSight-1-substelsels vir verskillende wentelbane te bestudeer om problematiese gevalle te identifiseer waar substelsels hul maksimum / minimum operasionele temperatuur oorskry. Voorstelle word gemaak vir verbetering aan die termiese ontwerp om hierdie problematiese temperature te bestuur, en die voorgestelde veranderinge word gesimuleer om die effek daarvan te verifieer.

Acknowledgments

I would like to acknowledge the contributions of the South African companies, CubeSpace Satellite Systems and Space Commercial Services, for making data on the nSight-1 mission available for this study.

I would like to acknowledge the contributions of Mr R Dobson for his guidance, motivation and confidence in me.

I would like to thank Lourens Visagie for his unconditional support when it came to integrating my work with his ADCS software.

I would like to thank everyone in my life that supported me through this journey.

Dedication

I would like to dedicate this thesis to my parents:

Alexis Johan Kearney, who inspired me to be an engineer. He taught me to strive to understand the fundamentals of nature and the environment around me, and the value that this understanding has in everyday live.

“The older I get, the smarter my father seems to get”

- Tim Russert

Mariaan Suzette Kearney, who inspired me to always strive to be my best. She taught me the power of sheer will and determination, and she always believed that I could achieve whatever I put my mind to.

“Mother’s love is peace. It need not be acquired; it need not be deserved.”

- Erich Fromm

Table of Contents

1	Introduction.....	1
2	Literature Review	4
3	Theoretical Background and Definitions	7
3.1	Orbital and Attitude Dynamics.....	7
3.1.1	Coordinate Definitions	7
3.1.2	Attitude Format and Operation Mode Definitions	10
3.1.3	Satellite Orbital and Celestial Geometry.....	11
3.1.4	Celestial Equations.....	16
3.2	Heat Transfer	16
3.2.1	Radiation	16
3.2.2	Conduction	17
4	Heat Sources and Sinks.....	18
4.1	Direct Sunlight.....	18
4.2	Earth Albedo.....	19
4.3	Earth IR	23
4.4	Earth View Factor.....	24
4.5	Deep Space and Celestial Bodies	27
4.6	Electronic Heat Generation	29
4.6.1	Solar Panel Efficiency	30
4.6.2	Photo-voltaic Converter Efficiency.....	31
4.6.3	Battery Efficiency	31
4.6.4	Power Conditioning Efficiency	31
4.6.5	Sub-System Power Consumption.....	32
5	Satellite Thermal Model	35
5.1	Thermal Node and Resistance Definitions	35
5.2	Thermal Resistance Values	39
5.2.1	Structure	39
5.2.2	PCBs.....	43
5.2.3	Side Panels	46
5.2.4	Deployable Solar Panels	47

5.2.5	Deployable Magnetometer	48
5.2.6	Contact Resistance	49
5.3	Surface Properties.....	50
5.4	Surface Model	54
5.5	Thermal Resistance Matrix Construction.....	56
5.6	Temperature Solver	57
6	Simulation Results and In-Orbit Measurements.....	62
6.1	Description of Scenario	62
6.2	Comparison of Flight and Simulated Data	67
6.2.1	Battery	67
6.2.2	Computer/MCU.....	70
6.2.3	Deployable Magnetometer	72
6.3	Satellite Subsystem Temperature Ranges	73
6.4	Orbit Dependence of Satellite Temperatures	75
6.5	Necessity of Thermal Contact Resistances.....	77
6.6	Isolation of Electronics from Outside Panels	78
6.7	Better Connections between Deployables and Satellite Body	80
7	Discussion, Conclusions and Recommendations.....	82
	Appendix A: Thermal node and resistance listing	87
	Appendix B: Datasheet Extracts	94

List of Figures

Figure 1: nSight-1 Flight model pre-launch.....	2
Figure 2: Definition of the Vernal Equinox.....	8
Figure 3: J2000 ECI Frame.....	8
Figure 4: ORC Frame Definition.....	9
Figure 5: SBC Definition for nSight-1.....	9
Figure 6: RPY Definition.....	10
Figure 7: Y-Thomson Spin.....	11
Figure 8: Keplerian orbit parameters.....	12
Figure 9: Angle to local horizon in SBC.....	13
Figure 10: Sun β -Angle geometry.....	13
Figure 11: Sun path on spacecraft centered sphere.....	14
Figure 12: Solar Zenith-angle definition.....	15
Figure 13: Solar Zenith angle from Sun and satellite vectors in inertial coordinates.....	15
Figure 14: Solar radiation spectrum.....	18
Figure 15: Radius of satellite FOV of Earth.....	20
Figure 16: Effect of β -angle on albedo.....	21
Figure 17: Albedo with and without solar-Zenith-angle correction.....	22
Figure 18: Earth IR energy flux at orbital height.....	23
Figure 19: Earth VF for Nadir (left) and off-Nadir pointing (right).....	24
Figure 20: Coordinate system for VF calculation.....	25
Figure 21: Three different cases for calculating VF between plate and Earth.....	25
Figure 22: Angular diameter of celestial body.....	27
Figure 23: Average environment temperature calculation.....	28
Figure 24: Flow diagram of energy transfer in a typical satellite.....	30
Figure 25: Construction of a typical CubeSat solar panel.....	30
Figure 26: Thermal nodes of structure.....	35
Figure 27: Thermal nodes of PCBs.....	36
Figure 28: Example of thermal connections between PCBs and stack rods.....	36
Figure 29: Thermal connections between X+ and X- panels and structure.....	36
Figure 30: Thermal connections between Y side panels and structure.....	37
Figure 31: Thermal connections between X side panels and structure.....	37
Figure 32: Deployable solar panel thermal nodes.....	38
Figure 33: Deployable magnetometer in stowed (left) and deployed state (right).....	39
Figure 34: One dimensional conduction.....	39
Figure 35: Z+ and Z- Structural bracket cross-section.....	40
Figure 36: Y-Side structural rib cross-section.....	40
Figure 37: X- Stack rods cross-section (Dimensions in mm unless otherwise specified).....	40
Figure 38: PCB Spacers.....	41
Figure 39: X+ Stack rods cross-section.....	42
Figure 40: PCB Geometry and internal structure.....	43
Figure 41: Approximation of conduction thermal resistance in PCB.....	43

Figure 42: Accurate model 2-Dimensional flow through laminate PCB.....	44
Figure 43: Side panel thermal resistances	46
Figure 44: Deployable solar panel thermal resistance	47
Figure 45: Deployable panel thermal resistance detail	48
Figure 46: Deployable magnetometer thermal resistances	48
Figure 47: Temperature drop because of contact resistance	49
Figure 48: Exaggerated view of surface roughness	50
Figure 49: Solar panel layer structure	51
Figure 50: 1U Solar panel	52
Figure 51: Nadir (left) and Zenith (right) panels	53
Figure 52: Normal vector of surface relative to vertices.....	55
Figure 53: Screenshot of surface builder visualization	56
Figure 54: Thermal node heat fluxes	56
Figure 55: Generic structure of thermal resistance matrix.....	57
Figure 56: Errors induced by Euler integration for large timesteps.....	59
Figure 57: Errors induced by Euler integration for smaller timesteps	59
Figure 58: Errors induced by 4 th order Runge-Kutta	60
Figure 59: Y-Thomson spin RPY (top) and body rates (bottom)	63
Figure 60: Zoomed Y-Thomson spin RPY (top) and body rates (bottom).....	64
Figure 61: Nadir pointing RPY (top) and body rates (bottom).....	65
Figure 62: Generated solar panel power for Y-Spin (left) and Nadir pointing (right).....	66
Figure 63: Solar panel currents for Y-Spin (left) and Nadir pointing (right).....	66
Figure 64: Current delivered from battery for Y-Spin and Nadir pointing.....	67
Figure 65: Battery voltage.....	68
Figure 66: Battery temperature measurements	68
Figure 67: Simulated Battery temperatures.....	69
Figure 68: Simulated Battery temperatures with limited solar charge heat generation ...	70
Figure 69: OBC MCU temperature for Y-Spin and Nadir pointing	71
Figure 70: Simulated OBC MCU temperature.....	71
Figure 71: Simulated OBC MCU temperature with solar charge	71
Figure 72: Deployed magnetometer temperature.....	72
Figure 73: Simulated deployed magnetometer temperature	73
Figure 74: Temperature ranges of subsystems.....	74
Figure 75: Temperature range of EPS for various β -angles.....	75
Figure 76: Temperature range of deployable magnetometer for various β -angles	76
Figure 77: Temperature range of Y+ deployable solar panels for various β -angles.....	76
Figure 78: Temperature range of Y- deployable solar panels for various β -angles.....	77
Figure 79: Thermal model with thermal contact resistances (left) and without (right) ...	78
Figure 80: Change in MCU temperature for varying PCB spacer material	79
Figure 81: Illustration of MLI (left). Example implementation of MLI (right).....	80
Figure 82: Magnetometer temperature variation with and without MLI blanket	81
Figure 83: Screenshot of surface builder data editor	93
Figure 84: P31U PV converter efficiency	95

Figure 85: P31U Buck converter efficiency.....	95
Figure 86: GomSpace Battery Physical Dimensions	96

List of Tables

Table 1: Reflectance values of various large surfaces on earth	20
Table 2: Angular diameters and surface temperatures of nearby celestial bodies	28
Table 3: Heat transfer from celestial bodies	29
Table 4: nSight-1 main operational modes	32
Table 5: Average duty cycle of sub-systems for typical control modes (values in %)	33
Table 6: Power consumption of fully switched on subsystems	33
Table 7: Power consumption for operational modes (values in mW).....	33
Table 8: Regulator losses for operational modes (values in mW)	34
Table 9: Battery current for operational modes (values in mA)	34
Table 10: Z+ and Z- Structural bracket thermal resistance calculation	40
Table 11: Y-Side structural rib thermal resistance calculation	40
Table 12: X- Stack rods thermal resistance calculation	41
Table 13: X- Stack spacers thermal resistance calculation	41
Table 14: Total X- parallel stack resistance calculation	42
Table 15: X+ Stack rods thermal resistance calculation	42
Table 16: X+ Stack spacers thermal resistance calculation	42
Table 17: Total X- parallel stack resistance calculation	42
Table 18: PCB layer thermal resistance	44
Table 19: FIPEX mounting plate thermal resistances	45
Table 20: VFs of PCBs to each other	46
Table 21: Thermal resistances for conduction within side panels	47
Table 22: Thermal resistances of solar panel backings.....	48
Table 23: Emissivity and solar absorptivity of the solar cell	52
Table 24: Emissivity and solar absorptivity of bare Polyamide PCB	52
Table 25: Annotations of surfaces.....	53
Table 26: Average emissivity and solar absorption of body panels.....	54
Table 27: Attributes of a surface segment.....	54
Table 28: Comparison of simulation with and without heat generated due to charging...	70
Table 29: Operational temperature ranges for each subsystem	73
Table 30: Total resistance between PCB and structure for varying space material	79
Table 31: Full list of thermal nodes	87
Table 32: Full list of thermal resistances in model	89
Table 33: P31U Electrical Characteristics	94
Table 34: P31U Physical Characteristics	95
Table 35: GomSpace Battery Specifications.....	96
Table 36: P110 series physical specifications	97
Table 37: P31U Electrical Characteristics	98
Table 38: QIOptic Cover glass transmission specifications	99

List of Abbreviations and Acronyms

ADCS	Attitude Determination and Control System
AIT	Assembly, Integration and Test
CoM	Centre of Mass
COTS	Commercial Off-The-Shelf
CSKB	CubeSat Kit Bus
DCM	Direct Cosine Matrix
ECI	Earth-Centred Inertial
FEA	Finite Element Analysis
FOV	Field of View
FR4	Flame Retardant
IR	Infrared
LEO	Low Earth Orbit
ORC	Orbit Referenced Coordinate
PCB	Printed Circuit Board
PV	Photovoltaic
RAAN	Right Ascension of the Ascending Node
SBC	Spacecraft Body Coordinate
SGP4	Simplified General Perturbation model
SSO	Sun-Synchronous Orbit
TLE	Two-line Element
UHF	Ultra-High Frequency
VF	View Factor
VHF	Very-High Frequency

Nomenclature

α_s	Solar absorptivity
β	Angle between sun and orbital plane
e	Eccentricity
ε	Emissivity
h	Satellite altitude
i	Inclination
k	Thermal conductivity constant
v	True anomaly
ω	Argument of perigee
Ω	Right ascension of ascending node
\dot{Q}	Heat transfer rate
q	Heat flux
R_E	Radius of earth
R_c	Conductive thermal resistance
ρ	Angular radius of Earth-disc as seen by satellite
σ	Stefan-Boltzmann constant
U	Internal energy
ξ	Solar zenith angle

1 Introduction

Satellites have greatly reduced in size over the years and the introduction of CubeSats marshalled in a new era of satellite development. CubeSats are small, relatively simple to build, much more affordable, and yet have proved very powerful for applications related to Earth Observation (EO) and Internet of Things (IoT) when launched in clusters or constellations. Furthermore, CubeSats provide a great platform for teaching inexperienced teams how to build satellites because of the low cost and complexity. First introduced in the year 2000, this nano-satellite concept formed part of a university project led by Stanford University in California, USA [1]. Thereafter, in 2003, the CubeSat design specification was formalised in a document for the first time but has since been updated to remain current in a rapidly evolving landscape [2].

Unfortunately, despite their low technical complexity, a high percentage of CubeSats that are built fail, with only about 20% achieving full mission success [3]. This is because the depth to which designs are tested and analysed is typically limited due to small budgets, short timelines and inexperienced teams. The overarching reasons for the high number of failures, and some guidelines on how to increase chances of success when doing a CubeSat project, especially within an university environment, are discussed at length in [4] and [5]. This study will instead focus specifically on one cause for failures on CubeSats and that is bad thermal design.

The following are some of the most important reasons for the lack of thorough thermal analyses in CubeSat missions;

- CubeSat teams typically consists of undergraduates or hobbyists that usually have good knowledge of electronics and software but frequently lack the expertise to do thorough thermal modelling and simulation of their satellites' temperatures,
- Commercial thermal simulation packages that are suitable for space is expensive, and
- The thermal environment in space is particularly complex because of the significance of radiative heat transfer.

The complexity of using traditional thermal analysis software to simulate CubeSats has been discussed in multiple previous studies, and many attempts have been made to address this problem by creating simplified thermal models [6], [7], [8], [9]. Simplified thermal analysis tools have been developed successfully, and it has been demonstrated that good results can be achieved using these tools to simulate a satellite in a particular orbit and in a particular orientation. One major limitation of these studies is that only simplified, fixed position analyses can be done where only a single, specific orbit and satellite orientation is considered. For analysis of the temperatures a CubeSat should experience throughout its lifetime, the following varying factors need to be considered:

- changing attitude of the satellite,

- changing orbit (especially for LEO orbits), and
- changing electrical load with different control modes.

It is argued that the thermal analysis of a satellite should therefore be done in close connection with the attitude simulation thereof. The decay of a LEO has a significant effect on the amount of sunlight reaching the satellite. If the satellite is not in a Sun-synchronous orbit the angle between the Sun-vector and the orbital vector changes and the eclipse time of the orbit varies between a maximum eclipse (which depends on altitude), and a minimum eclipse which can be zero if the Sun-vector and the orbit vector is aligned. This change in angle not only affects eclipse times, but also affects which parts/panels of the satellite is illuminated by the Sun during nominal flight orientation. The varying emissivity/absorptivity of the different panels of the satellite, together with this variance in panel illumination, leads to a significantly varying total solar heat flux absorbed by the satellite. There is thus a need for an affordable satellite thermal simulation tool that is simple to use and optimised for simulating dynamic in-orbit scenarios. This would allow teams building CubeSats to more thoroughly test their thermal designs and hopefully contribute significantly to the success rate of CubeSats.

The high-level mission of this study is to develop a thermal analysis tool capable of simulating the temperature for a CubeSat for various in-orbit scenarios, using a South African built CubeSat called nSight-1 (callsign AZ02) as a test case (shown in Figure 1).



Figure 1: nSight-1 Flight model pre-launch

The high-level mission is translated into goals:

- Create a simplified thermal model that can be used in simulation to predict the temperatures of a CubeSat and its subsystems to high enough accuracy that it can be used to design the thermal subsystem for a CubeSat before launch,

- Create the thermal simulation environment to simulate the model of the satellite with heat sources and sinks representative of the space environment,
- Create a generic intuitive tool for inputting the thermal and surface model of a satellite into the thermal simulation,
- Combine the thermal simulation of the satellite with an attitude simulation package to simulate the satellite for dynamic in-orbit scenarios,
- Verify the simulation performance with in-orbit measurements of a real satellite, and
- Make useful conclusions about the satellite that was simulated, and recommendations for how this satellite's thermal design could be improved.

How these goals were achieved during this study is systematically described in this thesis document.

- **Section 2: Literature review**, provides a summary of a few pieces of relevant literature which more clearly states the need for this research, as well as literature that describes related work available in the public domain.
- **Section 3: Theoretical Background and Definitions**, provides a comprehensive theoretical background of relevant scientific and mathematical principles that were required to complete this study, and can be used as reference material when reading this thesis.
- **Section 4: Heat Sources and Sinks**, describes the thermal environment in space which serves as external sources/sinks of heat to the satellite, as well as internal heat generation in the satellite.
- **Section 5: Satellite Thermal Model**, describes a simplified distributed lumped mass thermal model of the satellite and provides detailed information on the thermal surface properties of the outside surfaces of the satellite. It also provides a brief description of the tool that was created to input surface models of a satellite into the simulation.
- **Section 6: Simulation Design**, gives a brief overview of the logical structure of the simulation environment, and provides some additional theory relating to the numerical simulator/solver.
- **Section 7: Simulation Results and In-Orbit Measurements**, shows simulation results for a few nominal orientation cases for a simplified plate and compares these results with analytical predictions, with the aim of verifying some of the core functionality of the simulation environment. It then compares in-orbit data with the simulation results of the complete satellite in orbit.
- **Section 8: Discussion, Conclusions and Recommendations**, finally reflects on the results obtained in the study, discusses the significance of a few interesting cases, provides some recommendations for how the work done in this study could have retrospectively been done better, and can be built upon in future studies.

2 Literature Review

CubeSats were originally intended for education use, with the focus on giving young, inexperienced engineers the opportunity to be involved in the design, build, launch and commissioning of satellites. One of the first major educational projects to utilise CubeSats for this objective was the OPAL program [1] at Stanford University. At the time, a specific focus was placed on developing systems engineering skills. The schedule for the entire design and build of the satellite was set to one year, with a budget of \$50000 (USD) which limited the team to using Commercially-Off-The-Shelf (COTS) components, and a required satellite in-orbit lifetime of one year. This program's limited budget, short schedule, and inexperienced team is a good example of the norm for typical CubeSat missions and demonstrates the limited resources that are available for complex analyses and expensive software simulations in such missions.

Practical thermal testing is one way of, at the very least, making sure that a satellite can survive at certain extreme temperatures, given an extreme and rapidly varying thermal environment. However, given limited access to, and the high cost to use these powerful thermal vacuum chambers most CubeSat teams must settle for limited testing. In certain cases CubeSat teams have the privilege of piggybacking off of existing larger satellite infrastructure [10], but this is country and institution specific. Typically, CubeSat teams have limited access to both simulation software as well as testing facilities, especially in countries that do not have established national satellite programs and/or relevant Assembly, Integration and Test (AIT) facilities.

An interesting case where the precession of a satellite's orbits significantly changed the dynamic and equilibrium temperatures of the satellite is the C3P satellite [11]. After more than a year in orbit, the satellite experienced overheating of electronics, and rapidly changing temperatures in multiple components. The satellite operators originally suspected an electronic malfunction which resulted in large currents in the satellite, and consequently higher internal heat generation and higher temperatures on components. This hypothesis was supported by the fact that the satellite's batteries cycled more rapidly than in past cases and discharged deeper. After investigation it was confirmed that the change in temperature cycling behaviour, as well as change in power generation, was caused by a precessing orbit. This change in orbit resulted in a changing eclipse length, which saw different panels on the satellite being illuminated that had different thermal properties, and a changing albedo intensity.

For CubeSats, the thermal analyses done on a system level is usually aimed at investigating satellite temperatures in a broader sense, not necessarily focusing on the electronics component level. These types of analyses are done to investigate operational cases where the satellite would reach extreme temperatures, and then based on these findings, appropriate side panel coatings would be selected to passively control the satellites temperature to allowable ranges. This type of analysis assumes that subsystems were designed with appropriate heat dissipation mechanisms in mind, and focus is not

necessarily placed on the local temperature extremes seen by the various electronic components. Analyses that focus specifically on these component level temperatures are typically done using Finite Element Analysis (FEA) type software packages. These simulations are less focussed on orbital and attitude information since the electronics inside the satellite are not directly exposed to external heat sources (such as the Sun). Instead a specific attitude and orbital scenario is assumed, resulting in some net external heat flux, and some equilibrium temperature on each of the subsystems.

From a mission design perspective, these detailed analyses are not necessary since COTS CubeSat parts are mature enough that good thermal design can be assumed. Therefore, engineers analysing the temperature of a CubeSat rather need a tool that is focussed on external heat sources/synchs for varying attitude and orbit to be able to analyse the temperature of the satellite on system level. It would thus be beneficial if the two approaches can be combined to the extent that, at a minimum, the major temperature sensitive components such as the batteries for example can be included in the simulation.

Most of the thermal analyses done for CubeSats usually make use of significantly simplified models for albedo and for Earth IR. Examples include [12], [13] and [14]. Typically, a constant albedo factor of roughly 0.3 is assumed, and orbital inclination and position are ignored. For larger, more expensive satellite missions, more detailed models are used, and it has been demonstrated that simplified models result in significantly reduced accuracy. A good example of such a study, which made use of both a simplified and commercial software approach, was [15]. In this study both a Matlab model, as well as the commercial NX6.0 TMG software were used and compared with one other.

Furthermore, a study by Baturkin [16] focussed on providing a summarised overview of thermal control concepts, but with a stronger focus on Microsatellites. This study also provides a very complete list of available commercial thermal simulations tools, which might be useful for readers who are investigating such available tools. However, microsatellites are typically launched in higher altitude orbits where Earth IR and albedo have a significantly lower affect than what is seen in the case of CubeSats which needs to be kept in mind.

The Earth Radiation Budget Experiment (ERBE) satellite, which was launched in 1984, had the mission of better studying the near-Earth thermal environment. The satellite collected 28-month long datasets of thermal measurements at an interval of 16 s. Additionally, NASA has a wide selection of documents in the public domain relating to the space thermal environment of satellites. One such document [17], describes a new method IR and albedo predictions proposed by NASA for use in the thermal design of among others the International Space Station (ISS), as well as NASA space shuttles. The 2001 study relies on the dataset generated by the ERBE and considers the widely used orbital average constant albedo factor and compares it with the measurements from the ERBE. By doing so, this study introduces a polynomial correction factor which shows improved correlation with the measured data. However, it does not discuss the complex problem of determining the view factor (VF) of panels on a satellite to Earth.

VFs of satellite surfaces to the Earth sphere, has a significant effect on the albedo and IR absorbed by the satellite. These VF calculations are complex and require integration over complex geometrical shapes to be able to find analytical solutions. A few widely referenced papers were written in the 1960s on analytical solutions to the albedo and IR received by panels of a satellite. Then in 1992, a paper was written which built on these previous studies by providing more practical analytical solutions to the albedo for surfaces with arbitrary orientations, in arbitrary orbits [18]. This paper provides a VF of the satellite to the entire part of the Earth sphere that is visible to the satellite for use in calculating IR and provides a more complex VF which takes into account the solar terminator line for albedo calculations.

Analytical solutions like these can be used to do more accurate steady state analyses, but they still have limited use for LEO orbits that are not sun synchronous, where orbital precession and decay result in rapidly changing orbits. The analytical solutions typically have discrete cases for when solar Zenith angles are large and small, whether the eclipse terminator is beneath the satellite or not, and other complex geometrical variations. For such a LEO mission there is no single solution that covers all the thermal environments the satellite will experience during its mission lifetime.

The early CubeSat missions all used body fixed solar panels, which made them a lot simpler to model. The extra power that deployable solar panels provide was not required since CubeSats had relatively simple functions and required little power. However, in recent years, CubeSats have evolved significantly and tend to be larger, execute more complex and power-hungry tasks and therefore, typically have deployable solar panels. These deployable panels make thermal analyses significantly more complex to execute, since the panels shadow the rest of the satellite. The amount of energy reaching the top side of the deployables, and the amount reaching the rest of the satellite body, is dependent on the position and orientation of the satellite and its deployables relative to the Sun and Earth. This is further motivation for doing simulations of the satellite in a dynamic environment.

The thermal surface model of solar panels is also more complex than other surfaces, since all 'absorbed' solar radiation is not turned into heat but rather some of it is turned into electrical energy. A more accurate model for solar panel thermal surfaces is discussed in [19]. The author of this paper suggests using a modified absorptance for the solar panel surface, which considers the fact that only a percentage of the incoming absorbed radiation is turned into heat. From a thermal point of view the portion of the energy that is transformed to electrical energy does not affect the surface of the panel. The electrical energy generated by the panel will eventually also be turned into heat, but this will happen on a subsystem level, where the electrical energy is 'consumed' by electronics.

3 Theoretical Background and Definitions

To be able to build a thermal model and a thermal simulation environment for a satellite, certain definitions and pieces of theoretical background is required. In this section, the following topics are discussed;

- Definitions required to be able to describe the
 - coordinate system used to describe the orientation of a body in inertial space,
 - coordinate system used to describe orientation of a body in referenced to its orbit around the Earth,
 - coordinate system used to describe the direction to a target relative to the body of a satellite,
 - geometric relationships between the satellite, Earth and other celestial bodies,
- and methods/theory required to
 - rotate between these coordinate systems, and
 - calculate conductive and radiative heat transfer rates.

Further theory is discussed in the rest of the document as it is required but typically builds on the information provided in this section.

3.1 Orbital and Attitude Dynamics

In this section the focus is on the mathematical description of the orbit, the position and orientation of the satellite in the orbit, as well as the relevant coordinate systems and definitions that are used to describe these positions/orientations.

A variety of geometrical variables relating to the satellite orbit and celestial bodies are defined, and the relationship between these variables is investigated. These variables and definitions are used in the rest of the document, especially in Section 4, and this section serves as a geometrical and mathematical reference when reading the rest of the document.

3.1.1 Coordinate Definitions

To be able to mathematically describe the position of the satellite in the orbit, as well as the orientation of the satellite relative to the orbit, the following coordinate systems are defined.

3.1.1.1 Inertial Coordinate System

As is common practice with satellite theory, an Earth-Centred Inertial (ECI) coordinate system is used as inertial reference. ECI frames use the Earth's equatorial plane, as well as the Earth's orbital plane, to define an inertial coordinate system. One such ECI coordinate definition is the J2000 system.

The J2000 system uses the vernal equinox together with the rotation axis of the earth as inertial vectors to define an inertial coordinate system. The Earth's rotation axis has periodic oscillations and is not perfectly fixed, so such definition for use in the ECI requires some assumptions. The J2000 system uses the average Earth rotational axis as of 12:00 Terrestrial Time on 1 January 2000. With this definition of the Earth rotational axis, the corresponding vernal equinox is defined.

The Earth's equatorial plane is rotated with an angle of roughly 23.4 degrees relative to the earth's orbital plane around the Sun. The vernal equinox is defined as when the Earth is in such a position that a vector from Earth to the Sun (therefor a vector within the orbital plane) intersects the Earth's equatorial plane. The vernal equinox is illustrated in Figure 2.

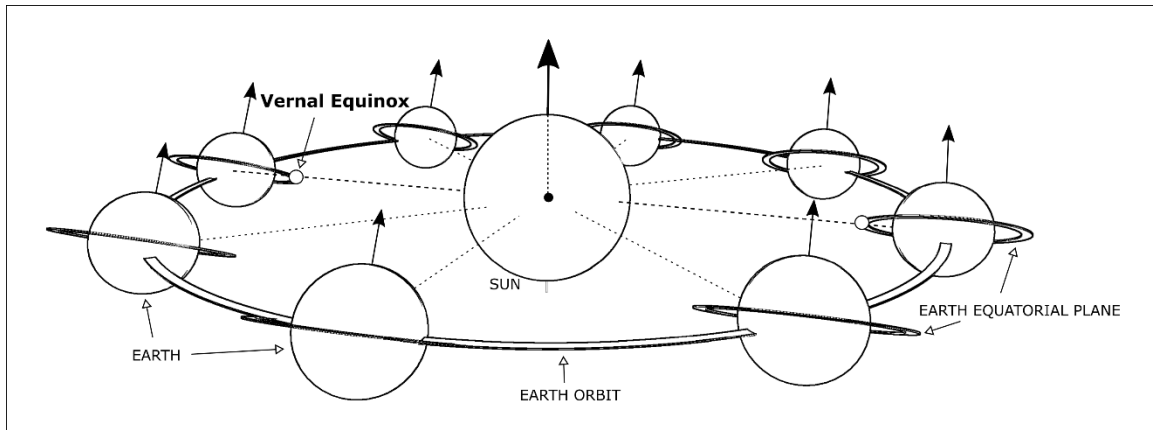


Figure 2: Definition of the Vernal Equinox

The J2000 ECI is then defined with X_{ECI} , Y_{ECI} , and Z_{ECI} as shown in Figure 3.

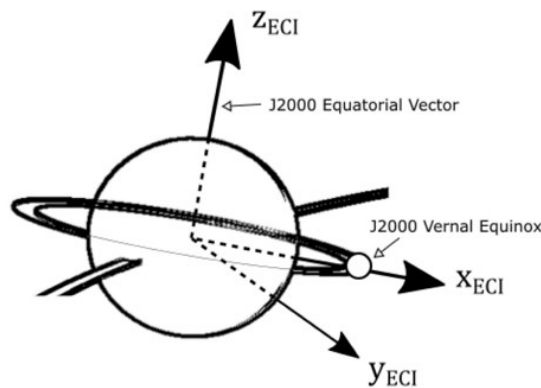


Figure 3: J2000 ECI Frame

3.1.1.2 Orbit Reference Coordinate System

An orbit referenced coordinate (ORC) system is defined that stays fixed relative to the orbit but rotates relative to the ECI. The ORC is defined with X_{ORC} in the orbital velocity direction, Z_{ORC} is defined in the Nadir direction, and Y_{ORC} completes the orthogonal set as illustrated in Figure 4. This is the standard definition used in common ADCS literature as in [20].

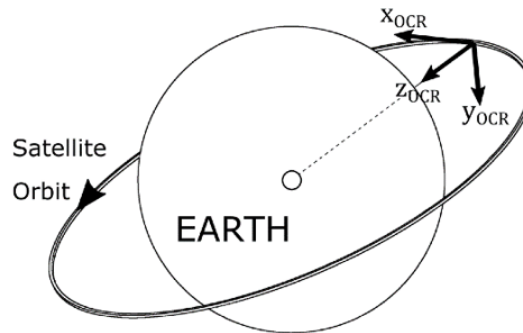


Figure 4: ORC Frame Definition

3.1.1.3 Satellite Body Coordinate System

A satellite body coordinate (SBC) system is defined that stays fixed relative to the satellite body. For convenience, the SBC is defined so that the SBC aligns with the ORC when the satellite is in its nominal orientation. For n-Sight-1 the SBC is defined with X_{SBC} pointing out orthogonal to the velocity face of the satellite (face which houses the QB50 science payload), Z_{SBC} pointing out orthogonal to the Nadir face of the satellite (face housing the imager payload), and Y_{SBC} completing the orthogonal set. The SBC for the n-Sight mission is shown in Figure 5 below.

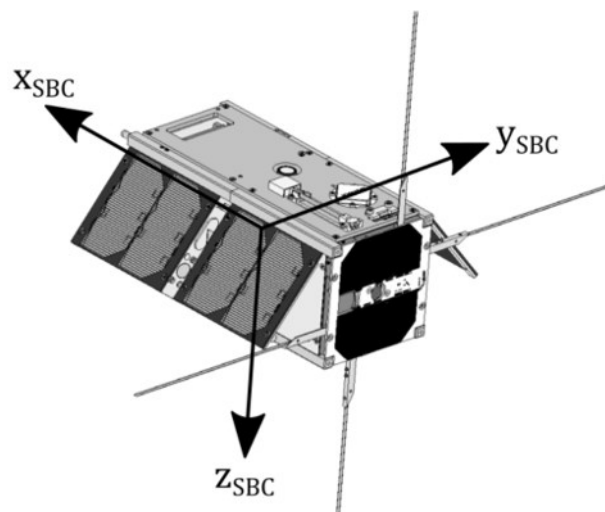


Figure 5: SBC Definition for nSight-1

3.1.2 Attitude Format and Operation Mode Definitions

This section defines the format in which the satellite's position and orientation information is given, as well as common ADCS operation modes that are referred to later in the document.

3.1.2.1 RPY Definition

The orientation of the satellite can be defined by three intrinsic body rotations namely Roll, Pitch and Yaw. These rotations correspond to Euler rotations, which has limitations due to singularities. Within the ADCS dynamics propagator, quaternions are used to avoid these singularities. For the purposes of describing the orientation of the satellite in this study, only these angles are required. If only single rotations are used the RPY can be illustrated as in Figure 6. Note that once multiple rotations are done for more complex orientations, the Euler angle definitions are slightly more complex, since the principle axes rotate. However, this is never required in this thesis.

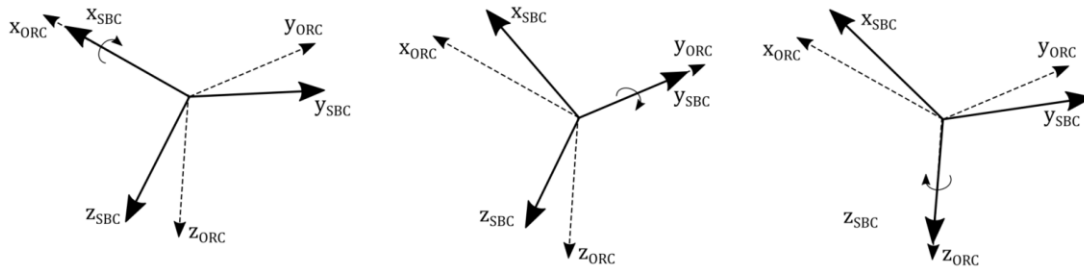


Figure 6: RPY Definition

3.1.2.2 Common ADCS Control Modes

Y-Thomson spin

After release into orbit from a deployer pod, a satellite usually has some random tip-off rate. The first step of the process to control the orientation of the satellite is to reduce (“dump”) the tip-off rates and control the satellite's orientation to have either zero RPY body rotation rates, or to be in a safe-mode spin. This safe-mode spin is typically one that is stable, which implies that it is around the principle axis with largest inertia (see intermediate axis theorem). This spin is usually also chosen in a way which guarantees at least some exposure of the solar panels to the Sun.

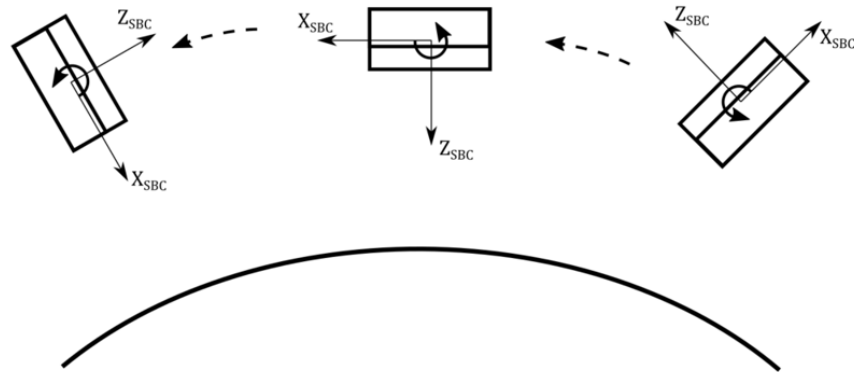


Figure 7: Y-Thomson Spin

One such safe-mode spin, and the chosen mode for nSight-1, is a Y-Thomson spin. In a Y-Spin the satellite Y_{SBC} axis is aligned with the orbit Y_{ORC} axis, and the satellite spins around this axis as illustrated in Figure 7. The reason why this control mode is beneficial from a control systems point of view is:

- 1) The spin momentum vector stays inertially fixed throughout the orbit,
- 2) The spin provides gyroscopic stiffness to the satellite making it less sensitive to disturbance forces, and
- 3) This mode transitions well into a Y-Momentum biased Nadir pointing mode, as discussed in the next section.

From a momentum and power generation point of view, it guarantees solar radiation on at least one of the solar panels throughout the spin regardless of the angle between the orbital plane and the Sun, as discussed in Section 3.1.3.3

Momentum biased Nadir pointing

After reaching a stable Y-Spin, a typical low-power Nadir pointing (Zero Roll, Pitch and Yaw angles) control strategy is to absorb the rotation of the satellite into a single reaction wheel placed in the Y_{SBC} , and then to control the orientation of the satellite to stay Nadir pointing using magnetic control. The satellite assembly maintains the same momentum vector it had while in Y-Spin, but this momentum is transferred to a reaction wheel, instead of a rotating satellite body.

3.1.3 Satellite Orbital and Celestial Geometry

3.1.3.1 Kepler Elements

The Simplified General Perturbations 4 (SGP4) model is used in the EOS simulation software to propagate the position of the satellite in-orbit. This model is used to calculate the orbit of Near-Earth objects using Two-Line Element (TLE) sets. These TLEs are provided by the North American Aerospace Defence Command (NORAD) and NASA.

They scan near-Earth orbit and provide new TLEs for objects in-orbit regularly. The TLEs consist of two lines, each with 69 American Standard Code for Information Interchange (ASCII) characters and with the format as specified in [21].

The TLEs contain information on the name and description of the satellite, and information on its orbit. The orbital information is specified as Keplerian orbit parameters as well as perturbation and drag terms. These describe periodic changes in the orbit as well as continuous degradation of the orbit due to drag.

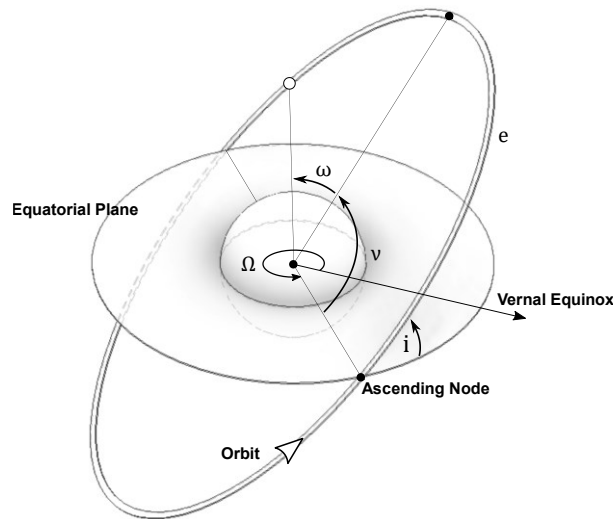


Figure 8: Keplerian orbit parameters

The Keplerian orbit is defined as in Figure 8 with the orbital elements defined as [20]:

- ω - Argument of perigee
- Ω - Right ascension of ascending node
- v - True anomaly
- i - Inclination
- e - Eccentricity

These TLEs are formed by combining long term measurements to create an averaged model of the position and velocity of the satellite. The SGP4 propagator uses the TLEs to predict a positional vector to the orbiting object, as well as the velocity of the object. Free implementations of SGP4 propagators are available for most common programming languages. One such source of these implementations can be found on the Celestrak site [22]. This model is not perfectly accurate, since some disturbances on the satellite are not deterministic. These include variable drag due to satellite attitude, atmospheric density variations due to solar activity, and others. The accuracy to which the position of a satellite can be predicted using the SGP4 propagator can be kept to under 1 km for LEO satellites if updated daily [23].

3.1.3.2 Local Horizon

Another important geometrical variable which is required for further calculations is the angle measured from the Nadir vector, to the vector to the local horizon as seen by the satellite, both in the SBC. This angle is shown in Figure 9.

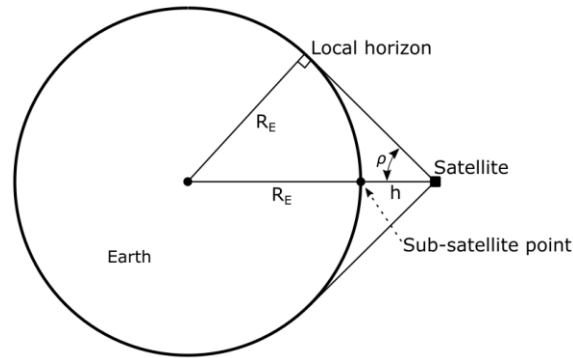


Figure 9: Angle to local horizon in SBC

Where

- R_E – Earth’s radius
- h – Satellite altitude
- ρ – Angular radius of the Earth-disc as seen by satellite

By simple trigonometry we can calculate

$$\rho = \text{asin}\left(\frac{R_E}{R_E + h}\right) \quad (1)$$

3.1.3.3 Sun β -Angle

The angle between the orbital plain and the vector from the Earth to the Sun is an important factor which determines eclipse lengths and influences the satellite thermal environment significantly. The sun β -angle is illustrated in Figure 10.

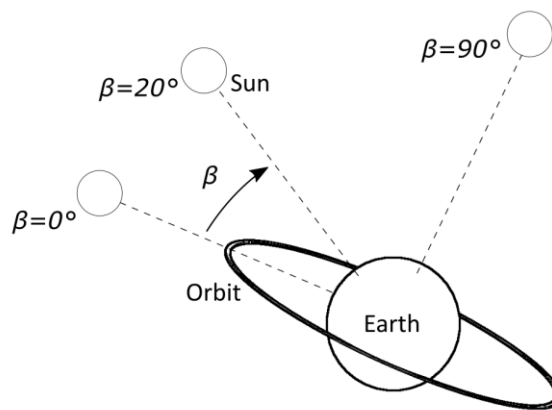


Figure 10: Sun β -Angle geometry

For purposes of calculating the temperature of the satellite, it is important to calculate what the duration of eclipse is, the period where the satellite is shielded from sunlight by the Earth. The procedure on P98-P110 of SMAD [20] can be followed to plot the motion of the Sun on a spacecraft centred sphere as in Figure 11.

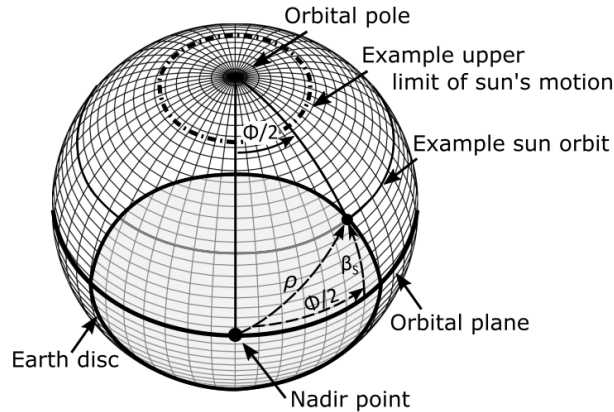


Figure 11: Sun path on spacecraft centered sphere

Figure 11 shows the unit spherical view centred on the spacecraft. The Earth disc is the part of the spacecraft's view that is obstructed by the Earth, with angular radius as calculated in Figure 9. The orbital plane divides the satellite's spherical view into two halves. Assuming a Nadir pointing satellite, the Sun rotates through the view of the satellite in a circle which is offset with angle β_S from the orbital plane for a particular orbit. The locations where this circle and the Earth disc intersect are where the satellite enters and leaves eclipse. For a given β_S , the angle ϕ provides the angular diameter of the ecliptic section of the orbit, measured parallel to the orbital plane. Using the spherical trigonometrical rules described in Table D1 of [1], ϕ can be calculated as

$$\phi = 2 \cdot \arccos\left(\frac{\cos(\rho)}{\cos(\beta_S)}\right) \quad (2)$$

This equation is only valid if $\beta_S < \rho$, since there will be no eclipse otherwise. The fraction of the orbit spent in eclipse can be calculated as

$$F_{eclipse} = \phi/360 \quad (3)$$

The solar Zenith angle ξ can be defined between the Earth-Sun vector, and the Earth-satellite vector. As the satellite rotates in its orbit, an angle θ can be defined for the rotation of the satellite in the orbital plane, away from the line formed by projecting the Earth-Sun vector onto the orbital plane. This is defined in Figure 12.

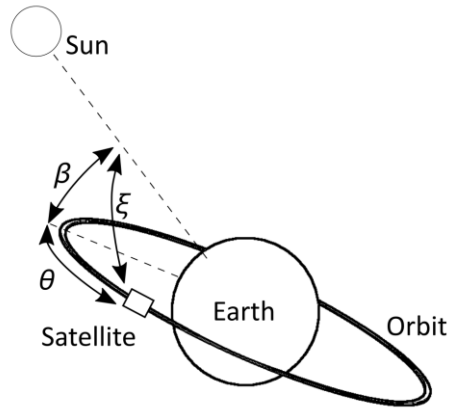


Figure 12: Solar Zenith-angle definition

Using the rule of cosines as defined in table D-1 on P905 of [20], we see that

$$\cos \xi = \cos \beta \cos \theta \quad (4)$$

Analytically the β and θ -angle can be calculated from the satellite TLEs and Unix time together with an appropriate Sun model. In simulation environment the satellite motion and environment are numerically propagated and the Earth-Sun vector, as well as the Earth-satellite vector can be obtained from the satellite environment and kinematic models.

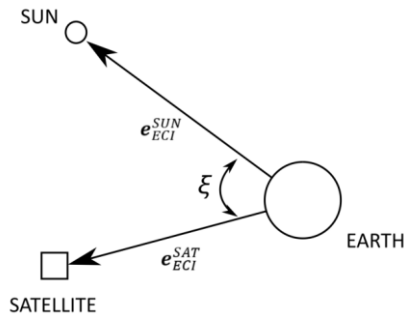


Figure 13: Solar Zenith angle from Sun and satellite vectors in inertial coordinates

Figure 13 shows the solar Zenith angle in relation with the Earth-Sun (e_{ECI}^{SUN}) and Earth-satellite (e_{ECI}^{SAT}) unit vectors in the inertially referenced ECI frame. Using the standard dot-product definition

$$\cos \xi = e_{ECI}^{SUN} \cdot e_{ECI}^{SAT} \quad (5)$$

the solar Zenith angles can be calculated using these two vectors.

3.1.4 Celestial Equations

EOS uses models described in [24] to calculate the vectors to the Sun and the Moon. The algorithm described on P151-153 is used to calculate the position of the Sun. This algorithm is an adaptation of previously less accurate algorithms, to include perturbations due to the effects of the eccentricity of the Earth's orbit, and gravitational disturbances to the Earth's orbit by the Moon, Venus, Mars and Jupiter. Similarly, the algorithm described on P307-308 is followed to calculate the position of the Moon. These algorithms provide a vector to the Sun (\mathbf{s}), and to the Moon (\mathbf{m}), in the J2000 ECI frame.

3.2 Heat Transfer

3.2.1 Radiation

The radiosity of a body is the amount of electromagnetic radiation leaving its surface. A blackbody is defined as a body with surfaces that perfectly absorb all incoming energy, and perfectly radiates energy. Such a body radiates energy in proportion to its temperature in accordance with Stefan-Boltzmann law

$$J = \sigma T^4 \quad (6)$$

where σ is the Stefan-Boltzmann constant, and T is the absolute temperature of the body in Kelvin. The frequency spectrum of the radiation from such a blackbody, is given by Planck's law which defines the spectral radiance for a body at a specific frequency and temperature.

If two theoretical blackbodies are placed in a configuration where all energy radiated by the one body is incident on the surface of the second body and vice-versa, the net heat transfer from body one to body two is the difference in the radiated energies between the bodies so that

$$\dot{Q}_{12} = A_1(\sigma T_1^4 - \sigma T_2^4) \quad (7)$$

For practical geometrical situations, for bodies with finite size, only a part of the energy leaving the surface of one body reaches the second body. The fraction of the energy leaving body one, that reaches body two is defined as the VF F_{12} which is dependent on the geometry of the two bodies, and their geometrical/spatial relation. Shape factors are typically complex to calculate, but a lot of literature is available in the public domain for most common practical situations. Taking the VF into account, the net heat transfer from a finite body one, to a finite body two, with VF F_{12} , the heat transfer is

$$\dot{Q}_{12} = A_1 F_{12}(\sigma T_1^4 - \sigma T_2^4) \quad (8)$$

Practical surfaces do not behave exactly like blackbodies. Instead, such practical surfaces only absorb a fraction of incoming energy and radiate less energy than blackbodies. The

most widely used model for practical surfaces is that of a graybody. For a graybody, a constant absorptance α is assumed for all frequencies of incident radiation. Similarly, a constant emissivity ε is assumed which defines the fraction of the energy radiated relative to a blackbody. Further, for a graybody the absorptivity and emissivity are assumed to be equal.

For one finite graybody, to a second finite graybody, with a VF F_{12} , the net heat transfer is

$$\dot{Q}_{12} = \frac{\sigma T_1^4 - \sigma T_2^4}{\frac{1 - \varepsilon_1}{\varepsilon_1 A_1} + \frac{1}{A_1 F_{12}} + \frac{1 - \varepsilon_2}{\varepsilon_2 A_2}} \quad (9)$$

This is the model that is assumed for heat transfer between different parts of the satellite, as well as between the satellite and the Earth.

Outside surfaces of the satellite that face deep space, has VF 1. Deep space is assumed to behave like a blackbody ($\varepsilon = 1$). For heat transfer between the surfaces of the satellite and deep space, Eq 9 can be simplified to the equation below. $T_{deepspace}$ is defined in Section 4.5.

$$\dot{Q}_{12} = \frac{\sigma T_1^4 - \sigma T_2^4}{\frac{1 - \varepsilon_1}{\varepsilon_1 A_1} + \frac{1}{A_1}} = \sigma \varepsilon_1 A_1 (T_1^4 - T_{deepspace}^4) \quad (10)$$

3.2.2 Conduction

Conductive heat transfer through a solid can be calculated using Eq 11 which is derived from Fourier's law of conductance together with the assumption of a homogeneous substance.

$$\dot{Q} = -kA \frac{dT}{dx} \quad (11)$$

where k is the conductance of the material, A is the cross-sectional area of the material, and x is in the direction of the heat-flow. For conduction from one location in a material to another over a length L , the heat transfer rate is

$$\dot{Q}_{12} = \frac{T_1 - T_2}{L/kA} = \frac{T_1 - T_2}{R_c} \quad (12)$$

Where R_c is the conductive thermal resistance of the connection between point 1 and 2 defined as in Eq 13.

$$R_c = \frac{L}{kA} \quad (13)$$

4 Heat Sources and Sinks

To determine the temperature of a satellite as it orbits around Earth in the space environment, it is necessary to consider the energy balance of the satellite. According to the principle of conservation of energy the change in internal energy of a solid, incompressible control volume for a given timestep is

$$\frac{\Delta U}{\Delta t} = \dot{Q} + \dot{Q}_v \quad (14)$$

where

U is the internal energy of a system,

\dot{Q} is the heat transfer rate to the control volume, and

\dot{Q}_v is the heat generation rate within the system.

In this chapter the various sources and sinks of energy to and from the satellite are considered. The main direct source of energy for a satellite is the Sun. Radiated solar energy reaches the surfaces of the satellite both directly and indirectly through reflection off of other celestial bodies (such as the Moon and Earth). Further external sources of energy include IR radiation from the Earth, and energy from deep space.

4.1 Direct Sunlight

The typical spectrum of solar radiation is shown in Figure 14 as measured by the American Society for Testing and Materials (ASTM) Terrestrial Reference Spectra and is used as the standard definition for sunlight in the photovoltaic (PV) industry [25].

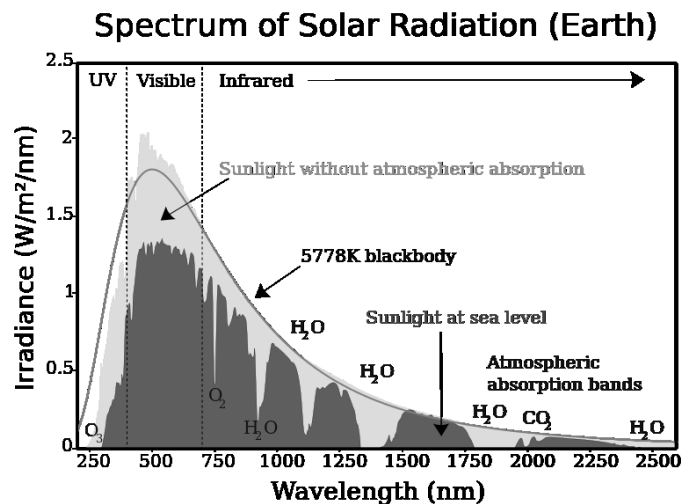


Figure 14: Solar radiation spectrum

Because of the large distance between the Sun and the Earth, the energy that reaches the satellite can be assumed to be parallel rays of radiation with uniform distribution. The

intensity of this radiation varies significantly with seasonal changes, as the Earth moves further and closer to the Sun in its elliptical orbit. The radiant flux of the sunlight near Earth can be calculated as [20]

$$I_s = \bar{I}_s(1 + e_s \cos(\nu_s))^2 \quad (15)$$

where

e_s is the eccentricity of the Earth's orbit,

ν_s is the true anomaly of the Sun, and

\bar{I}_s is the mean solar constant, 1353 W/m^2 .

The amount of solar energy absorbed by a surface on the satellite is then determined by the projected area of the surface to the Sun, as well as the solar absorptivity (α_s) of the surface. For a particular surface i with surface area A_i , emissivity ε_i , and unit normal vector \mathbf{n}_{SBC}^i in the SBC frame, the total solar flux is then

$$Q_{solar} = I_s A_i \alpha_{si} (\mathbf{n}_{SBC}^i \cdot \mathbf{e}_{SBC}^{Sun}) \quad (16)$$

where \mathbf{e}_{SBC}^{Sun} is the unit vector from the spacecraft to the sun in the SBC frame.

Note that in Section 3.2.1 the assumption is made that for a graybody absorptance equals emissivity. When considering the absorptance of sunlight on a surface, we use a more accurate absorptance figure that takes into consideration the solar spectrum, and the way a surface absorbs solar radiation. For such a surface $\alpha_s \neq \varepsilon$. The ratio of solar absorptance to emissivity of a body and its surfaces that is not generating its own heat, would therefore determine the steady-state temperature it will reach.

4.2 Earth Albedo

Of the sunlight that hits the Earth's atmosphere, a portion is absorbed by the Earth and its surrounding atmosphere and a portion is reflected back into space. Sunlight is absorbed by, penetrates through, and is reflected off of the atmosphere and the surface of the Earth in a complex manner which is determined by factors such as the make-up and density of the atmosphere, cloud coverage and the reflectance of the surface of the Earth that the rays hit.

The predominant factor determining the amount of energy reflected back into space is the reflectance of the part of the Earth's surface that is illuminated. This reflectance varies dramatically for different surface types. Some reflectance values of typical surfaces are shown in Table 1.

Table 1: Reflectance values of various large surfaces on earth

Surface type	Reflectance
Freshly fallen snow	0.9
Melting Snow	0.4
Dirty Snow	0.2
Trees	0.09 - 0.18 (Depending on moisture and snow coverage)
Clouds	0-0.8
Water	Depends on <ul style="list-style-type: none"> - water texture (wavy vs. calm) - incident angle of radiation - polarisation of light - frequency of radiation

The instantaneous albedo a satellite experiences varies significantly based on the cloud coverage and surface type directly beneath the satellite. As illustrated in Figure 9, a satellite only has a small portion of the Earth in its view.

The radius of the disc of the Earth that is visible to a satellite in an orbit with altitude h can be calculated using the angle ρ as defined in Equation 1. Using ρ , and considering Figure 15, the radius of the disc of Earth that is visible to the satellite can be calculated as

$$R_{FOV} = \left(\frac{\pi}{2} - \rho\right) * R_E = \left(\frac{\pi}{2} - \text{asin}\left(\frac{R_E}{R_E + h}\right)\right) * R_E \quad (17)$$

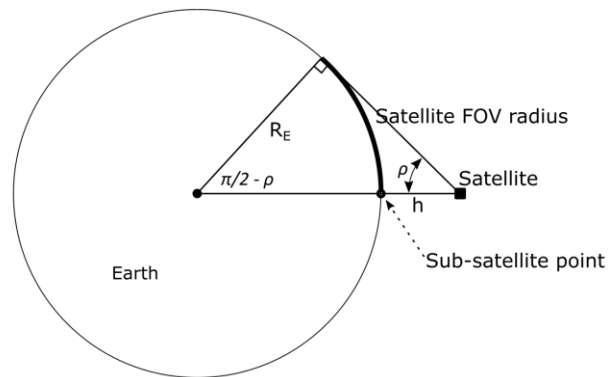


Figure 15: Radius of satellite FOV of Earth

For an ISS orbit with altitude of roughly 400 km, and an average radius of Earth of 6 371 km, the R_{FOV} can be calculated as 2 200 km. A satellite in this orbit will therefore have less than 3% of the Earth's surface in its field of view (FOV) at a time. At any particular time the part of the Earth that is visible to a satellite can therefore be dominated by a single type of large surface such as sea or desert, or it can consist of a variety of surfaces such as cities, lakes, forests, etc. One can therefore expect the average reflectance, and the albedo, to vary with orbital position. Albedo is further dependant on the incident

angle between the Sun, the Earth, and the satellite. The β -angle, as described in Figure 16, determines the angle at which sunlight is reflecting off of the surface of the Earth towards the satellite.

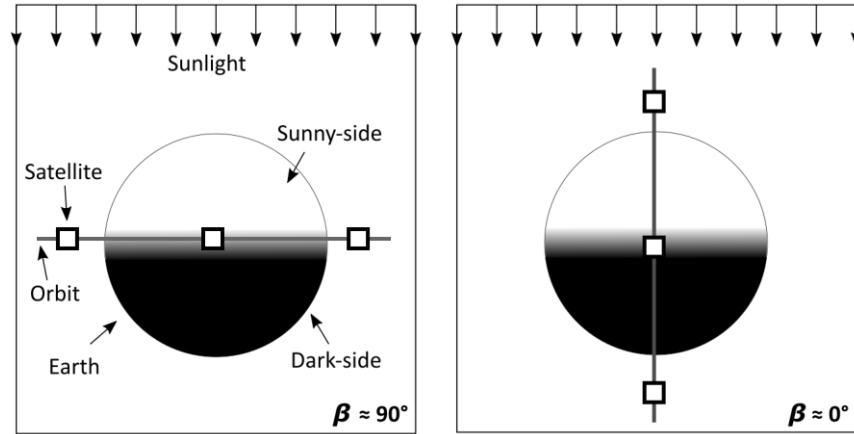


Figure 16: Effect of β -angle on albedo

Figure 16 shows the two extreme cases for the β -angle where the Sun falls within the satellite orbital plane, and where the Sun is orthogonal to the orbital plane. By simple examination of these figures it can be deduced that in the 90° case, the angle at which light reflects off of the Earth towards the satellite will be close to constant, whereas in the 0° case this angle will vary with a cyclic nature. Apart from this cyclic nature, the intensity of the albedo varies with a complex, non-linear relationship between the Sun, Earth and satellite, due to complex interactions with the atmosphere.

In order to study these complex relationships, dedicated NASA missions have been flown like the Earth Radiation Budget Experiment (ERBE) and the NOAA Sun-synchronous satellites [26]. These satellites collected incident sunlight, albedo and Earth longwave radiation using an array of instruments.

The data collected during these missions were used to create a model presented in [17]. The model uses the solar Zenith angle defined in Figure 12 to calculate the albedo irradiance on a Nadir facing panel by introducing a solar-Zenith-angle-dependent albedo reflectance factor, $a(\xi)$, so that

$$E_r = a(\xi) S \cos \xi \quad (18)$$

where S is the direct solar irradiance on a surface facing the Sun.

With the simplest model, without experimental corrections, the albedo irradiance on a surface scales with the cosine of the solar Zenith angle, and the albedo reflectance value remains constant. The average constant albedo reflectance factor according to [17] as well as other common references such as [20], is

$$\bar{a} = a(0) = 0.3 \quad (19)$$

The model based on the ERBE experiment introduces the solar-Zenith-angle-dependent correction factor $a(\xi)$ to account for complexities in the reflectance of typical Earth surfaces. According to [2], the albedo in some cases is at a minimum when the Sun is overhead ($\xi = 0$), since at these angles sunlight more effectively penetrates clouds and liquid surfaces like oceans and lakes, hence reflecting less energy back into Space. Conversely, lower solar Zenith angles result in higher albedo values if the area of Earth viewed by the satellite is covered with “dark (low albedo) trees growing over bright (high albedo) soil”. In these cases, the underlying soil which has high albedo is better illuminated with small solar-Zenith angles, and therefore results in higher albedo. Taking these and other effects into consideration, the following correction factor was introduced

$$a(\xi) = a(0) + C_1\xi + C_2\xi^2 + C_3\xi^3 + C_4\xi^4 \quad (20)$$

with ξ in degrees, and

$$\begin{aligned} C_1 &= 1.3798 \cdot 10^{-3}, \\ C_2 &= -2.1793 \cdot 10^{-5}, \\ C_3 &= 6.0372 \cdot 10^{-8} \text{ and} \\ C_4 &= 4.9115 \cdot 10^{-9}. \end{aligned}$$

The albedo fraction of direct sunlight with and without the solar-Zenith-correction factor is shown in Figure 17.

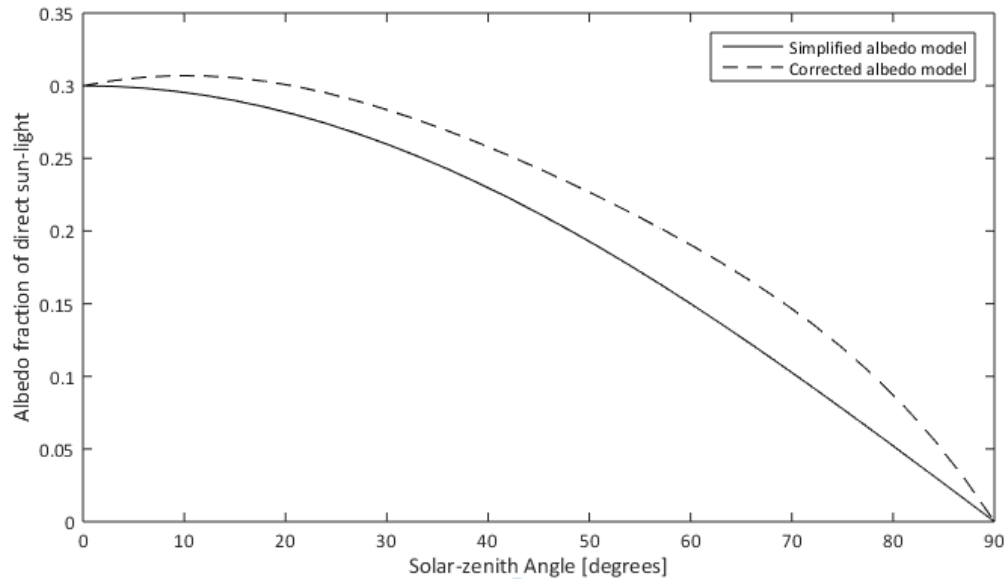


Figure 17: Albedo with and without solar-Zenith-angle correction

The above calculation is for a surface facing Nadir. For a panel facing off-Nadir, the total albedo heat transfer will be

$$Q_{albedo} = a(\xi) S \alpha \cos\xi F_e \quad (21)$$

with F_e the Earth VF as defined in Section 4.4, and α is the solar absorptivity of the surface.

4.3 Earth IR

Even when the satellite is not in the Sun-illuminated side of the orbit, the Earth is still radiating energy according to Planck's law and therefore transferring heat to/from the satellite. The intensity of the radiation the satellite receives depends on the exact part of the Earth's surface the satellite is above. The ocean, forests and desert all have a different emissivity and surface temperature and will therefore have different levels of radiation. The NASA CERES experiment gathered significant scientific measurements of the Earth IR and albedo in the upper atmosphere, and [27] compares these measurements to typical assumptions made for models of these values.

A surface model that contains different emissivity and temperature values for different latitude/longitude locations introduces a lot of complexity, without necessarily having a significant effect on the result of the simulation. Furthermore, the unpredictability of cloud coverage makes it unfeasible to have such a detailed IR model of the Earth.

Instead, an average temperature and emissivity is assumed for Earth's surface which according to [20] results in an average energy flux from the Earth's surface of $q_{surface} = 237.21 \text{ W} \cdot \text{m}^{-2}$.

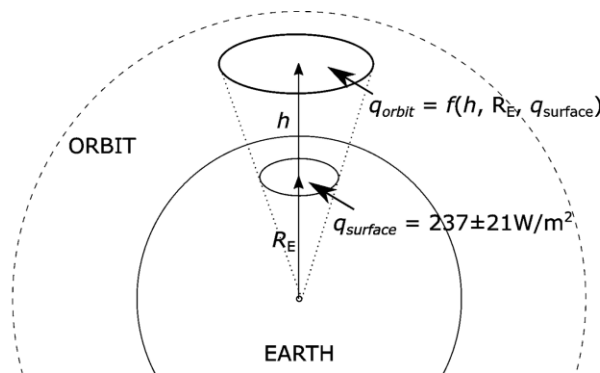


Figure 18: Earth IR energy flux at orbital height

The Earth IR energy flux at orbital height is a fraction of the flux at the surface, in the same ratio as the area of the spheres at the surface of the Earth and the orbit as shown in Figure 18.

The area of the sphere of the surface of the Earth is

$$A_{surface} = 4\pi R_E^2 \quad (22)$$

Similarly, the area of the sphere at the orbital height is

$$A_{orbit} = 4\pi(R_E + h)^2 \quad (23)$$

The energy flux at the orbital height is then

$$\begin{aligned} q_{orbit} &= q_{surface} \frac{A_{surface}}{A_{orbit}} \\ &= (237 \pm 21) \frac{R_E^2}{(R_E + h)^2} \text{ W} \cdot \text{m}^{-2} \end{aligned} \quad (24)$$

Given a surface on the satellite with area A_{sat} , the total Earth IR heat transfer rate to the surface is

$$\dot{Q}_{IR} = \varepsilon_{sat} F_e A_{sat} q_{orbit} \quad (25)$$

where F_e is the VF of the surface to the Earth, as discussed in Section 4.4, and ε_{sat} is the emissivity of the surface.

4.4 Earth View Factor

The amount of radiation a surface that is rotated off-Nadir will receive also depends on the orientation of the surface. A surface pointing Nadir will have a large part of its FOV facing the Earth, which is the direction the radiation is coming from. A surface that is rotated at a 90° angle relative to Nadir will have deep space in most of its FOV, and the Earth only in a smaller part towards the edge of its FOV. This is illustrated in Figure 19.

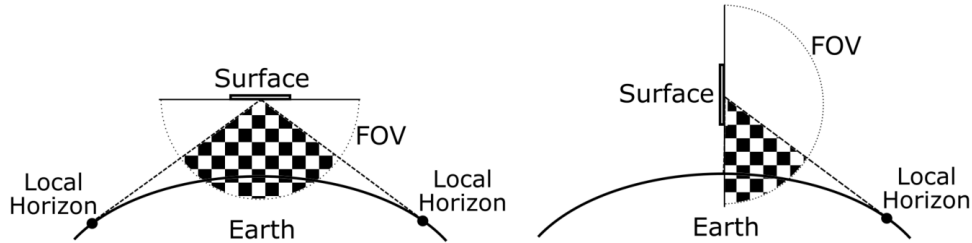


Figure 19: Earth VF for Nadir (left) and off-Nadir pointing (right)

This VF of one surface to another determines the fraction of the heat radiated from the one surface that reaches the other. Calculation of the VF between a flat plate and the Earth has been studied in multiple papers, but an analytical solution was formulated in [28] specifically for plates that are rotated off-Nadir. The study defines a coordinate system as shown in Figure 20.

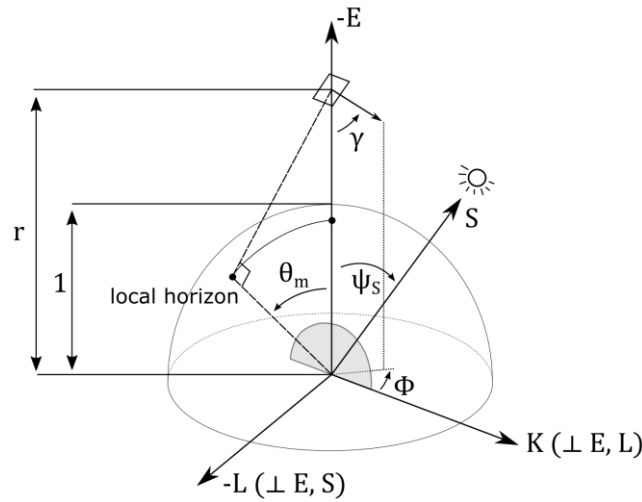


Figure 20: Coordinate system for VF calculation

The study defines three discrete cases for which three different solutions apply, and these three cases are illustrated in Figure 21.

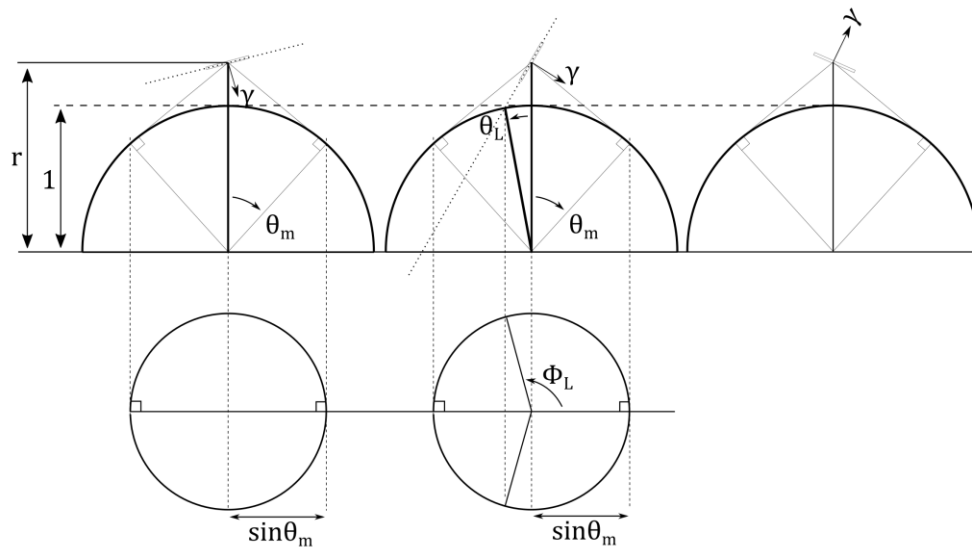


Figure 21: Three different cases for calculating VF between plate and Earth

The three cases correspond to:

- 1) $0 \leq \gamma \leq \theta_m$: A full Earth disc is visible from the center of the plate
- 2) $\theta_m \leq \gamma \leq \pi - \theta_m$: A partial Earth disc is visible from the center of the plate
- 3) $\pi - \theta_m \leq \gamma \leq \pi$: The Earth is NOT visible to the surface

For each of these three cases, a different solution to calculate the VF (F_e) is used. To calculate F_e , the ratio η_L is defined as

$$\eta_L = (\phi_L - \sin\phi_L \cos\phi_L)/\pi \quad (26)$$

with

$$\phi_L = \begin{cases} \cos^{-1}(-\sin\theta_L/\sin\theta_m), & \theta_m < \gamma < \pi/2 \\ \frac{\pi}{2}, & \gamma = \pi/2 \\ \cos^{-1}(\sin\theta_L/\sin\theta_m), & \pi/2 < \gamma < \pi - \theta_m \end{cases} \quad (27)$$

The VF is then calculated as

$$F_e = \begin{cases} \frac{1}{r^2} \cos\gamma, & 0 \leq \gamma \leq \theta_m \\ \frac{\eta_L}{r^3}, & \theta_m < \gamma < \pi - \theta_m \\ 0, & \pi - \theta_m \leq \gamma \leq \pi \end{cases} \quad (28)$$

where

$$r = \left(\frac{R_E + h}{R_E} \right) \quad (29)$$

The paper further discriminates between cases where the Sun/eclipse terminator is in the FOV of the surface, but for the purposes of this study these effects are ignored as they are only relevant for short periods of the orbit, when in polar orbits.

In the simulation environment vectors to the satellite, celestial bodies, and the normal vectors of all surfaces are available in the body reference and orbital coordinate systems, and the physical angles required to calculate the above VF can be calculated from these vectors.

For surface i with a normal vector n_i , the dot product with the vector from the Earth's center to the satellite is

$$\mathbf{e}_{sat}^{ORC} \cdot \mathbf{n}_i^{ORC} = \cos(\gamma_i) \quad (30)$$

The angle γ_i is then calculated as

$$\gamma_i = \text{acos}(e_{sat}^{OCR} \cdot n_i^{OCR}) \quad (31)$$

For all surfaces θ_m is the same, since it only depends on the satellite altitude. θ_m is calculated as

$$\theta_m = a \sin\left(\frac{\sqrt{r^2 - 1}}{r}\right) \quad (32)$$

To calculate θ_l the variable t is defined as

$$t = \frac{\sin(\gamma) - \sqrt{1 - r^2 \cos^2(\gamma)}}{(r + 1)|\cos(\gamma)|} \quad (33)$$

θ_l is then calculated as

$$\theta_l = a \sin\left(\frac{2t}{1+t^2}\right) \quad (34)$$

4.5 Deep Space and Celestial Bodies

The temperature of deep space has been measured by multiple satellites throughout the years to be roughly 2.7 K. This temperature is commonly referred to as the cosmic background radiation which is theorised to be a remnant of the Big Bang.

However, the effective temperature the radiating faces of the satellite are exposed to is not exactly equal to 2.7 K since parts of the view of deep space contains other bodies in our solar system, as well as stars, gas clouds, and other galaxies. To understand these effects better, the influence of objects in our solar system on a LEO satellite was studied.

The angular diameters of celestial objects as seen by the satellite's radiating faces are a function of their size and distance from the satellite.

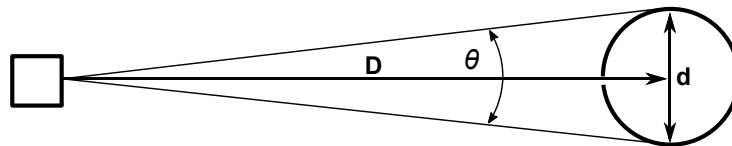


Figure 22: Angular diameter of celestial body

The angular diameter of an arbitrary object as seen from the satellite can be calculated as

$$\theta = 2 \operatorname{atan}\left(0.5d/D\right) \quad (35)$$

with

d the diameter of the celestial object and,

D the distance to the celestial object

as shown in Figure 22.

Table 2 shows the angular diameter of a list of objects of various types that can be found in the FOV of the satellite's radiator, as well as their varying average surface temperatures. The distances between these objects and the Earth are constantly changing as they move in their elliptical orbits around the Sun, and the Moon around the Earth. These distances vary from a local maximum to a local minimum periodically, but the exact maximum/minimum varies in a more complex manner. For the purpose of this chapter average recent values for the local maximum (denoted *far* in Table 2 and Table 3) and minimum (denoted *near* in Table 2 and Table 3) distances are used.

Table 2: Angular diameters and surface temperatures of nearby celestial bodies

Body	d (km)	D _{far} (km)	θ _{far} (deg)	D _{near} (km)	θ _{near} (deg)	T _{body} (K)
Sun	1.391M	152M	0.524	146M	0.546	5778
Moon	3474.2	405.7k	0.491	363.1k	0.548	100-400K
Venus	12104	261M	0.003	40M	0.017	735
Jupiter	139820	968M	0.008	588M	0.014	130

The heat transfer to/from the satellite radiator can be calculated by summing the heat transfer to deep space, as well as other celestial bodies considering their temperatures as well as their VFs. The VF to a specific celestial body can be calculated as the area occupied by the object in the FOV of the radiator, as a fraction of the total spherical area around the radiator.

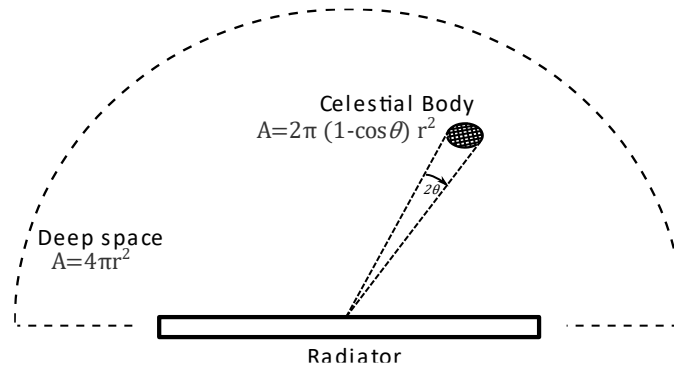


Figure 23: Average environment temperature calculation

Taking a unit sphere around the radiator as shown in Figure 23 and calculating the fraction of the area on the sphere that the object occupies, the VF from the radiator to the celestial bodies can be calculated.

$$\begin{aligned}
 F &= \frac{A_{body}}{A_{unit}} \\
 &= \frac{2\pi(1 - \cos\theta)r^2}{4\pi r^2} \\
 F &= \frac{(1 - \cos\theta)}{2} \quad (36)
 \end{aligned}$$

If we assume blackbodies for the purposes of this chapter, the radiative heat transfer from any of the celestial bodies to the satellite is then calculated as

$$\dot{Q} = \sigma A_1 F_{1 \rightarrow 2} (T_1^4 - T_2^4) \quad (37)$$

If we assume a satellite radiator at 20 C (293.15 K), and a radiator area of 1 m², the heat transfer to the various bodies in Table 2 can be calculated as shown in Table 3.

Table 3: Heat transfer from celestial bodies

Body	$\dot{Q}_{far} (W)$	$\dot{Q}_{near} (W)$
Sun	1323.12	1434.1
Moon	0.02661	0.03322
Venus	8.9e-6	0.00038
Jupiter	8.4e-8	2.3e-7

Furthermore, the heat transfer to deep space can be calculated, assuming a VF of 1 from the radiator to deep space.

$$\dot{Q}_{deepspace} = \sigma(T_{radiator}^4 - 2.7^4) = 418.8 \text{ W} \quad (38)$$

The Sun is, as expected, the biggest source of heat to the radiator. The second highest source is the Moon when closest to the Earth, and at typical maximum temperature.

Using the above results, the Moon supplies roughly <0.01% of the amount of heat to the radiator, compared to the amount of energy that the radiator is radiating into deep space. The Moon is the celestial body with the largest source of heat apart from the Sun and its effects are still negligible compared to the heat radiated into deep space. The assumption is therefore made that the heat from the Moon and the other specific celestial bodies, as well as their location relative to the satellite, can be disregarded for the purpose of this analysis. The industry standard for the temperature of deep space, taking into account these effects, is to use 4 K in all directions [20]. For this study, $T_{deepspace}$ is therefor assumed to 4 K.

4.6 Electronic Heat Generation

Apart from the external sources of heat from the Sun and Earth, a satellite also produces heat internally due to the conversion of electrical energy to heat energy.

Satellites that are too small and simple for nuclear reactors rely completely on sunlight for the supply of electrical power. They use solar panels to convert solar radiation to electrical power, which they use to charge their batteries. The power in the batteries is then used to power the satellite subsystems. The electrical power the subsystems use is converted into other forms of energy, one of which is thermal. Others include mechanical energy in the form of the rotation of reaction wheels, and consequently the rotation of the satellite, mechanical energy in the form of thrusters propelling the spacecraft and electromagnetic energy in the terms of RF transmission from antennae.

The main parts of the satellite where heat is generated are shown in Figure 24.

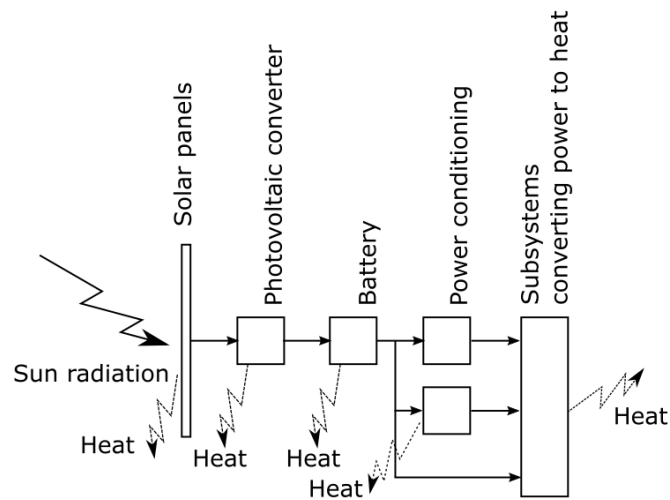


Figure 24: Flow diagram of energy transfer in a typical satellite

4.6.1 Solar Panel Efficiency

When sunlight falls on the solar panels, a fraction of the energy is reflected off of the surface of the panels and a fraction is absorbed. The solar cells convert the energy that is absorbed into electrical energy with a certain efficiency. This efficiency depends on the current drawn by the load connected to the panels. Typical CubeSat solar cells (usually produced by AzurSpace) have an efficiency of 28% [29].

The make-up of typical solar cells consists of a Polyimide PCB, GaInP/GaAs/Ge solar cells, and a glass cover (typically CMX100), which is illustrated in Figure 25.

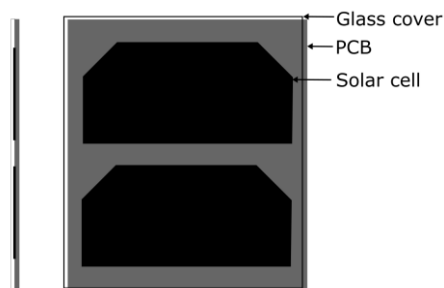


Figure 25: Construction of a typical CubeSat solar panel

The 100 μ m thick QIOptiq CMX 100 glass panels (which is used by some of the commercial CubeSat solar panel suppliers) has a transmission coefficient of 95%, a refractive index of 1.53, and an emissivity of 0.88. The bare polyimide PCB below the cover glass has emissivity of roughly 0.85 and solar absorptivity of 0.75. The Solar cells typically used on CubeSat panels have solar absorptivity of 0.86 and converts absorbed sunlight to electrical energy at roughly 28% efficiency. The other 72% of sunlight absorbed by the cell is turned into heat energy. The effect of this generated heat is further discussed in Section 5.3.

With S_{1U} the incoming solar energy on the 1U solar panel and A_{panel} and A_{cell} the area of the panel and the area of a single solar cell respectively, the amount of electrical power generated by the panel is

$$P_{solar} = 28\% * 0.95 * 0.86 * S_{1U} * \frac{2A_{cell}}{A_{panel}} \quad (39)$$

4.6.2 Photo-voltaic Converter Efficiency

The photo-voltaic (PV) converters on the EPS boost the voltages generated by the solar cells to match and exceed the battery voltage in order to charge the batteries. The efficiency does vary with load. For the nSight-1 mission typical input power is <5 W and a constant average of 0.95 efficiency is assumed. The heat generated by the photo-voltaic converter is therefore

$$Q_{PV} = 0.05 * P_{Solar} \quad (40)$$

and the amount of power delivered to the batteries are then

$$P_{charge} = 0.95 * P_{Solar} \quad (41)$$

4.6.3 Battery Efficiency

While batteries charge or discharge, they generate a certain amount of heat due to their internal impedance. For nSight-1, the GomSpace Nano Power batteries were used which have an internal impedance of 70 mΩ. When charging or discharging, the amount of heat generated by the batteries can be calculated as

$$Q_{Bat} = I_{Bat}^2 R_{Bat} \quad (42)$$

The loss due to internal resistance of the battery for each operational mode is discussed in Section 4.6.5 While the solar panels are fully illuminated, the batteries can charge at a significant current, and can generate a lot of heat. The heat generated by the battery (assuming a battery voltage of roughly 8 V) and solar generated power as discussed in 4.6.2 is

$$Q_{charge} = 70m\Omega * \left(\frac{P_{charge}}{8V}\right)^2 \quad (43)$$

4.6.4 Power Conditioning Efficiency

The satellite battery voltage is regulated to 3.3 V and 5 V which is the typical voltages used by CubeSat subsystems. The heat generated by the power regulators depend on the type of regulator used, and the associated efficiency thereof.

The losses associated with linear regulators are largely dependent on the input to output voltage relations. When converting from the battery voltage of 8.4 V to the subsystems

voltages of 5 V/3.3 V these losses become significant and is typically not feasible for systems with limited available power. For this reason, switching regulators are typically used on CubeSats. These regulators have efficiencies in the order of 85% and up for medium loads. For currents lower than 1000 mA efficiency of the converter has local minima and maxima, but variation is relatively small. The significant drop in efficiency in these regulators are at much larger currents than drawn during normal operations. Considering the power consumption values in Table 6, the buck converter efficiencies can be approximated as 92% for all modes.

The power consumption of the various subsystems is shown in Table 6. It also shows the current consumption at various voltages for each subsystem. Using the power conditioning efficiency discussed in Section 3.6.4 and Eq 22, the total current draw from the battery as well as the power lost in the regulators are also calculated.

If we define the efficiency of the regulator as η ,

$$P_{out} = \eta P_{in} \quad (44)$$

then,

$$I_{in} = \frac{P_{out}}{\eta V_{bat}} \quad (45)$$

This equation will be used in Section 4.6.5

4.6.5 Sub-System Power Consumption

The amount of heat generated by the satellite subsystems depends on which subsystems are active. The combination of subsystems that are active depend on the operational mode of nSight-1 which can be split into unique cases that are summarized in Table 4.

Table 4: nSight-1 main operational modes

Case	ADCS Mode	Payload	GS Overpass
Mode 1	Y-Spin	N	N
Mode 2	Y-Momentum	N	N
Mode 3	Y-Momentum	N	Y
Mode 4	Y-Momentum	Y	N

For each of these operational modes the various subsystems are switched on with a particular duty cycle, which is shown in Table 5.

Table 5: Average duty cycle of sub-systems for typical control modes (values in %)

	EPS	OBC	VHF/UHF Receiver	VHF/UHF Transmitter	CubeControl	CubeSense	CubeWheel	CubeTorquers	Payload Camera
Mode 1	100	100	100	1	100	0	0	2	0
Mode 2	100	100	100	1	100	100	100	4	0
Mode 3	100	100	100	70	100	100	100	4	0
Mode 4	100	100	100	1	100	100	100	4	100

The power consumption of the various subsystems is shown in Table 6 as well as the effective battery current to deliver this power and the total regulator losses.

Table 6: Power consumption of fully switched on subsystems

	EPS	OBC	VHF/UHF Receiver	VHF/UHF Transmitter	CubeControl	CubeSense	CubeWheel	CubeTorquers	Payload Camera
3.3V Power [mW]	165	165	184.8	0	231	33	69.3	0	0
5V Power [mW]	0	0	0	2815	0	75	0	1150	1418
Vbat Power [mW]	0	0	0	0	0	0	57.4	0	0
Total Power [mW]	165	165	184.8	2815	231	108	126.7	1150	1418
Total Battery Current (0.92 Efficiency) [mA]	21.9	21.9	24.5	373.1	30.6	14.3	16.2	152.4	188.0
Total Regulator Losses [mW]	13.2	13.2	14.8	225.2	18.48	8.6	5.5	92	113.4

Given the duty cycles in Table 5, and the values in Table 6, the average power consumption for different modes are calculated in Table 7, average regulator losses in Table 8, and average battery current in Table 9.

Table 7: Power consumption for operational modes (values in mW)

	EPS	OBC	VHF/UHF Receiver	VHF/UHF Transmitter	CubeControl	CubeSense	CubeWheel	CubeTorquers	Payload Camera	Total
Mode 1	165	165	184.8	28.2	231	0	0	23	0	797.0
Mode 2	165	165	184.8	28.2	231	108	126.7	46	0	1054.7
Mode 3	165	165	184.8	1970.5	231	108	126.7	46	0	2997
Mode 4	165	165	184.8	28.2	231	108	126.7	46	1418	2472.7

Table 8: Regulator losses for operational modes (values in mW)

	EPS	OBC	VHF/UHF Receiver	VHF/UHF Transmitter	CubeControl	CubeSense	CubeWheel	CubeTorquers	Payload Camera	Total
Mode 1	13.2	13.2	14.8	2.3	18.48	0.0	0.0	1.84	0	63.8
Mode 2	13.2	13.2	14.8	2.3	18.48	8.6	5.5	3.68	0	79.8
Mode 3	13.2	13.2	14.8	157.6	18.48	8.6	5.5	3.68	0	235.2
Mode 4	13.2	13.2	14.8	2.3	18.48	8.6	5.5	3.68	113.4	193.2

Table 9: Battery current for operational modes (values in mA)

	EPS	OBC	VHF/UHF Receiver	VHF/UHF Transmitter	CubeControl	CubeSense	CubeWheel	CubeTorquers	Payload Camera	Total
Mode 1	21.9	21.9	24.5	3.7	30.6	0	0	3.0	0	105.6
Mode 2	21.9	21.9	24.5	3.7	30.6	14.3	16.2	6.1	0	139.2
Mode 3	21.9	21.9	24.5	261.2	30.6	14.3	16.2	6.1	0	396.7
Mode 4	21.9	21.9	24.5	3.7	30.6	14.3	16.2	6.1	188.0	327.2

The values in Table 7 are used in the simulation as the heat generated by each node for a particular operational mode. The regulator losses in Table 8 are added to the EPS power consumption, since the regulators are also located on the EPS. The battery currents in Table 9 are compared to the in-flight data in Section 6.

In addition to this, EPS heats up significantly because of PV Converter inefficiencies and battery charge losses as described in 4.6.2 and 4.6.3. These are all added to the EPS heat generation in the simulation by calculating charge currents as incident solar energy on the solar panels change.

5 Satellite Thermal Model

A lumped capacitance thermal model was used to model the satellite. The satellite was divided into fixed control volumes (referred to as nodes for the rest of the document), connected to each other through a combination of conductive and radiative thermal connections. The model excludes radiative connections between nodes with very small VFs and between nodes with very large conductive thermal resistances.

This chapter visually illustrates the various thermal nodes, and their connections. It also provides detail on how thermal resistances were calculated. Due to the limited scope of this study, approximated and simplified average cross-sectional areas are used when calculating the thermal resistance of structural members. At the end of this chapter, a complete list of all the defined thermal nodes are given, with the material properties of each.

5.1 Thermal Node and Resistance Definitions

The structural frame of the satellite consists of four Aluminium side frames, connected to each other by eight Aluminium ribs. The parts of the structure are split into smaller sections, that each form a thermal node. The allocation of these nodes is done in a way that creates a boundary where a temperature gradient is expected.

Only the contact thermal resistances (e.g. R_{1-17} , R_{15-32} , etc) are shown in Figure 26. Each of the nodes that are on the same bracket are also connected with a conductive thermal resistance (e.g. R_{1-2} , R_{15-16} , etc), but these are not shown for simplicity of the illustration. The full list of thermal resistances for all nodes are shown in Table 32.

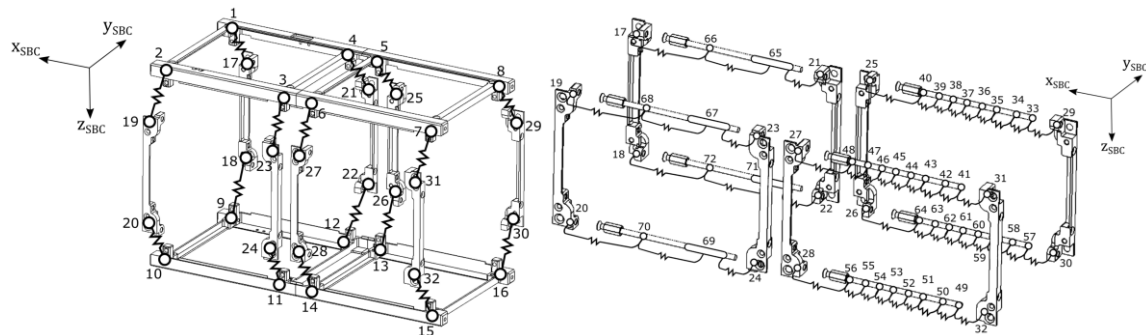


Figure 26: Thermal nodes of structure

The PC104 size boards which make up the electronic bus of the satellite, are mounted in the structure by stacking them on stainless steel stack rods, that span between the ribs as shown in Figure 26. The boards are stacked on these rods with Aluminium spacers to separate them. A thermal node is added at each point of contact between a board and one of the rods.

Each board in the stack is modelled as a single thermal node as shown in Figure 27. Each of these nodes are connected to the nodes on the stack rods at the corners of the boards, through conduction through the PCB and contact resistance between the PCB and the stack rod as shown in Figure 28. Adjacent boards are connected to each other both radiatively as well as conductively through the PC104 connectors.

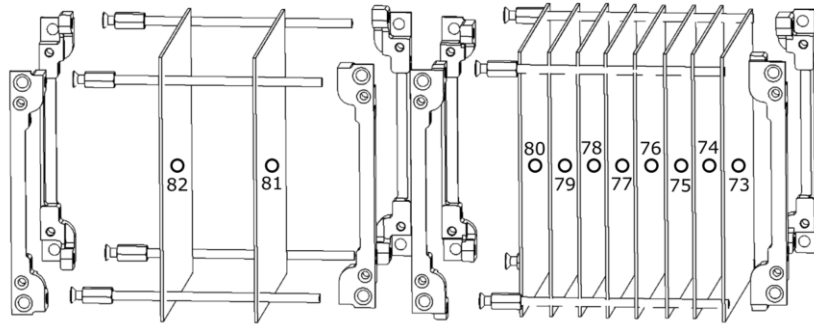


Figure 27: Thermal nodes of PCBs

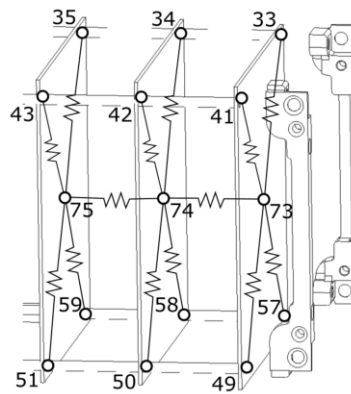


Figure 28: Example of thermal connections between PCBs and stack rods

The top panel should never experience much of a temperature gradient, so it is modelled as a single thermal node as shown in Figure 29.

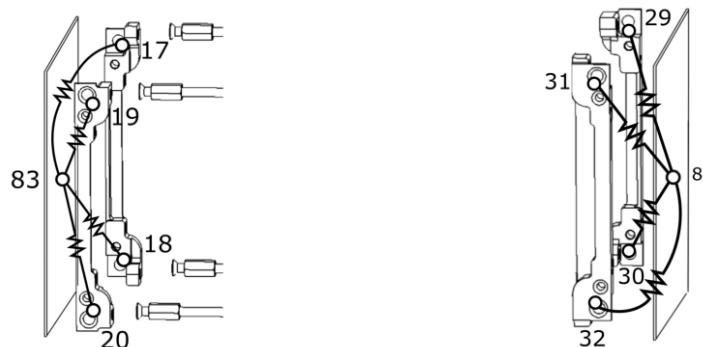


Figure 29: Thermal connections between X+ and X- panels and structure

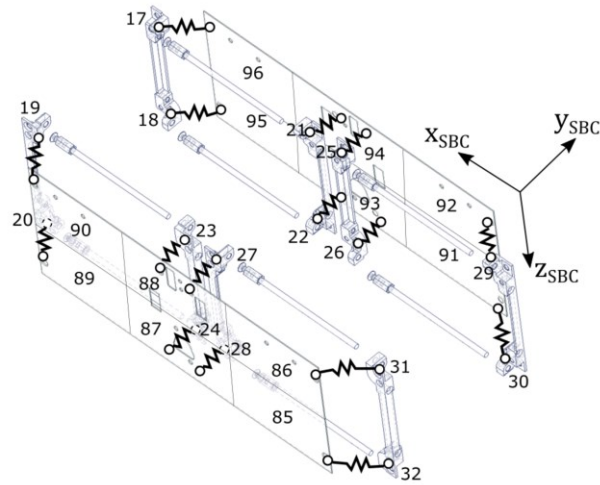


Figure 30: Thermal connections between Y side panels and structure

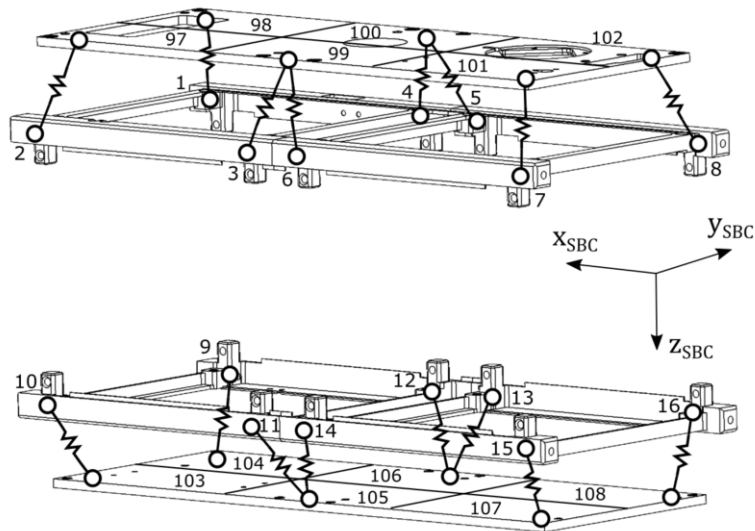


Figure 31: Thermal connections between X side panels and structure

nSight-1 has deployable solar panels on the $\pm Y_{SBC}$ faces as shown in Figure 32. These panels deploy to an angle of 45° , to ensure that the satellite receives at least some sun on the panels throughout its orbital lifetime. The panels are each assigned a single node.

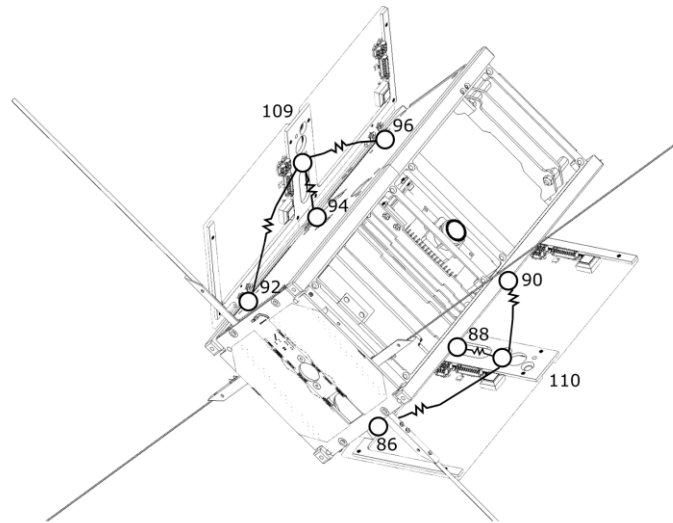


Figure 32: Deployable solar panel thermal nodes

One of the most important sensors in a CubeSat ADCS is the magnetometer. It is used in all control modes, and the accuracy of its measurements directly influences the accuracy of the control. The magnetometer would ideally only measure the Earth's geomagnetic field. However, in practice, it is disturbed by

- ferrous parts in the satellite which disturbs the local geomagnetic field,
- permanent magnetic dipoles on ferrous parts of the satellite which create a secondary permanent magnetic field, and
- locally generated magnetic fields which occur due to electrical currents that flow in the satellite.

To reduce the effect of all the above, the magnetometer must be placed as far as possible from these sources of disturbance. This is achieved by placing the magnetometer on a deployable boom. During launch it is in the stowed state, and then deployed once in orbit. The mechanism consists of

- an Aluminium frame/base,
- a brass deployment boom, containing insulated copper wires, and
- an Aluminium head, containing a PCB with electronics.

The magnetometer is shown in the stowed and deployed state in Figure 33.

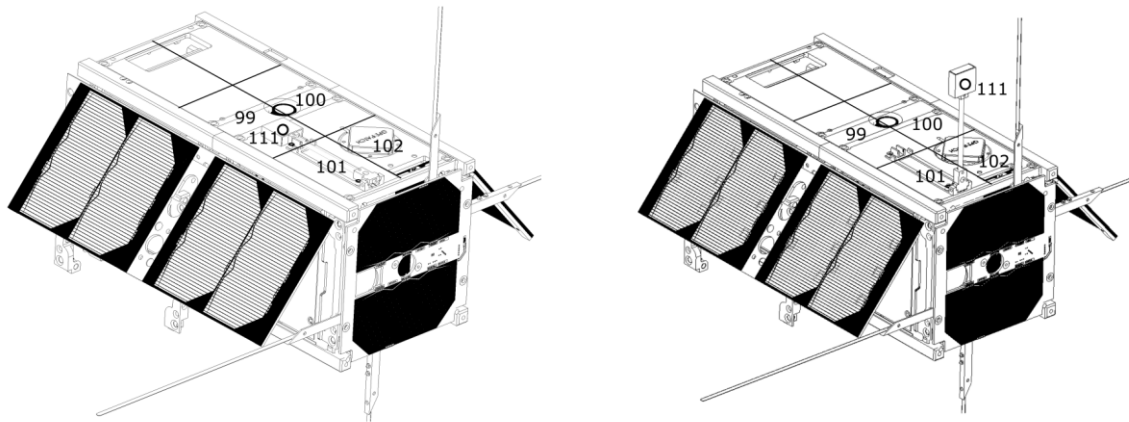


Figure 33: Deployable magnetometer in stowed (left) and deployed state (right)

5.2 Thermal Resistance Values

5.2.1 Structure

To be able to find the heat transfer rates between the various nodes in the model, we construct a thermal resistor network connecting all the nodes together. The resistances between nodes are one or a combination of the following three types:

1. conduction between nodes on the same part,
2. contact resistance between two different parts, and/or
3. radiation between two different parts.

The thermal resistance of a conductive connection between nodes on the same part can be calculated using Eq 13 with geometry as illustrated in Figure 34.

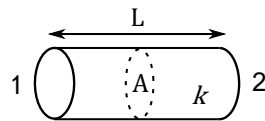


Figure 34: One dimensional conduction

Nodes 1-16 are all part of the same type of Aluminium 7075 T6 bracket. The geometry and cross-sectional area of this part is shown in Figure 35.

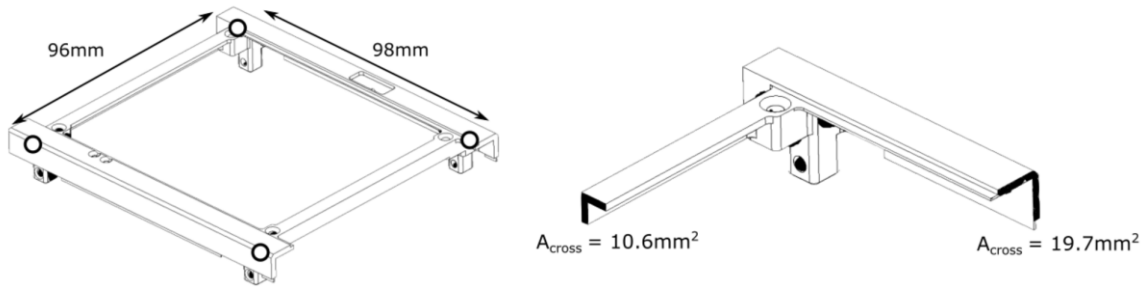


Figure 35: Z+ and Z- Structural bracket cross-section

Using Eq 13, the conductive thermal resistance along the long side of the bracket, as well as along the short side was then calculated as

Table 10: Z+ and Z- Structural bracket thermal resistance calculation

Side	L [m]	A [m ²]	k [W/K · m]	R [K/W]
Long	0.098	0.0000197	130	38.3
Short	0.096	0.0000106	130	69.7

Nodes 17-32 are all part of the same type of Aluminium 7075 T6 ribs. The geometry and cross-sectional area of this part is shown in Figure 36.

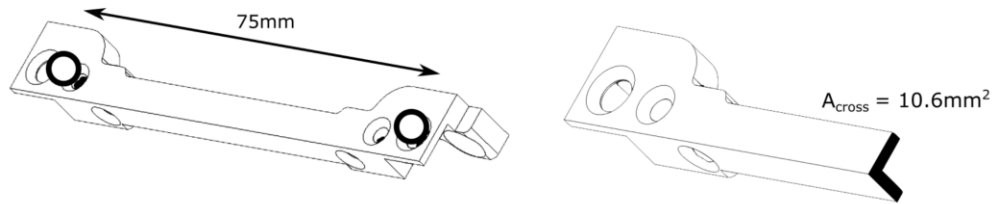


Figure 36: Y-Side structural rib cross-section

Using Eq 13, the conductive thermal resistance along the rib was calculated as shown in Table 11. Thermal conductivity values for Table 11 and Table 12 were taken from the Aerospace Specification Metals Inc supplier page [30].

Table 11: Y-Side structural rib thermal resistance calculation

Side	L [m]	A [m ²]	k [W/K · m]	R [K/W]
Long	0.075	0.0000106	130	54.4

Nodes 33-64 are all part of the 314 Stainless Steel rods that are used to stack the PCBs.

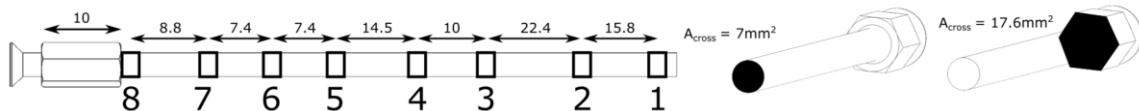


Figure 37: X- Stack rods cross-section (Dimensions in mm unless otherwise specified)

The eight PCBs are stacked on the rods with varying spacing between them. Each rod is divided into sections, with connection points between the rod and the PCBs labelled 1 to 8. The numbering of the connection points should not be confused with node numbers. Based on these spacings, the thermal resistances per single rod between the boards was calculated as

Table 12: X- Stack rods thermal resistance calculation

Section	L [m]	A [m ²]	k [W/K · m]	R [K/W]
1-2	0.0158	0.000007	17.5	129.0
2-3	0.0224	0.000007	17.5	182.9
3-4	0.0100	0.000007	17.5	81.6
4-5	0.0145	0.000007	17.5	118.4
5-6	0.0074	0.000007	17.5	60.4
6-7	0.0074	0.000007	17.5	60.4
7-8	0.0084	0.000007	17.5	68.6
8-	0.0100	0.0000176	17.5	32.5

The boards are spaced apart with 6mm OD Stainless Steel spacers with geometry as shown in Figure 38.

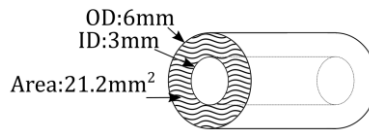


Figure 38: PCB Spacers

Following the same approach as above, the resistance of these spacers is:

Table 13: X- Stack spacers thermal resistance calculation

Section	L [m]	A [m ²]	k [W/K · m]	R [K/W]
1-2	0.0158	0.0000212	17.5	42.6
2-3	0.0224	0.0000212	17.5	60.4
3-4	0.0100	0.0000212	17.5	27.0
4-5	0.0145	0.0000212	17.5	39.1
5-6	0.0074	0.0000212	17.5	19.9
6-7	0.0074	0.0000212	17.5	19.9
7-8	0.0084	0.0000212	17.5	22.6

The S/S spacers in parallel with the S/S rods result in the following thermal resistances

Table 14: Total X- parallel stack resistance calculation

Section	R [K/W]
1-2	32.0
2-3	45.4
3-4	20.3
4-5	29.4
5-6	15.0
6-7	15.0
7-8	17.0
8-	32.5

Similarly, the two boards on the X+ side of the satellite are spaced as in Figure 39.



Figure 39: X+ Stack rods cross-section

The thermal resistance along these rods are then

Table 15: X+ Stack rods thermal resistance calculation

Section	L [m]	A [m ²]	k [W/K · m]	R [K/W]
- 1	0.0275	0.000007	17.5	224.5
1-2	0.0298	0.000007	17.5	243.3
2 -	0.0135/0.010	0.000007/0.0000176	17.5	142.7

Using the same S/S spacers as above

Table 16: X+ Stack spacers thermal resistance calculation

Section	L [m]	A [m ²]	k [W/K · m]	R [K/W]
- 1	0.0275	0.0000212	17.5	74.1
1-2	0.0298	0.0000212	17.5	80.3
2 -	0.0135	0.0000212	17.5	36.4

The resistance of the parallel assembly is then

Table 17: Total X- parallel stack resistance calculation

Section	R [K/W]
- 1	55.7
1-2	60.4
2 -	29.0

5.2.2 PCBs

The distribution of heat across the PCBs will be non-uniform, since individual high-power electronic components will generate significant heat in concentrated locations. A model that captures all the information on component placement and individual component power consumption falls outside of the scope of this study. Building such a model on its own would require significant research and would add a lot of complexity to the system thermal model.

For this reason, each PCB in the PC104 stack was modelled as a single node, located at the centre of the PCB. The thermal resistance between each of these nodes and the corners of the respective PCBs, is taken as equal in all four directions.

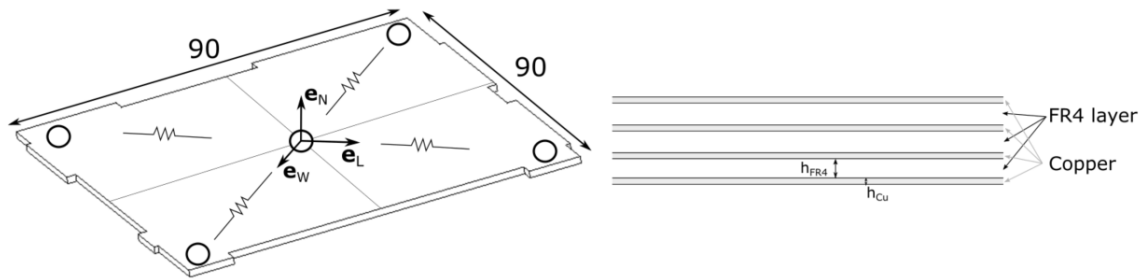


Figure 40: PCB Geometry and internal structure

The effective thermal resistance for the piece of PCB between the centre and the corners, were approximated by taking the average width of cross sections as shown in Figure 41.

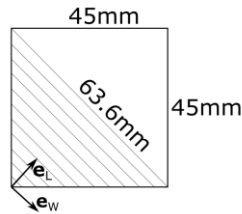


Figure 41: Approximation of conduction thermal resistance in PCB

The width in the e_W -direction varies in the e_L -direction

$$w(l) = \begin{cases} 2l & 0 \leq l \leq 31.8 \\ 127.2 - 2l & 31.8 < l \leq 63.6 \end{cases} \quad (46)$$

The average width from the centre to the corner is

$$w_{avg} = \frac{\int_0^{63.6} w(l) dl}{63.6} \quad (47)$$

Due to the geometric symmetry

$$w_{avg} = \frac{\int_0^{31.8} w(l) dl}{31.8} = \frac{\int_{31.8}^{63.6} w(l) dl}{31.8} = 31.8 \text{ mm} \quad (48)$$

The PCBs consist of layers of FR4 glass-reinforced epoxy laminate, with copper layers and tracks in-between (Figure 40). The copper and FR4 layers form parallel thermal paths conducting heat from the core to the corners of the PCBs. However, the layers are also connected to each other along the path of conduction, and an accurate way of modelling this structure is illustrated in Figure 42.

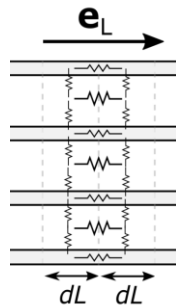


Figure 42: Accurate model 2-Dimensional flow through laminate PCB

The FR4 layers are roughly 0.4 mm thick, and the coppers layers are 50 μm each. The thermal resistance of each layer, the layer thickness and w_{avg} calculated above, are shown in Table 18.

Table 18: PCB layer thermal resistance

Layer	W [m]	H [m]	L [m]	k [W/K·m]	R [K/W]
FR4	0.0318	0.0004	0.0636	0.25	20 000
Copper	0.0318	0.00005	0.0636	355	112.7

The largest portion of heat generated in electronic components is typically conducted away through the grounding legs of the components to the PCB copper layer, instead of to the body [31]. The copper layers on the outsides of the PCBs will have the electronic components directly connected to them. These layers usually have a network of tracks, instead of a solid layer to conduct heat across the board. Typically, PCBs contain a near-solid ground layer on one of the two inner layers. The outer layers are usually connected to these ground layers through Vias.

A PCB will therefore have at least one solid layer conducting heat across the board. The FR4 and the other layers will also conduct heat, and aid in the distribution of heat but it can

be assumed that it will be significantly smaller than the contribution of the solid copper layer. One of the objectives of this study is to determine if any subsystems exceed their maximum temperature specifications. A worst case estimate of the local temperature of the electronics on a PCB, is if we assume all the heat generated on the PCB is in the centre of the PCB (furthest from the corner rails which dissipates the generated heat), and with worst case (largest) thermal resistance to the corner rails. For this reason, we use the thermal resistance of a single copper layer to model the thermal conduction of heat in the PCB.

Node 83, is a 2 mm thick Aluminum plate with a tight PCB stack mounted on it. The connection of this plate is modelled in the same way the PCBs were modelled, except the plate is homogeneous 2mm thick aluminum, instead of the laminate structure of the PCBs. The thermal resistances from this node to the surrounding nodes were then calculated and is shown in Table 19:

Table 19: FIPEX mounting plate thermal resistances

	W [m]	H [m]	L [m]	k [W/K·m]	R [K/W]
FIPEX mounting plate	0.0318	0.002	0.0636	130	7.7

The PCBs are stacked parallel with varying spacing and radiates heat to each other. The heat transfer from one PCB to an adjacent PCB can be calculated using Eq 49 [32].

$$\dot{Q}_{1 \rightarrow 2} = \sigma \varepsilon_1 \varepsilon_2 A_1 F_{1 \rightarrow 2} (T_1^4 - T_2^4) \quad (49)$$

The VF for parallel plates of various configurations can be found in [33]. For square parallel plates of equal size ($w \times w$), that are aligned with each other and with spacing (h) between them, the equations in [3] can be simplified to

$$F_{1 \rightarrow 2} = \frac{2}{\pi X^2} \left[\ln \sqrt{\frac{(1 + X^2)^2}{1 + 2X^2}} + 2X \sqrt{1 + X^2} \tan^{-1} \left(\frac{X}{\sqrt{1 + X^2}} \right) - 2X \tan^{-1}(X) \right] \quad (50)$$

where

$$X = \frac{w}{h}$$

Nodes 73-81 all radiate to each other, and in accordance to Eq 50 the VFs between the plates were calculated and is shown in Table 20.

Table 20: VFs of PCBs to each other

Plates	Spacing [mm]	View factor
$F_{73 \rightarrow 74}$	15.8	0.72
$F_{74 \rightarrow 75}$	22.4	0.63
$F_{75 \rightarrow 76}$	10	0.81
$F_{76 \rightarrow 77}$	14.5	0.74
$F_{77 \rightarrow 78}$	7.4	0.85
$F_{78 \rightarrow 79}$	7.4	0.85
$F_{79 \rightarrow 80}$	8.8	0.83

To be able to use the same mechanism to integrate the temperatures of nodes that are connected through radiative thermal connections as used in conductive connections, equation 49 is rewritten as

$$\begin{aligned} \dot{Q}_{1 \rightarrow 2} &= \sigma \varepsilon_1 \varepsilon_2 A_1 F_{1 \rightarrow 2} (T_1^2 + T_2^2) (T_1 - T_2) \\ &= \sigma \varepsilon_1 \varepsilon_2 A_1 F_{1 \rightarrow 2} (T_1^2 + T_2^2) (T_1 + T_2) (T_1 - T_2) \end{aligned} \quad (51)$$

Also

$$\dot{Q}_{1 \rightarrow 2} = \frac{(T_1 - T_2)}{R_{1-2}} \quad (52)$$

We therefore define the radiative temperature dependent thermal resistance as

$$R_{1-2} = (\sigma \varepsilon_1 \varepsilon_2 A_1 F_{1 \rightarrow 2} (T_1^2 + T_2^2) (T_1 + T_2))^{-1} \quad (53)$$

5.2.3 Side Panels

The side panels of the satellite (both in Y_{SBC} and Z_{SBC}), as shown in Figure 30 and Figure 31, each are divided into six thermal nodes, each representing an equal size section of the panel as indicated in Figure 43.



Figure 43: Side panel thermal resistances

Heat conduction between these nodes occurs through their adjoining edges and the thermal resistances for these connections are shown in Table 21 with conductivity values taken from [34].

Table 21: Thermal resistances for conduction within side panels

Connection	W [m]	d [m]	L [m]	k [W/K · m]	R [K/W]
Long Edge (Y_{SBC} panel)	0.06666	0.0012	0.04	130	3.9
Short Edge (Y_{SBC} panel)	0.04	0.0012	0.06666	130	10.7
Long Edge (Z_{SBC} panel)	0.06666	0.003	0.04	109	2.0
Short Edge (Z_{SBC} panel)	0.04	0.003	0.06666	109	5.1

5.2.4 Deployable Solar Panels

The two deployable solar panels each consists of two 1U solar panels, mounted on an Aluminium frame, connected to the satellite body through two Aluminium hinges.

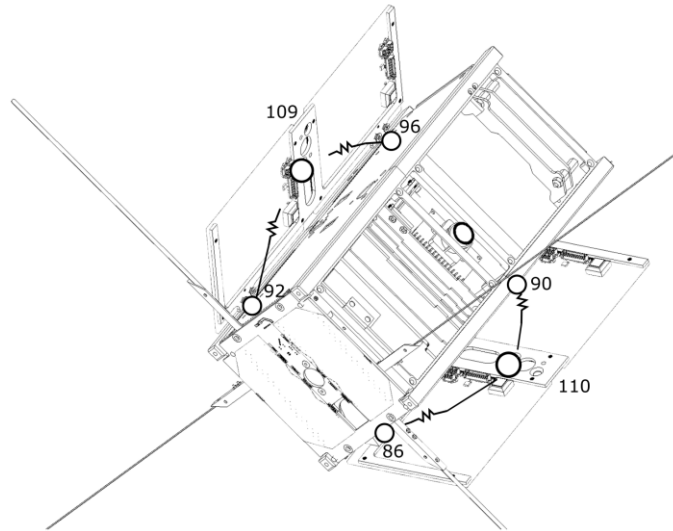


Figure 44: Deployable solar panel thermal resistance

Due to the symmetry, the simplified assumption was made that the temperature across the assembly will be constant in the direction of the longer axis of the panel, and that the two 1U panels will have similar temperature profiles. Each deployable solar panel assembly is modelled as a single thermal node.

One expects a temperature gradient across the panel in the shorter axis, since heat absorbed by the panels will flow to the satellite body through the panel polyamide backing and Aluminium frame. The heat-flow from the panel to the body is modelled as two conductive thermal resistances between the panel node, and the two nodes located at the hinges.

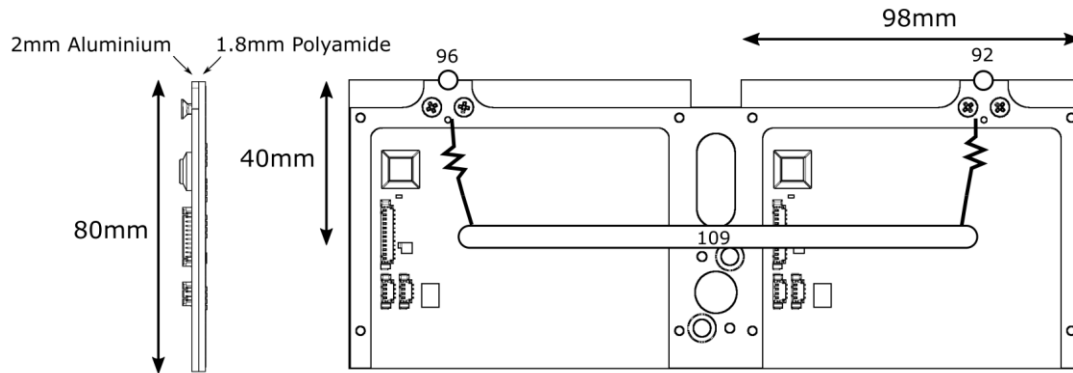


Figure 45: Deployable panel thermal resistance detail

The PCB of the solar panel consists of a 1.8 mm PCB, which contains a copper ground layer. Assuming a 50 μm copper layer, an estimated thermal resistance between the panel and each of the two hinges is calculated in Table 22.

Table 22: Thermal resistances of solar panel backings

Layer	W [m]	H [m]	L [m]	k [W/K · m]	R [K/W]
FR4	0.098	0.0018	0.04	0.25	907
Copper	0.098	0.00005	0.04	355	28.8
				Total	27.9

5.2.5 Deployable Magnetometer

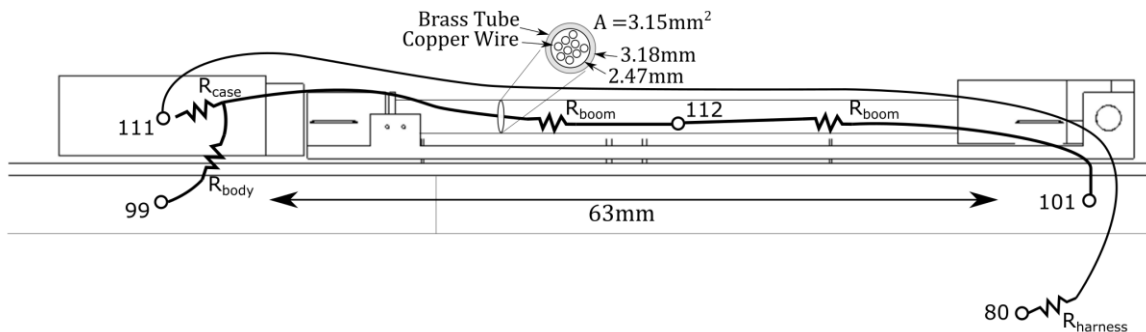


Figure 46: Deployable magnetometer thermal resistances

R_{case} : The magnetometer sensor is on a PCB, inside the head of the magnetometer. The PCB is connected to the case by means of epoxy with thermal conductivity of 38.1 W/mK . Total thermal resistance from the magnetometer to the case is roughly 0.5 K/W .

R_{boom} and $R_{harness}$: The case is connected to the deployment base, and to the panel on which it is mounted through a deployment boom consisting of a brass tube with dimensions as shown in Figure 46. The magnetometer chip is connected to CubeControl (Node 80)

through a harness with 11 connections, consisting of 22 AWG copper wire. The total harness length is roughly 120 mm. Thermal conductivity values taken from [34].

Resistance	$A_{\text{section}} [\text{m}^2]$	$L [\text{m}]$	$k [\text{W}/\text{K} \cdot \text{m}]$	$R [\text{K}/\text{W}]$
R_{boom}	0.00000315	0.063	109	183.5
R_{harness}	0.00000142	0.120	385	219.5

R_{body} : In the ideal stowed case the magnetometer has full contact with the side panel. In this case the only resistance between the case and the body is the thermal contact resistance. The magnetometer is held down with a polyethylene burn wire, which during integration, launch vibration and in-orbit thermal cycling may slightly stretch. As soon as the burn-wire stretches, the magnetometer head loses contact with the side panel.

In this case there is only radiative heat transfer between the case and the side panel. Due to the close proximity, the VF between the body and the bottom face of the case can be assumed to be 1. The total area of the bottom face of the magnetometer case is 276 mm². The radiative heat transfer between the magnetometer case and the brass is then

$$\dot{Q}_{\text{case} \rightarrow \text{body}} = \sigma \varepsilon_{\text{case}} \varepsilon_{\text{body}} A_{\text{case}} (T_{\text{case}}^4 - T_{\text{body}}^4) \quad (54)$$

5.2.6 Contact Resistance

When heat flows through an interface where two materials are in contact, there is a slight temperature drop across the interface due to thermal contact resistance. Thermal contact resistance exists because practical surfaces are never perfectly flat on a microscopic level, and because this uneven surface finish results in decreased contact area. The typical one-dimensional temperature profile for two solids in contact is shown in Figure 47.

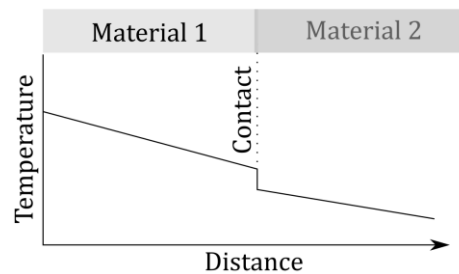


Figure 47: Temperature drop because of contact resistance

The concept of thermal contact resistance is one that has been widely researched, and a large amount of experimental research papers are publicly available. Due to the wide variation in surface finishes and contact geometry, no satisfactory general theory exists for predicting the contact resistance between arbitrary solids [35].

The surface roughness of the materials, and contact pressure are the most important factors in determining contact resistance. Surface roughness, as illustrated in Figure 48, decreases the contact area between two materials. The rougher the surface, the higher the contact

resistance. Increased contact pressure decreases surface resistance, due to deformation of the material to increase contact, especially by depressing microscopic peaks as illustrated in Figure 48.

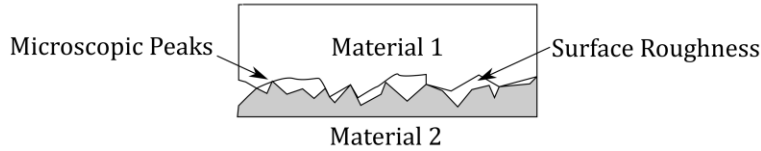


Figure 48: Exaggerated view of surface roughness

Another minor factor in the surface resistance is the air/liquid that fills the holes in the rough surface. However, in the vacuum environment of space, this is not applicable. Typical contact resistance for raw Aluminium under pressure, in a vacuum environment and with various fluids in the surface gaps are discussed in [35], [36] and [37] and surface thermal resistance values for anodized Aluminium is discussed in [38]. According to these, typical values for the thermal contact resistance for an Aluminium interface, with surface roughness of $2.54 \mu\text{m}$, and with air in the gaps in the surface texture, is in the order of magnitude of $< 1 \times 10^{-4} \text{ m}^2 \cdot \text{K/W}$.

Some of the smallest contact interfaces in the assembly is in the Aluminium brackets where, the total contact area is in the order of 200 mm^2 . Total thermal contact resistance is then in the order of magnitude, 0.5 K/W .

All assemblies in the satellite where there are contact interfaces, have bolts that fasten the two surfaces to each other. These bolts add significant further conduction between the two surfaces. It is concluded that a value of 0.5 K/W is a very conservative worst-case value.

5.3 Surface Properties

The thermal properties of each surface that is exposed to the space environment was analysed to determine the effective solar absorption and emissivity thereof. The accuracy of the thermal simulation is very sensitive to the properties of the outside surfaces, since it directly determines the amount of Sun-energy absorbed, Earth IR absorbed, and the rate at which the satellite radiates energy into deep space. The various materials used on the outside panels, as well as their surface finishes are discussed in the rest of this section. Thereafter the composition of each side panel is discussed.

The $+Y_{SBC}$ and $-Y_{SBC}$ side panels, as well as the science payload panel ($+X_{SBC}$), are made from Aluminium, with an Alodine 1200S chromium conversion coating produced by Henkel. This coating is commonly used as pre-treatment before painting but is also widely used as final surface finish. The main advantages of this coating for use in the Aerospace industry is its corrosion resistance, and its low electrical conductivity [39]. The average value for the emissivity and solar absorptivity of Alodine 1200S is shown in Table 26 [40].

Anodization is a passivation treatment that is widely used in the Automotive and Aerospace industries to creating a robust, non-conductive, corrosion resistance finish on Aluminium parts. During anodization an Aluminium oxide layer is grown on the surface of the Aluminium, by putting it through an electrolytic process. The electrolyte used varies for different applications, but Boric Acid is most commonly used in the Aerospace industry, including by respected organisations such as NASA. Typically, the anodization layer is opaque, but a dye can be added to the process to create a coloured surface. Typical values for clear and black anodized Aluminium are shown in Table 26.

The Zenith and Nadir panels ($\pm Z_{SBC}$) are both made of 3mm thick brass. The emissivity of brass varies substantially with its surface finish (i.e. polished/rolled/dull/machined). These panels were laser cut from brass stock sheets, and the visual appearance of the surface finish matches that of raw dull plate the best. Typical values are shown in Table 26.

The solar panels have a layered structure as shown in Figure 49.

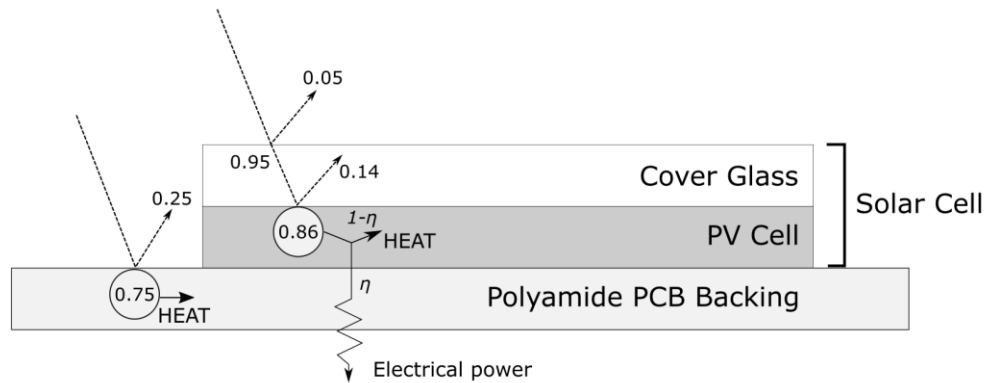


Figure 49: Solar panel layer structure

The cover glass is the outside layer of the solar panel and determines the emissivity of the solar cell assembly. Solar radiation that hits the panel is transmitted through the cover-glass with 95% efficiency as shown in the cover glass datasheet in Appendix B-4. The transmitted energy hits the PV cell, which has a solar absorptivity of 0.86. Of this absorbed energy, a portion is turned into electrical energy depending on the efficiency (η) of the solar cells, and the rest results in heat generated in the cell. From a thermal analysis perspective, the solar absorptivity of the solar cell is therefore actually less than 0.86, since not all absorbed energy is turned into heat. To compensate for this, the effective solar absorptivity α_{eff} was introduced and is calculated as shown in Eq 55. This is the approach followed in [19].

$$\begin{aligned}\alpha_{eff} &= 0.95\alpha(1 - \eta) \\ &= 0.57\end{aligned}\tag{55}$$

The effective solar absorption of the solar cell, as well as the emissivity is shown in Table 23.

Table 23: Emissivity and solar absorptivity of the solar cell

ϵ	α
0.88	0.57

PCBs usually come in two forms, glass-reinforced epoxy laminates, and polyamide. Polyamide boards are typically used in applications where specific thermal and shock environments are required and are as a result, widely used as backing for solar cells to form CubeSat solar panels. Typical values for such PCBs are shown in Table 24.

Table 24: Emissivity and solar absorptivity of bare Polyamide PCB

ϵ	α
0.89	0.75

Each solar panel has a structure as shown in Figure 50. The average values for the panel, considering the ratio of PCB to solar cell, are used in Table 26.

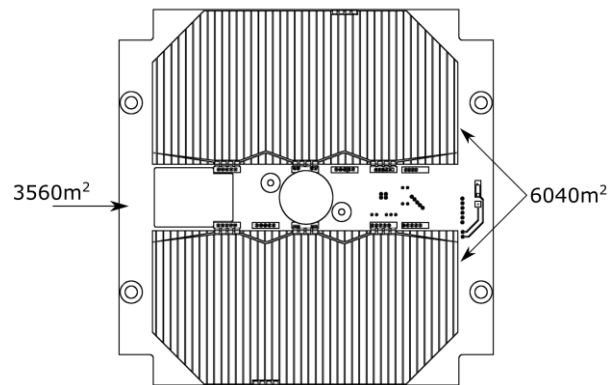


Figure 50: 1U Solar panel

Both the outside and the inside of the deployable $\pm Y_{SBC}$ panels are exposed to the space environment, and both sides of each panel must be modelled as separate surfaces.

The insides of these panels consist of the Alodined Aluminium frames on which the panels are mounted, the backsides of the panels, and parts that are covered in white velvet tape.

The Nadir and Zenith panels consist of portions that are covered in Aluminium tape, white velvet tape, solar panel, Alodined Aluminium, black anodised Aluminium, and lenses of cameras and sensors. The various surfaces are shown and marked with textures in Figure 51, and the textures are annotated in Table 25.

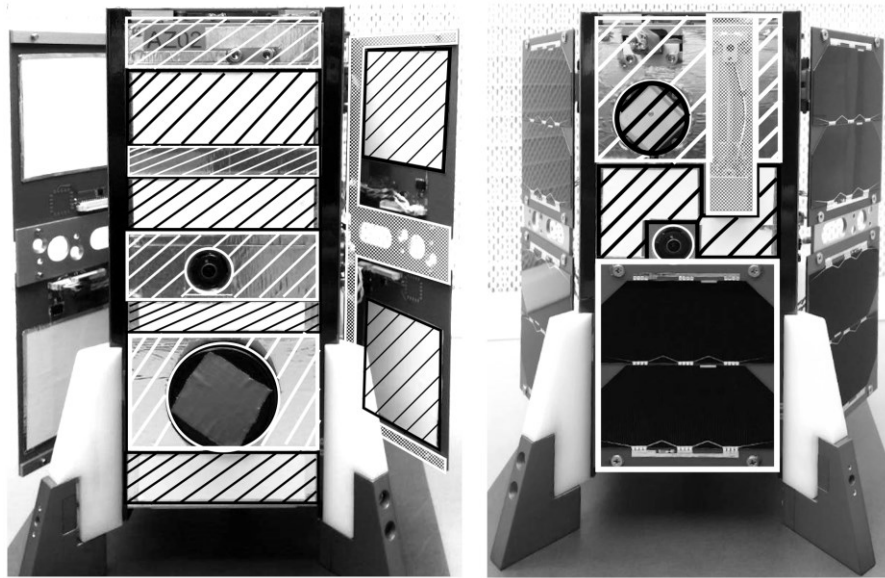


Figure 51: Nadir (left) and Zenith (right) panels

Table 25: Annotations of surfaces

Surface type	Annotation
3M-425 Aluminium Foil Tape	
White Velvet Tape	
Alodined Aluminium	
Bare Polyamide PCB	
Solar Panel	Picture of solar panel
Black Anodised Aluminium	

The percentages of each of these surfaces on each of the body panels are shown in Table 26.

Table 26: Average emissivity and solar absorption of body panels

ϵ	0.1	0.86	0.03	0.87	0.89	0.9	0.88		
α	0.4	0.86	0.2	0.3	0.75	0.95	0.64		
Side panel	Alodine 1200S	Anodized Aluminium (Black)	3M-425 Aluminium Foil Tape	3M 400 White Velvet	Polyamide PCB	Camera Lens	Solar Panel	Average Emissivity	Average Absorptivity
+ X_{SBC}	-	-	-	-	-	-	100%	0.88	0.64
- X_{SBC}	100%	-	-	-	-	-	-	0.10	0.40
+ Y_{SBC}	100%	-	-	-	-	-	-	0.10	0.40
+ Y_{SBC} deployable (+ Y_{SBC} side)	-	-	-	-	-	-	100%	0.88	0.64
+ Y_{SBC} deployable (- Y_{SBC} side)	26.3%	-	-	52.9%	20.8%	-	-	0.67	0.42
- Y_{SBC}	100%	-	-	-	-	-	-	0.10	0.40
- Y_{SBC} deployable (- Y_{SBC} side)	-	-	-	-	-	-	100%	0.88	0.64
- Y_{SBC} deployable (+ Y_{SBC} side)	26.3%	-	-	52.9%	20.8%	-	-	0.67	0.42
+ Z_{SBC}	-	8%	44.6%	39.4%	-	8%	-	0.50	0.35
- Z_{SBC}	9.7%	15.9%	15.9%	16.6%	-	-	41.9%	0.66	0.53

5.4 Surface Model

The surfaces of the satellite that are exposed to the space environment must be programmatically defined for the simulation to be able to calculate incoming solar radiation, IR radiation, albedo radiation, as well as radiation into deep space.

Surfaces are broken up into rectangular segments. Each segment has attributes as shown in Table 27.

Table 27: Attributes of a surface segment

Attribute	Description
Surface Member	Member identifier
Connected Node	Thermal node connected with this surface
Area	Area of surface
Emissivity	Emissivity of surface
Solar Absorptivity	Solar absorptivity of surface
CoP	<X, Y, Z> coordinate of center of pressure
N	<X, Y, Z> normal vector
Point 1	<X, Y, Z> coordinate of first vertex of surface
Point 2	<X, Y, Z> coordinate of second vertex of surface
Point 3	<X, Y, Z> coordinate of third vertex of surface
Point 4	<X, Y, Z> coordinate of fourth vertex of surface

The sequence in which the points of a surface segment is listed is used to determine the normal vector. The definition of the normal vector relative to the points was done as part of the existing EOS package, where it is used to calculate atmospheric drag. The definition is shown in Figure 52.

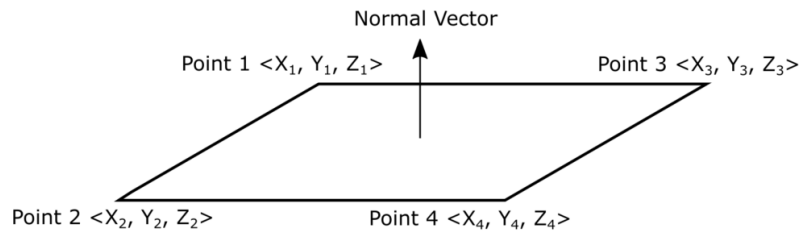


Figure 52: Normal vector of surface relative to vertices

A model of a complex satellite would contain at least 10 members and would therefore contain a very large number of vertices. Defining these vertices numerically in a table or an excel sheet is both time-consuming and difficult. To help easily create these models, a Surface Builder C# application was created. The application provides a GUI to:

- add/delete/edit surface members,
- visualize surface members,
- calculate and visualize normal vectors,
- automatically reorder vertices in a surface member to have its normal vector point, away from the CoM,
- save/load models,
- calculate the area of each surface,
- calculate the centre of pressure of each surface, and
- edit the other attributes of a surface member such as the name, connected nodes, emissivity and absorptivity.

A screenshot of the visual builder is shown in Figure 53.

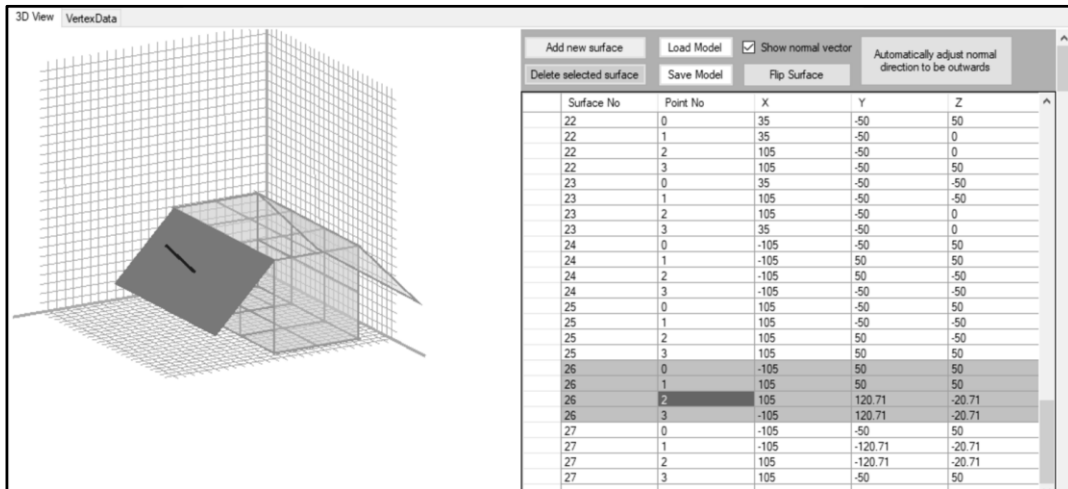


Figure 53: Screenshot of surface builder visualization

The automatic normal vector correction function is done by calculating the geometric center of the total model by averaging X, Y and Z coordinates of all points. The normal vector of each surface is then calculated according to the convention defined in EOS and is checked to ensure that it is pointing away from the geometric center. The vertices of each surface that has a normal vector pointing towards the geometric center is rearranged to flip the vector. A screenshot of the vertex data editor is shown in Figure 83.

5.5 Thermal Resistance Matrix Construction

Each thermal node can be connected to all other nodes radiatively and/or conductively through some total thermal resistance as shown in Figure 54.

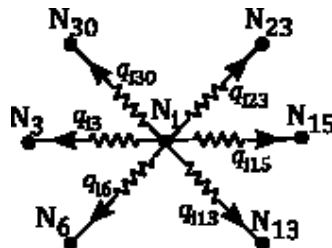


Figure 54: Thermal node heat fluxes

The connections between the thermal nodes can be represented by a matrix of thermal resistances.

	1	2	3	...	6	i	...	13	14	...	m
1											
2											
3											
...											
6											
i	R_{i1}	R_{i2}	R_{i3}	...	R_{i6}		...	R_{i13}	R_{i14}	...	R_{im}
...											
13											
14											
...											
m											

Figure 55: Generic structure of thermal resistance matrix

The net heat-flux out of node i can be written as:

$$q_i = \sum_{j=1}^m q_{ij} = \sum_{j=1}^m \frac{T_i - T_j}{R_{ij}} \quad (56)$$

5.6 Temperature Solver

According to the principle of conservation of energy the change in internal energy of a solid, incompressible control volume for a given timestep is shown in Eq 14 and repeated here for convenience.

$$\frac{\Delta U}{\Delta t} = \dot{Q} + \dot{Q}_v$$

where

U is the internal energy of a system,

\dot{Q} is the heat transfer rate to the control volume, and

\dot{Q}_v is the heat generation rate within the system.

For a such control volume with a fixed mass and fixed volume,

$$\Delta U = mc_v \Delta T \quad (57)$$

where

m is the mass of the control volume,

c_v is the specific heat capacity at constant volume, and

T is the temperature of the control volume.

Combining Eq 5714, and Eq 57 we get an equation relating the change in temperature of the control volume to the heat transfer rate and heat generation rate for a given timestep

$$\frac{\Delta T}{\Delta t} = \frac{\dot{Q} + \dot{Q}_v}{mc_v} \quad (58)$$

For an infinitely small timestep the instantaneous rate of change of the temperature of the node is then

$$\dot{T} = \frac{\dot{Q} + \dot{Q}_v}{mc_v} \quad (59)$$

The temperature of the node after a specific time t have elapsed since some reference time t_0 is found by integrating Eq 59

$$\begin{aligned} T(t) &= \int_{t_0}^t \dot{T} dt = \int_{t_0}^t \frac{\dot{Q} + \dot{Q}_v}{mc_v} dt \\ &= \int_{t_0}^t \frac{\dot{Q} + \dot{Q}_v}{mc_v} dt \end{aligned} \quad (60)$$

For a computer simulation the temperature must be calculated using a numerical integration method. For the sake of simplicity, only fixed timestep integration methods were considered. Of such methods, the Runge-Kutta methods are the most widely used and were chosen for this simulation.

Numerical integration of this nature may have significant errors and even be unstable for certain scenarios if not chosen correctly. These methods are specifically inaccurate on data with rapidly changing gradients, or when timesteps are large. During the simulation of the satellite's temperature, one such situation, where the gradient was large enough to induce significant errors, is with conduction within Aluminium parts such as the side panels of the satellite. In this case, the side panel is broken up into multiple nodes connected by very small thermal resistances and large changes in temperature gradients can occur, especially with discontinuous transition effects such as when the Sun 'appears' above the local horizon.

The simplest form of the Runge-Kutta method is the first order form, also known as the Euler method. The Euler method uses a first order fixed timestep to calculate the change in temperature. Eq 58 can be rewritten to

$$\Delta T = \frac{\dot{Q} + \dot{Q}_v}{mc_v} \Delta t \quad (61)$$

so that

$$T(t_0 + \Delta t) = T_0 + \frac{\dot{Q}(t_0, T_0) + \dot{Q}_v(t_0, T_0)}{mc_v} \Delta t \quad (62)$$

where

T_0 is the temperature at t_0 .

The problem with this method is that a constant rate of change \dot{T} , and therefore a constant heat transfer rate and heat generation rate \dot{Q} and \dot{Q}_v , is assumed for the entire timestep Δt . This is of course not accurate since \dot{Q} and \dot{Q}_v are dependent on T and t . Using this method therefore induces errors in situations where there is a non-constant rate of change as illustrated in Figure 56.

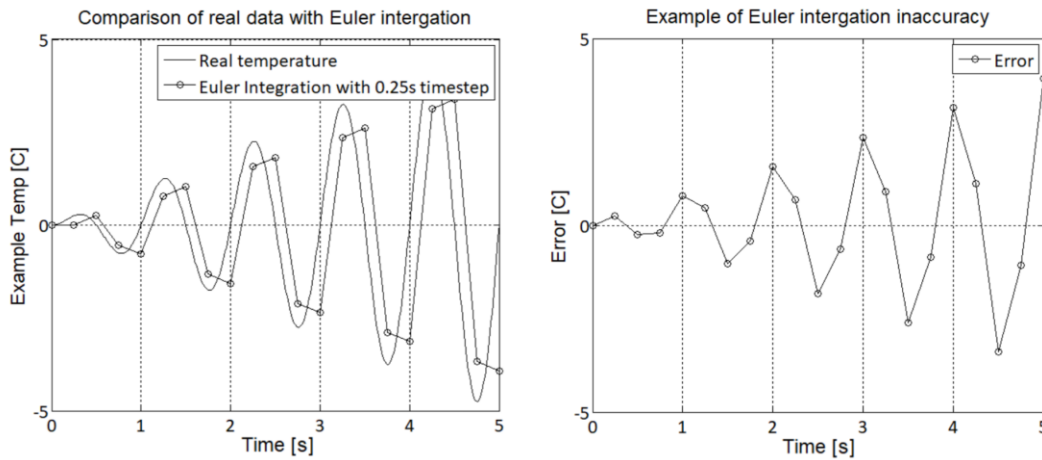


Figure 56: Errors induced by Euler integration for large timesteps

The global error with this first order method is proportional to the step size and can be greatly reduced by making steps smaller. This is illustrated in Figure 57 where the step size is reduced from 0.25 s to 0.05 s and the error is similarly reduce by a factor 5.

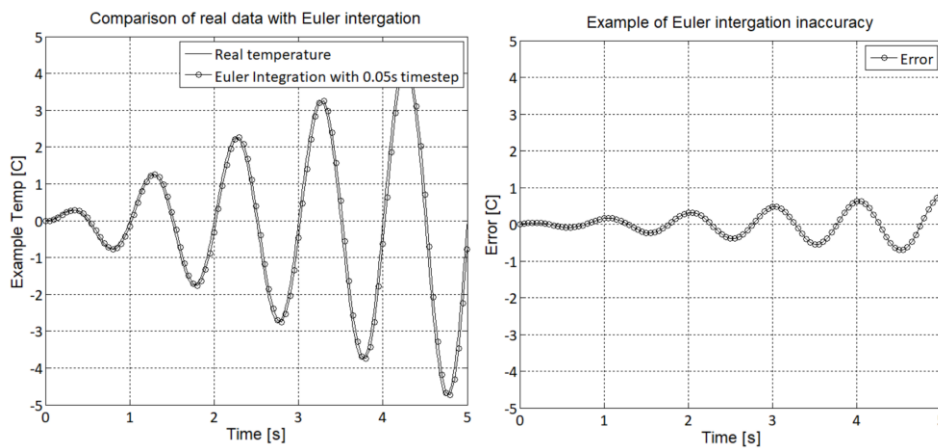


Figure 57: Errors induced by Euler integration for smaller timesteps

Since the heat transfer rates of the satellite depends on the attitude of the satellite, the thermal simulation must run at the same update rate as the attitude simulation of the satellite. The attitude simulation includes complex high order calculations for orbital

models, environmental models, aerodynamic drag and propagation of the kinematics of the satellite among others. These calculations require complex mathematical computations that places a huge burden on the CPU of the PC which is running the simulation. For this reason, reducing the timestep size comes at a tradeoff of slower simulation, which in turn makes the simulation less useful for the average user.

To address this problem the Runge-Kutta fourth order method is considered, which is the most widely used Runge-Kutta method. The Euler method assumed a constant gradient for the entire timestep based on the gradient at time t . The fourth order method considers not only the instantaneous gradient at time t , but rather calculates gradients later within the timestep based on predicted values of T , and finds a weighted average gradient that provides a better estimate of the temperature after the timestep. Applying this method, we estimate the temperature

$$T(t_0 + \Delta t) = T_0 + \frac{1}{6}(k_1 + 2k_2 + 2k_3 + k_4) \quad (63)$$

Where

$$\begin{aligned} k_1 &= \Delta t [\dot{Q}(t_0, T_0) + \dot{Q}_v(t_0, T_0)], \\ k_2 &= \Delta t [\dot{Q}(t_0 + \Delta t/2, T_0 + k_1/2) + \dot{Q}_v(t_0 + \Delta t/2, T_0 + k_1/2)], \\ k_3 &= \Delta t [\dot{Q}(t_0 + \Delta t/2, T_0 + k_2/2) + \dot{Q}_v(t_0 + \Delta t/2, T_0 + k_2/2)], \text{ and} \\ k_4 &= \Delta t [\dot{Q}(t_0 + \Delta t, T_0 + k_3) + \dot{Q}_v(t_0 + \Delta t, T_0 + k_3)]. \end{aligned}$$

Applying this method to the same dataset used to generate Figure 56 and Figure 57, Figure 58 is generated using a 0.25s timestep. From this figure the error for the Runge-Kutta method is in the order of 500 times smaller for the same timestep size.

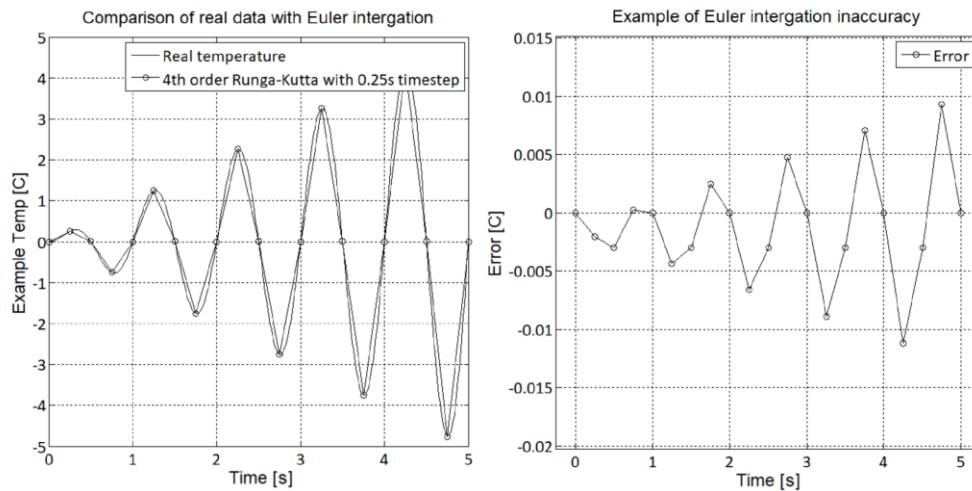


Figure 58: Errors induced by 4th order Runge-Kutta

Even though the fourth order Runge-Kutta performs better, it still requires a sufficiently small step size to be stable. According to [41], for

$$\dot{y} = f(t, y) \quad (64)$$

the region of stability for the Runge-Kutta method is

$$-2.78 < h \frac{\partial f}{\partial y} < 0 \quad (65)$$

With h the timestep in t .

For numerical solutions $\frac{\partial f}{\partial y}$ can be approximated using the discrete instantaneous difference

$$\frac{\partial f}{\partial y} \approx \frac{f_n - f_{n-1}}{y_n - y_{n-1}} \quad (66)$$

Applying this test to the worst-case gradient as simulated in Section 6 with a step size of 1 second, the above inequality is satisfied.

6 Simulation Results and In-Orbit Measurements

The simulations in this section were done with the complete nSight-1 thermal model. Two sets of data were pulled from the nSight-1 data archive for periods where the satellite was firstly in a Y-Thomson spin, and secondly in a 3-Axis stable Nadir pointing orientation. An orbit was chosen for the simulation based on the TLEs that were available from NORAD for the period when the data was collected.

6.1 Description of Scenario

Two different common satellite attitude scenarios were investigated, a Y-Spin mode and 3-Axis stable Nadir pointing mode. Typically, when a satellite is ejected out of the pod in which it is launched, it has an initial random spin called the tip-off rate. Typically, the first major step of the ADCS commissioning process is detumbling the satellite into a predictable stable spin, called a Y-Thomson spin. This spin has the following characteristics:

- 1) It ‘dumps’ the rates in the satellite X and Z axes to as close to zero as possible,
- 2) It aligns the satellite Y-Body axis with the orbital Y-Axis, and
- 3) It controls the satellite Y-Body spin to a target rate.

This ADCS state has the following advantages:

- 1) The control mode can be achieved by using only the magnetic torquers as actuators,
- 2) Once in a Y-Spin, very low torquer activity is required to maintain the spin,
- 3) Provides guaranteed sunlight on the solar panels,
- 4) The transition from Y-Spin to 3-Axis stabilized can be achieved with a single action of absorbing the spin of the satellite into the Y-Wheel, and
- 5) Temperature is more evenly distributed throughout the satellite.

The Y-Spin control modes is usually the first step in the detumbling process, but also provides a great fall back ‘safe mode’ where low power is required for ADCS, and solar panel illumination is guaranteed.

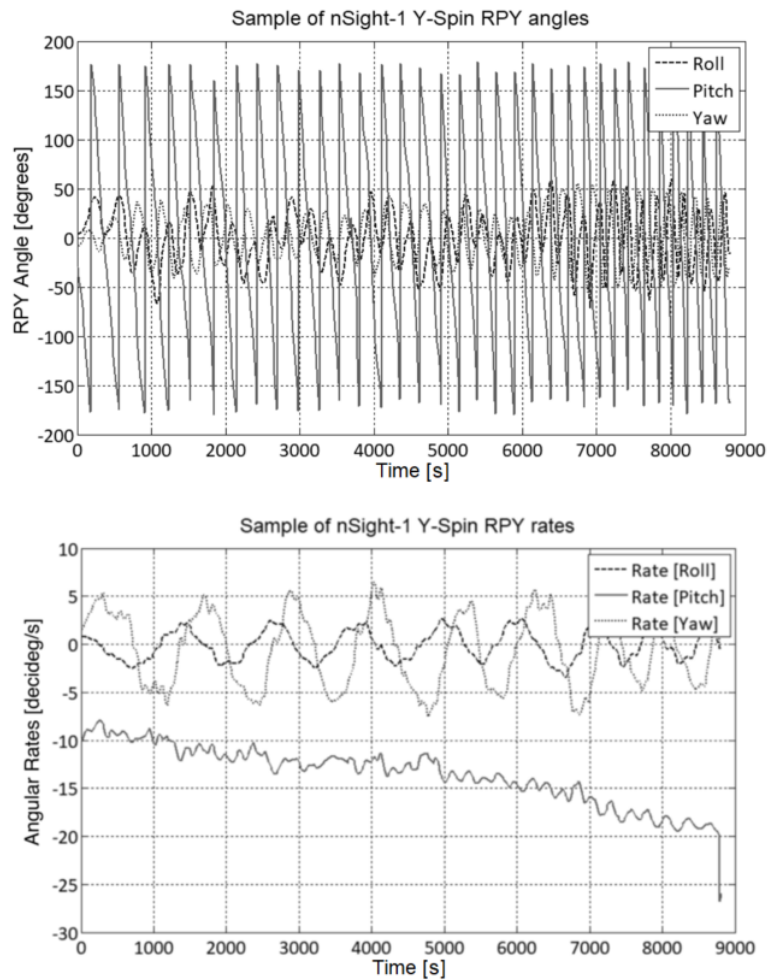


Figure 59: Y-Thomson spin RPY (top) and body rates (bottom)

Figure 59 shows a piece of in-flight data for nSight-1, recorded on 24 February 2018. It shows the estimated RPY angles as well as the body rates of the satellite for a period where it was in a Y-Spin control mode. From Figure 59 (top), the pitch angle takes the form of a saw-tooth, while the roll and yaw oscillate around zero. This indicates that the satellite is in a stable Y-Spin with the pitch angle increasing roughly linear from -180° to 180° , where it rolls over back to -180° . This can be better illustrated in the zoomed in section shown in Figure 60.

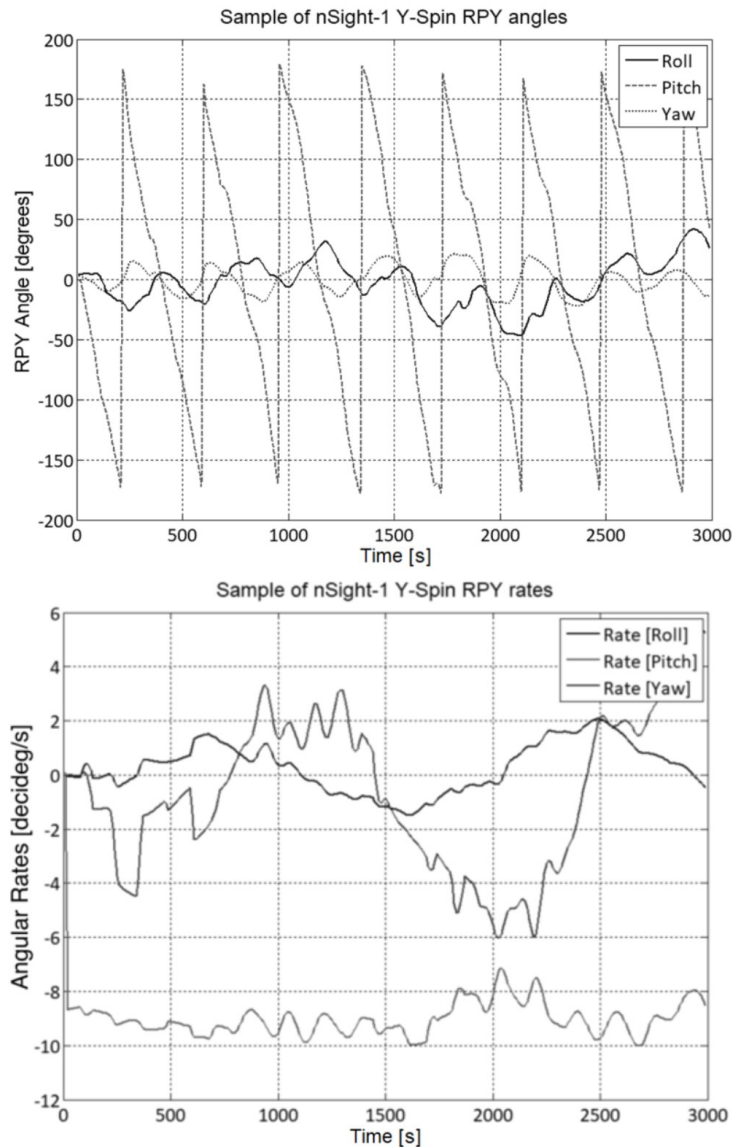


Figure 60: Zoomed Y-Thomson spin RPY (top) and body rates (bottom)

Typically, most satellite payloads require the satellite to be 3-Axis stable. Once stable, depending on the ADCS architecture, the satellite can then point the payload in the desired direction for it to operate. The architecture of the ADCS onboard nSight-1 has only one momentum wheel in Y_{SBC} . The satellite's Y-Spin is absorbed into this momentum wheel, and thereafter the magnetorquers are used to maintain a Nadir pointing attitude, while also maintaining the wheel speed to a constant offset. This offset in speed on the momentum wheel provides the satellite with a constant angular momentum in the $-Y_{ORC}$. If a satellite is not momentum biased in this manner, external disturbance torques resulting from aerodynamic drag forces, as well as magnetic disturbances, make the satellite hard to control. Furthermore, the fact that magnetic control torque can only be exerted orthogonal

to the Earth's magnetic field, limits the satellite's ability to counter such disturbances using only torquer rods.

Figure 61 shows the satellite RPY angles as well as body rates oscillating around zero, indicating a Nadir pointing satellite.

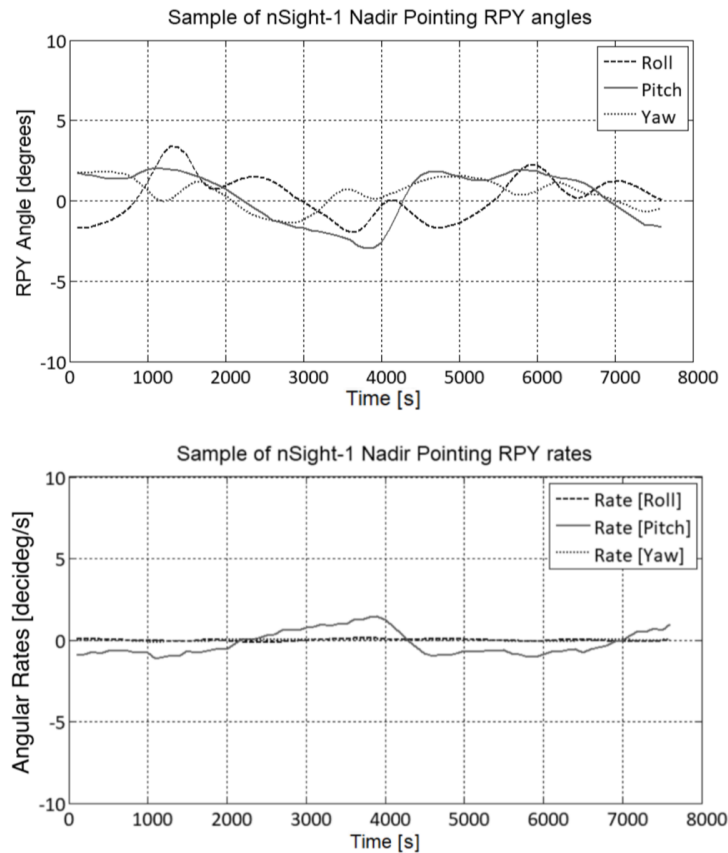


Figure 61: Nadir pointing RPY (top) and body rates (bottom)

Both the Y-Momentum and 3-Axis datasets are for a total time of roughly 130 min. The orbital period for this altitude orbit is roughly 90 min, so it is expected that a dataset of 130mins would contain at least a full section of both the sunlit and eclipse part of the orbit. Figure 63 shows the current supplied by the three solar panel boost converters for both the Y-Spin, as well as the Nadir pointing modes. From the figures it is clear that during the middle part of the dataset, the satellite was in eclipse, and had no sun on the solar panels. The Nadir pointing case has a cycling nature corresponding to the satellite making a single inertial rotation as it moves through the orbit in a Nadir pointing orientation. The Y-Spin case follows the same pattern but has an additional higher frequency cycle due to the rotation of the satellite around its Y-Body axis as shown in Figure 62.

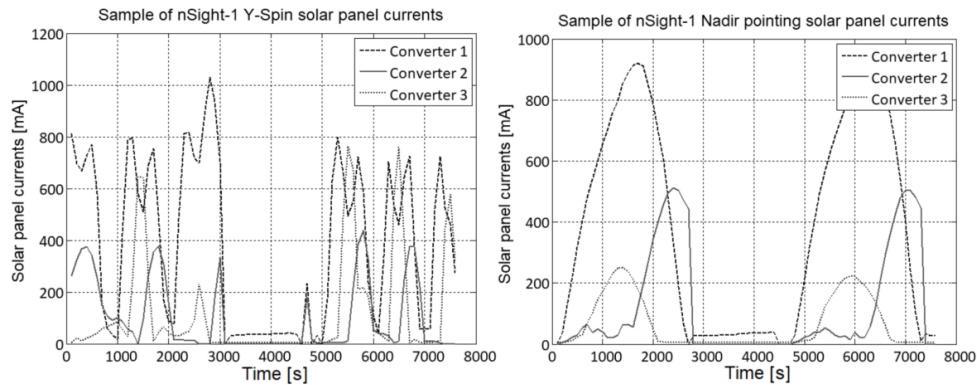


Figure 62: Generated solar panel power for Y-Spin (left) and Nadir pointing (right)

Adding the currents of all three converters together for each case, the total solar panel current was calculated and is shown in Figure 63. This figure also shows the average solar panel current, which is roughly equal for Nadir pointing and Y-Spin modes. A simple explanation for the fact that the two cases produce roughly equal amounts of power is that both the orbital motion, and the rotational motions are cyclical, with similar maximum and minimum values. The average value of the superposition of the two cyclical motions, is equal to the sum of the average values of each cyclic motion. This would have not been the case if the satellite had solar panels facing the Z+ Body axis. If the satellite had panels in both Z+ and Z- Body axes, the satellite would have received sun on solar panels in the sunlit part of the orbit, regardless of the orientation. Even if it had Z+ panels, it would however still not receive any power while in eclipse, and we would expect a spinning satellite to generate more power.

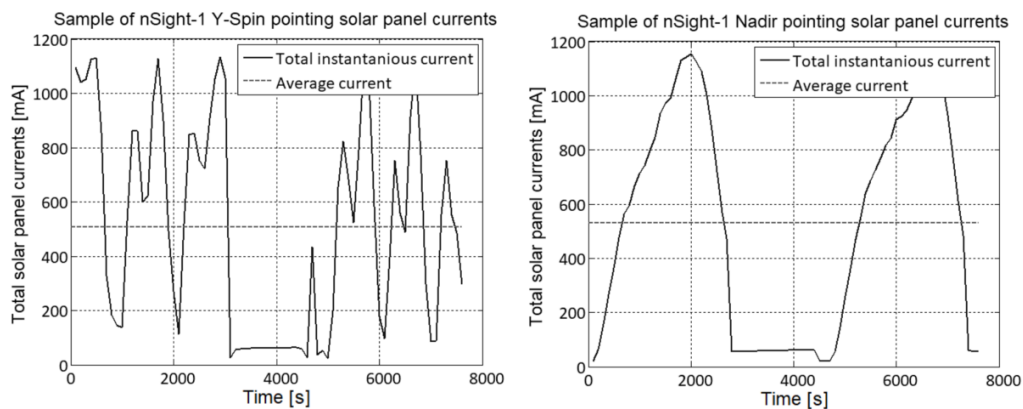


Figure 63: Solar panel currents for Y-Spin (left) and Nadir pointing (right)

6.2 Comparison of Flight and Simulated Data

6.2.1 Battery

As discussed in Section 4.6, the satellite consumes different amounts of power depending on the control modes. This is because the reaction wheels and sun sensors are running while doing 3-Axis pointing but not when doing Y-Spin. Figure 64 shows the battery currents for both control modes. From this figure, it can be seen that the satellite draws large peaks of current periodically. These peaks are due to the large current drawn when transmitting beacons.

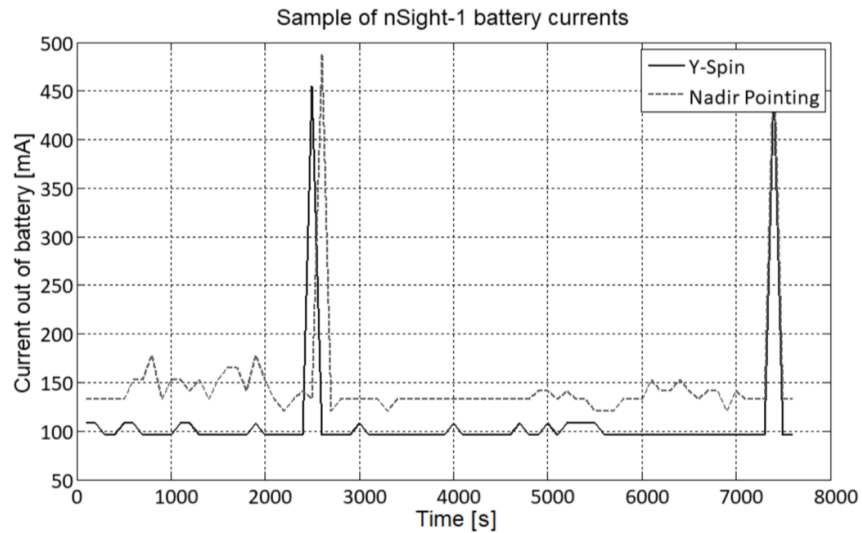


Figure 64: Current delivered from battery for Y-Spin and Nadir pointing

The assumptions made in Table 9 in Section 4.6 regarding the power consumption of the satellite for Mode 1 (Y-Spin) and Mode 2 (Nadir pointing) is verified to be correct by comparing the results with the in-flight measurements shown in Figure 64.

Figure 65 shows the battery voltage for both the Y-Spin as well as the Nadir pointing case. This figure illustrates that even though the same power is generated in both cases, the battery is drained deeper while the satellite is 3-Axis stable because more of the ADCS subsystems are switched on and as a result, the satellite consumes more power.

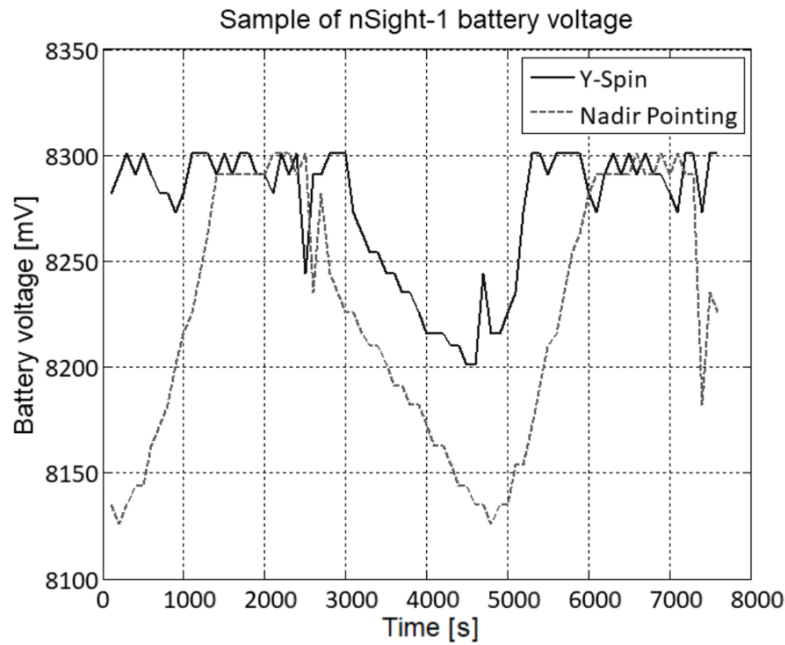


Figure 65: Battery voltage

Since the satellite is consuming more power, the average temperature of the satellite is expected to be higher, and the battery itself will experience further increases in heat generation because of losses due to battery internal resistance. This is confirmed in Figure 66 which shows both a higher average battery temperature, as well as larger variation from minimum to maximum.

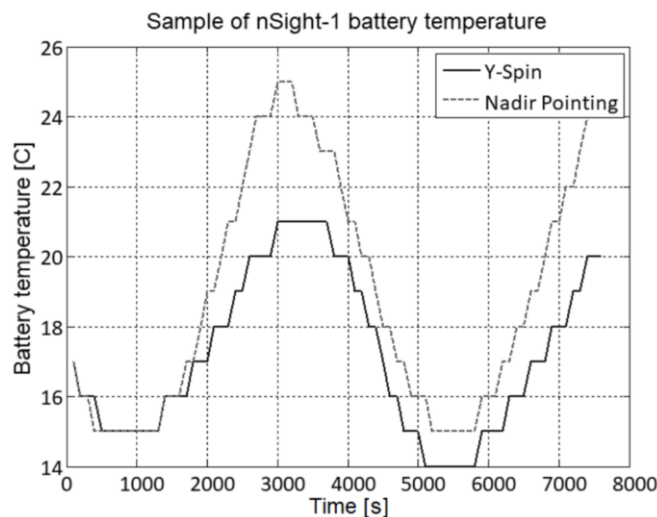


Figure 66: Battery temperature measurements

The simulated battery temperatures (Figure 67) followed a similar trend, but had two main differences:

1. The overall temperatures for both the Y-Spin as well as the Nadir pointing case were higher, and
2. The difference in temperatures between the Y-Spin and Nadir pointing cases were larger.

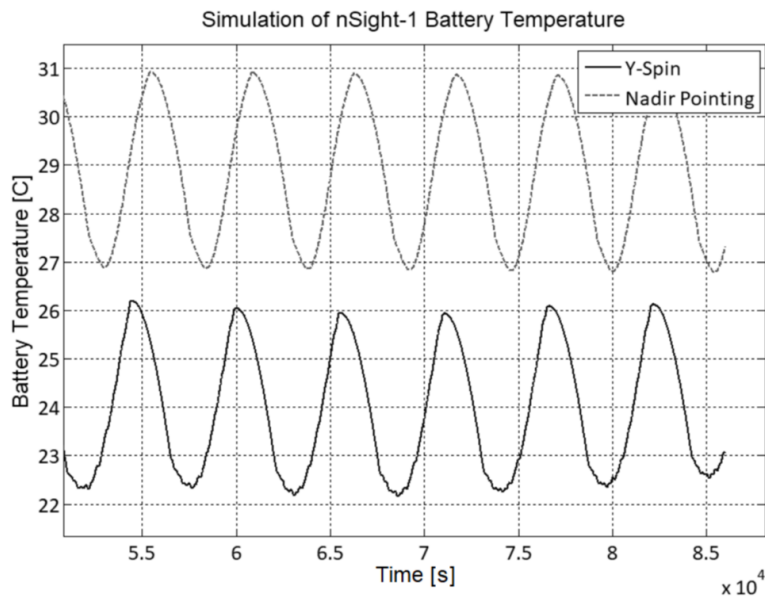


Figure 67: Simulated Battery temperatures

Upon further investigation, the reason for the difference was identified as being a result of the heat generated by the charging of the batteries by the solar panels. When the battery is not full, the energy incident on the solar panels is converted to electrical energy, which charges the battery, and generates heat on both the PV regulators on the EPS and heats up the battery itself. However, when the battery is above a certain threshold, the battery draws no load from the panels, and they stop generating electrical current. In this case the incoming solar energy goes towards heating the solar panels themselves.

As discussed in Section 4.6, the thermal model assumes that heat is generated in the PV converters and battery, in relation with the amount of current drawn by the satellite bus, which is only dependent on which subsystems are switched on. However, if we consider Figure 65, we find that the battery fully recharges within a small fraction of the sunlit part of the orbit, and that the assumption that heat will be generated in the EPS because of solar charging throughout the orbit is incorrect.

The simulation has no way of determining whether the battery is full or not, since battery levels are not currently simulated. If the heat generation is manually limited in the

simulation to only a 5th of the sunlit part of the orbit, battery temperatures were simulated and is shown in Figure 68.

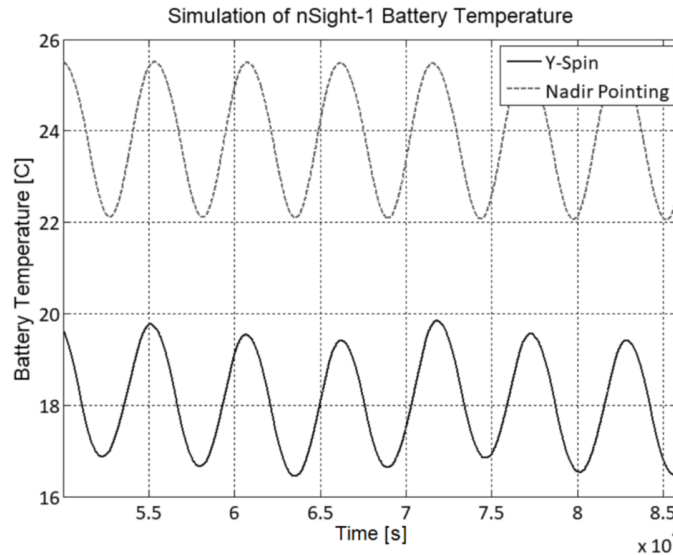


Figure 68: Simulated Battery temperatures with limited solar charge heat generation

This correlates better with the measured data. A summary of the measured and simulated temperatures is shown in Table 28.

Table 28: Comparison of simulation with and without heat generated due to charging

	Minimum Temperature [°C]			Maximum Temperature [°C]		
	Actual	Simulated With charge	Simulated Limited charge	Actual	Simulated With charge	Simulated Limited charge
Y-Spin	14	22	17	21	26	20
Nadir Pointing	15	27	22	25	31	26

6.2.2 Computer/MCU

The measured temperatures vary in cycling nature due to the eclipse period, but also contains some higher frequency variations as shown in Figure 69. One might think that these variations are linked to the rotation of the satellite as it does a Y-Spin. However, it does not correlate with this. The noise on the measurement is due to the fact that the measurement contains high frequency noise, and that the exact time the measurement is sampled in the MCU varies. This was confirmed with the supplier, and this noise is present even on ground tests. Figure 70 and Figure 71 show the simulated MCU temperature with and without solar charge and shows close correlation with the measured data.

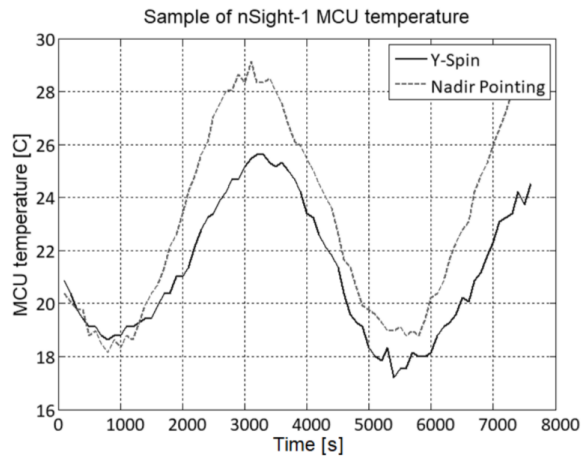


Figure 69: OBC MCU temperature for Y-Spin and Nadir pointing

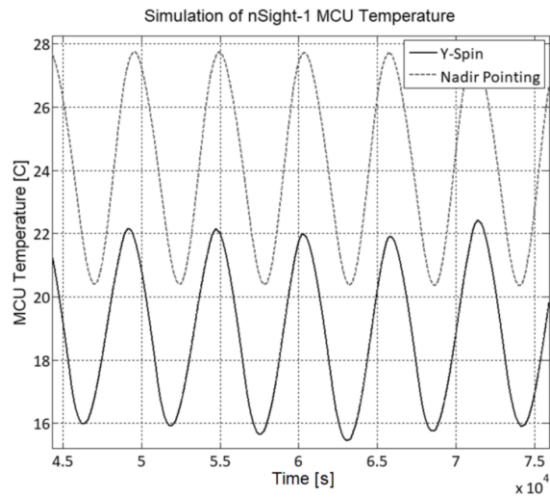


Figure 70: Simulated OBC MCU temperature

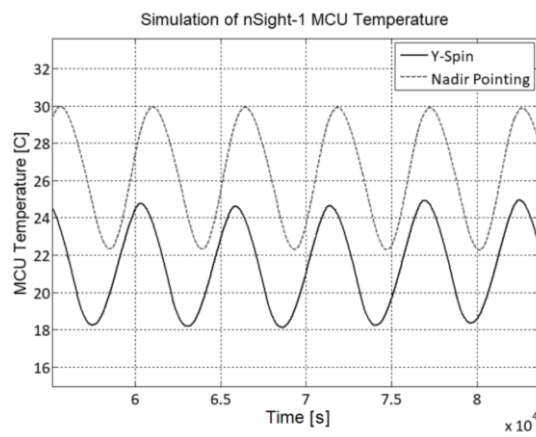


Figure 71: Simulated OBC MCU temperature with solar charge

6.2.3 Deployable Magnetometer

The measured temperatures for the deployable magnetometer are shown in Figure 72. The magnetometer is mounted on the outside of the satellite and is not thermally connected to the satellite very well. Due to its small thermal mass, direct exposure to the space environment, and bad thermal connection to the satellite body, it undergoes large temperature variations between the sunlit and eclipse part of the orbit. Furthermore, due to the fact that it is shielded by the satellite body as the satellite rotates in a Y-Spin, the magnetometer experiences higher frequency temperature variations than the normal cyclical variation between sun and eclipse. Figure 73 shows the simulated data of the satellite spinning at a slightly higher rate. The real and simulated temperatures correlate well, and the simulation demonstrates the effect of the rate on the higher frequency temperature variation.

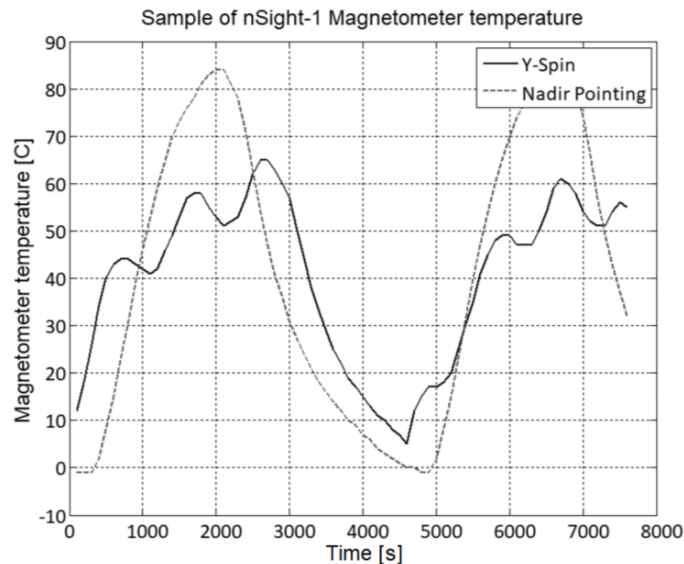


Figure 72: Deployed magnetometer temperature

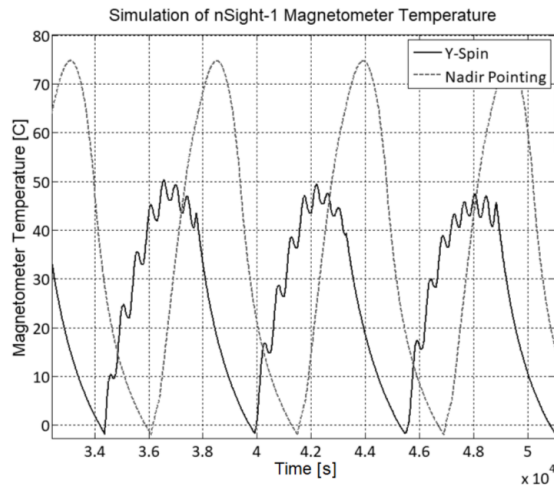


Figure 73: Simulated deployed magnetometer temperature

6.3 Satellite Subsystem Temperature Ranges

Each of the parts/subsystems of the satellite have minimum and maximum operation temperatures within which they can operate. Certain parts like the structure, and solar panels are designed to withstand extreme temperatures, whereas parts like the battery and payload usually have more strict limits on their operational temperatures. Ideally the temperature of all subsystems should be contained to within their operational range with some safety margin.

The operational temperature ranges for all operational subsystems on the nSight-1 mission are shown in Table 29. This information was taken from their datasheets.

Table 29: Operational temperature ranges for each subsystem

Subsystem	Min [°C]	Max [°C]
Structure	N/A	N/A
Solar panels	-40	85
CubeComputer	-10	60
Magnetometer	-20	80
EPS	0	45
CubeControl	-10	60
CubeSense	-10	60
VHF/UHF Radio	-25	60

It is difficult to visualise the temperature of all the subsystems at once by comparing graphs for their individual temperatures, plotted against time. To simplify this, a graphing system was introduced which plots the simulated temperature ranges, from minimum to maximum, for each component as a vertical line. Furthermore, nodes that form part of the same section are grouped together (e.g. the 6 nodes on the Z+ Body panel). The simulated temperature

ranges for the subsystems, as well as their rated operational temperature limits are shown in Figure 74.

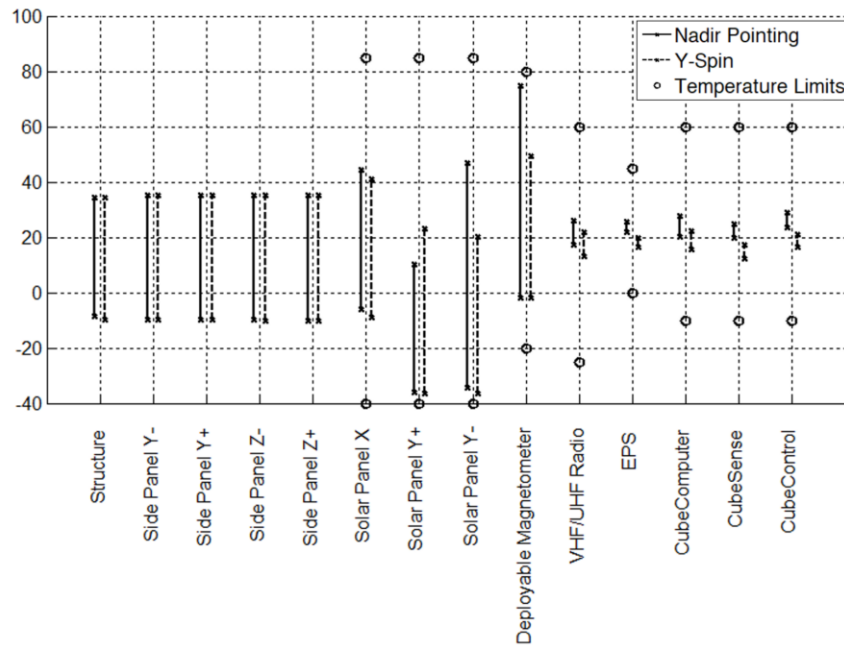


Figure 74: Temperature ranges of subsystems

From the figure, all subsystems are within their allowable margins. The two subsystems that come close to their operational limits are the deployable solar panels, and the deployable magnetometer. These two components are expected to reach extreme temperatures due to their bad thermal connection to the satellite.

There is a risk that these components will exceed their operational limits if the satellite's orbit precesses. The temperature of the satellite is simulated for a variety of orbits in Section 6.4 to investigate whether the subsystems stay within the operation limits, to identify risks, and to determine whether these risks can be mitigated by placing the satellite in specific operational modes.

6.4 Orbit Dependence of Satellite Temperatures

One of the shortcomings of traditional thermal analyses on CubeSats, as discussed in Section 2, is a lack of consideration for the decay and precession of the orbit. As the orbit changes, and the corresponding angle between the Sun and the orbit changes, eclipse times change, and the direct solar radiation affects the satellite from a different angle. These have effects on both the average temperature of the satellite, as well as the minimum and maximum temperatures the satellite reaches.

To study this effect on nSight-1, the satellite was simulated in a Nadir pointing mode, for orbits of varying β -angles. Orbits with Right Ascension of the Ascending Node (RAAN), ranging from 0° to 90° , were simulated with steps of 5° . The minimum and maximum temperatures of sensitive subsystems are plotted against RAAN angle in Figure 75 to Figure 78.

Figure 75 shows how the EPS temperature increases for increased RAAN. For zero RAAN, the satellite has maximum eclipse length, and one expects the coldest temperatures. As shown in Table 29, the operational temperature range of the EPS is 0°C to 45°C . At this point the EPS is still well above the minimum limit and does not pose any risks. As the RAAN increases, the satellite has shorter eclipse times, and the average temperature of the satellite rises. The EPS starts exceeding the maximum temperature at roughly 70° RAAN. At 80° RAAN the EPS is outside of its maximum bounds by 15°C and will have high likelihood of failing. This simulation highlights exactly why a thermal analysis cannot be done for only a single orbit when a satellite is launched in a non-Sun-synchronous orbit in LEO.

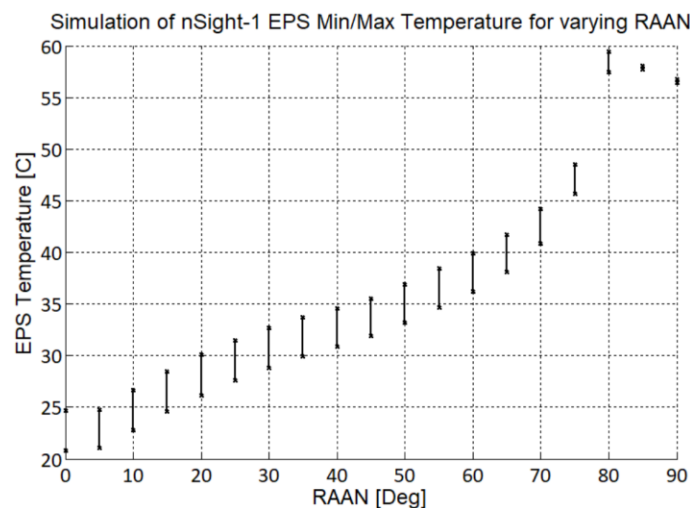


Figure 75: Temperature range of EPS for various β -angles

As shown in Figure 76, the magnetometer stays within its operational temperature limits, but only within $<10^{\circ}\text{C}$ from the maximum limit. This simulation was with the magnetometer in a semi-stowed state. However, if the magnetometer were to be deployed, the temperature variation will be much more extreme due to a smaller thermal coupling to the heavy satellite body and will most likely exceed operational temperature limits. Another concern is the fact that the magnetometer electronics are varying about 70°C every orbit, which poses the risk for solder joints to degrade. As the electronics heat up and cool down, solder joints expand and contract, which may lead to degradation of these joints. The recommendation would be for the magnetometer to be better insulated so that it is less thermally connected to the warm sunlit part, and cold eclipse part of the orbit.

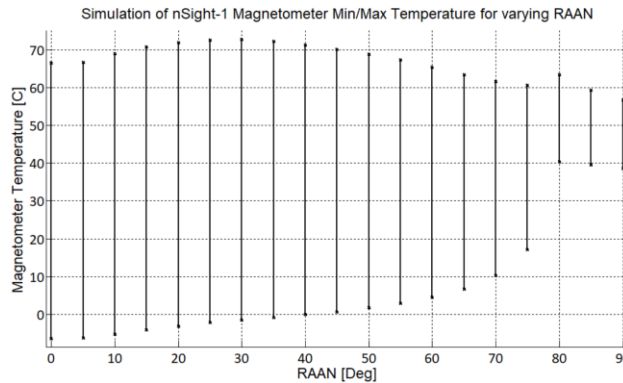


Figure 76: Temperature range of deployable magnetometer for various β -angles

Figure 77 and Figure 78 shows the Y+ and Y- deployable solar panels. As can be seen from these figures, the two solar panels experience significant variances in temperatures. The reason for this is that as the RAAN increases, and the Sun moves further out of the orbital plane, only one side of the satellite is directly exposed to the Sun. The temperatures of the panels stay within operational limits, but the temperature is within 5°C of the lower limit in the maximum eclipse case, which is concerning.

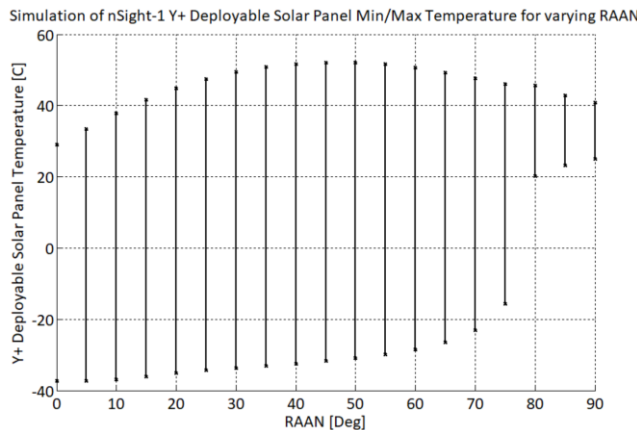


Figure 77: Temperature range of Y+ deployable solar panels for various β -angles

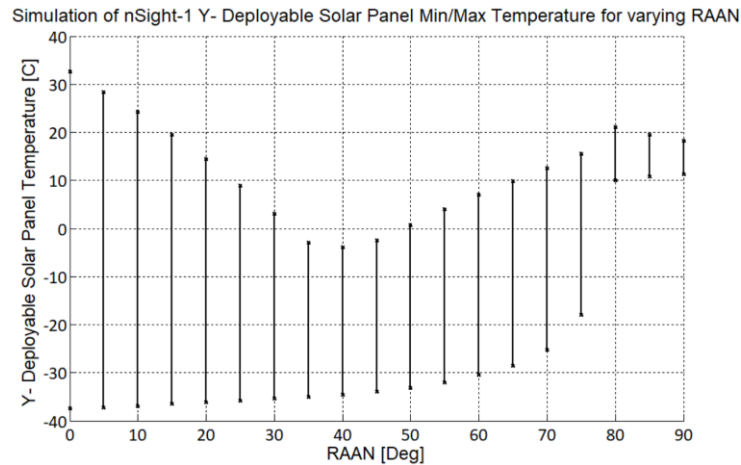


Figure 78: Temperature range of Y- deployable solar panels for various β -angles

6.5 Necessity of Thermal Contact Resistances

The thermal model was created by considering the individual parts of the satellite assembly and dividing them into smaller control volumes. The various parts were then connected to each other in the thermal model by means of contact resistances. At the time of creating the thermal model, it was not known whether thermal contact resistances would play a significant role in the analysis. The thermal contact resistances were added for the sake of completeness and provided the flexibility to later determine whether it is required or not.

As described in Section 5.2.6, it was found that thermal contact resistances play an insignificant role in the temperature of the satellite. This is largely due to the following factors:

1. Aluminium is used, which typically has low contact resistance since it is a relatively soft metal,
2. The other thermal conductive paths in the satellite have large thermal resistances relative to the contact thermal resistances, making them less significant, and
3. The parts of the satellite where there are contact resistances, are typically fastened with bolts which provides a high contact pressure, and conducts heat itself through the threaded connection.

During simulation it was found that the peak heat flux through one of these contact resistances was about 2 W, resulting in a temperature drop of 1°C over the contact resistance. This 1°C temperature drop over an already, overly conservative estimate on the thermal contact resistance, is deemed negligible.

A different approach for defining the thermal control volumes/thermal nodes of the satellite is suggested, where the satellite as a whole is considered, instead of the individual parts from which the satellite is assembled as illustrated in Figure 79.

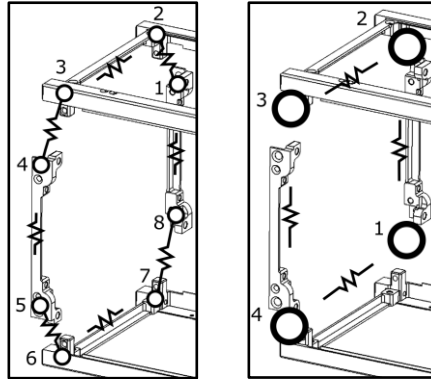


Figure 79: Thermal model with thermal contact resistances (left) and without (right)

This approach would result in

- lower total number of thermal nodes in the satellite model, lowering computational load,
- lower number of thermal resistances, lowering computational load, and
- less small thermal resistances, which causes ill-conditioned matrices and inaccurate numerical integration.

6.6 Isolation of Electronics from Outside Panels

The outer surfaces of the satellite reach extreme temperatures as the satellite moves between eclipse and the sunlit part of the orbit. How well these panels are thermally connected to the internal electronics of the satellite, significantly influences the equilibrium temperature of the electronics as well as the temperature variation of the electronics. There are two locations that significantly influence this connection:

1. The connection between the side/solar panels and the structure, and
2. The connection between the electronic PCBs and the structure.

In satellites with body fixed panels, there is not much that can be done to influence the thermal connection between the structure and the side/solar panels. If required in extreme cases, some insulation material can be placed between the panels and the structure, however this is uncommon in typical CubeSats. For deployable solar panels, the thermal connection to the structure through the mechanical deployment mechanism can vary significantly depending on the design. In this case, panels can be better isolated from the electronics.

The efficiency of the solar cells is very temperature dependent and drops sharply for increased temperatures. The more isolated the solar panels are from the large thermal mass of the satellite, the larger the variation in the temperature of the solar panels will be. Isolating the panels might therefore benefit the electronics of the satellite but may decrease power efficiency.

As mentioned above, the connection of the electronic PCBs to the satellite structure also significantly influence the temperature variance of the electronics, since the structure typically varies 5-10 times more than the electronic PCBs. Typical CubeSat PCBs are stacked on stainless steel rods, as described in Section 5.2. These rods provide a relatively low thermal conductivity to the structure. However, PCBs are usually stacked with some spacers between them to keep them apart. The spacers used varies between Stainless Steel, Aluminium and plastics for different satellites. For these various materials, and a 6mm OD 3 mm ID space, the approximate thermal resistances between a typical PCB located in the middle of a 1U stack (e.g node 77), and the structure is shown in Table 30.

Table 30: Total resistance between PCB and structure for varying space material

	Delrin	S/S	Aluminium
Total parallel resistance between PCB and structure through rails	52.2 K/W	27.5 K/W	19.3 K/W

Simulating the temperature for the same orbit and in a Nadir pointing attitude, with the varying spacer materials as discussed above, the MCU temperatures are shown in Figure 80.

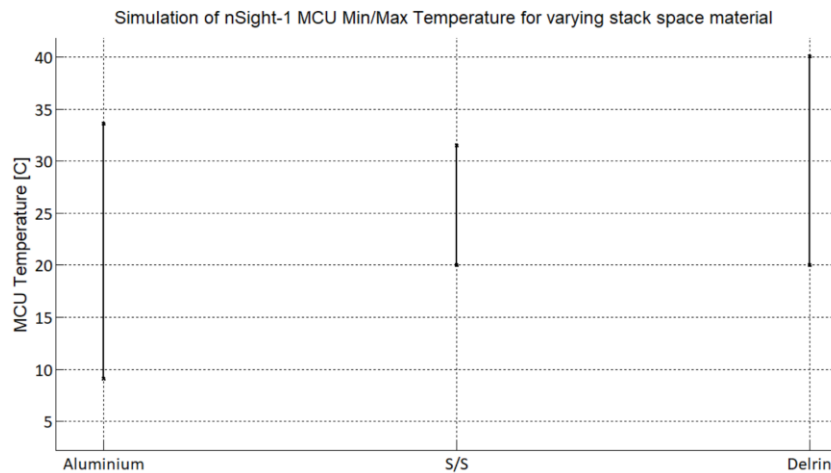


Figure 80: Change in MCU temperature for varying PCB spacer material

In none of the papers regarding CubeSat thermal design was any attention paid to the effect of PCB spacers on the thermal performance of the electronics. However, these spacers do

play a very important role in the electronics passive thermal control and should thus be carefully considered.

The concept of insulating the internal electronics from the satellite structure, and the concept of using the thermal mass of the satellite structure to reduce total extreme temperature variation of the outer structural elements is discussed in [42], and many of the design principles in this study should be applied to CubeSats in general.

6.7 Better Connections between Deployables and Satellite Body

As expected, deployable parts of the satellite reached more extreme temperatures. Usually these subsystems are designed for wider operational ranges, but as found in this study, there are risks to having sensitive electronics in a deployable mechanism.

One way of lowering the temperature ranges experienced by such deployables is through applying Multi-layer Insulation (MLI) blankets to the device. These blankets consist of multiple thin layers of material, separated by a small distance and void of any solid or fluid in the gaps between them, creating a chain of series connected radiative thermal resistances.

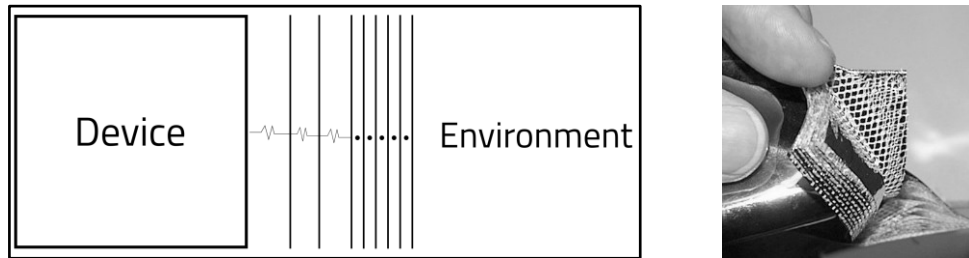


Figure 81: Illustration of MLI (left). Example implementation of MLI (right)

While it is not practically possible to create such layers that are not in contact with each other. A way of achieving something very close to this is by separating thin metallic sheets of foil, with a thin polyester mesh with low conductance, as shown in Figure 81.

Generally, the heat transfer rate through this kind of blanket decreases linearly with the number of layers in the blanket. Considering that these blankets consists of very thin layers, it is possible to build a highly insulating layer within a relatively thin blanket. If a commercially available blanket [43] were to be used to cover the magnetometer head, the exposure to the high temperature of the Sun and the low temperature of deep space would be minimised, and the extreme temperatures of the magnetometer electronics would be reduced. In such a case the outer surface that is exposed to the space environment is separated from the magnetometer electronics through a large thermal resistance. In the case of the above-mentioned commercial blanket, the layer has thermal conductivity of $0.00013 \text{ W/m} \cdot \text{K}$.

To simulate the effect that such a blanket would have on the temperature of the magnetometer, we assume perfect insulation of the magnetometer head. Therefore, there is

no energy transfer between the outer surfaces of the head and the environment, and the only heat transfer from the magnetometer head is through the conductive deployment boom. Simulating this is achieved by setting the outer surfaces of the magnetometer head to have zero emissivity and absorptivity and the results are shown in Figure 82.

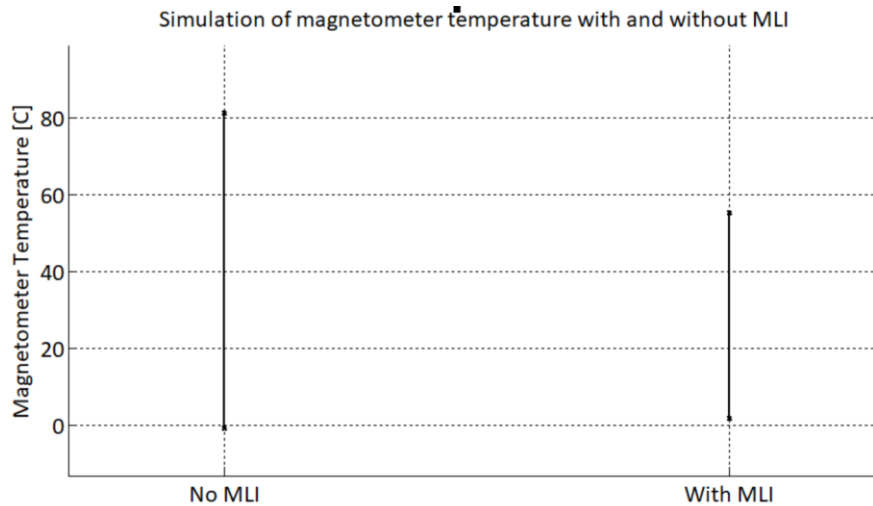


Figure 82: Magnetometer temperature variation with and without MLI blanket

The deployable solar panels generally have very wide variation and reaches close to its minimum operational temperatures. Since the temperatures are within some margin of the maximum operational temperatures, one solution to the problem at minimum temperatures would be to lift the overall temperature of the panels. This can be done by having a lower emissivity coating on the back of the panels, which will reduce the ability of the panels to radiate away its own heat. The problem with this approach is that it will increase the satellite temperature even further, and thus further exaggerate the already high EPS temperatures. A better way to solve this problem would thus be to improve the connection between the panels and the satellite body, as this would decrease the variation between maximum and minimum temperatures.

7 Discussion, Conclusions and Recommendations

A simple to use tool was created to enable a user to enter a surface model of a satellite, with deployables, into a computer with ease. The tool provides the user the ability to assign thermal properties to the surfaces, as well as to link the surfaces to nodes in a lumped-capacitance thermal model. Furthermore, the ability to simulate dynamic orientation thermal models in a space environment was created. For each satellite that is to be simulated in this environment, a lumped-capacitance model has to be created by considering conductive connections within the satellite. When creating such a simulation for a given satellite, the largest task would be to create this model.

The simulation of the temperatures of nSight-1 shows good correlation to in-flight data. For subsystems with more stable temperatures on the inside of the satellite, simulated temperatures are within 10% of measured temperatures. For outside panels and deployable structures temperatures reach much more extreme values, and the simulated temperatures are within 30% of real values (may need Y-Spin simulation with slower rate).

One of the major limitations of the simulation is that it is not able to determine what the battery level of the satellite is. The sunlight that is absorbed by the solar panels is either turned into electrical energy, or turned into heat on the panel, depending on the load connected to the solar panels. If the battery is fully charged, the panels stop delivering energy to the battery, and the solar energy heats the panels. When the batteries are not full, the solar panels provide a charging current to the batteries, which in turn heats up the batteries. These two cases have a significantly different effect on the total temperature and temperature distribution of the satellite. To be able to accurately simulate this effect, the charging characteristics of the battery would need to be modelled and the total energy consumed by the satellite would need to be accurately tracked. This would be a valuable feature that will have a significant effect on the accuracy of the simulation and is a recommended future addition.

The scripting feature in EOS, combined with the thermal simulation plugin, creates a powerful tool capable of doing complex thermal analyses for varying orbits and generating data that can be used to draw practical conclusions about a satellite's thermal design. These analyses are very useful for choosing satellite surface finishes to ensure that a satellite in LEO (which typically have rapidly varying orbits) has passive thermal performance that keeps all subsystems within their temperature limits.

The lumped-capacitance thermal model of the satellite was created with conductive thermal connections in mind. Heat-flow between nodes is calculated using a Runge-Kutta integration of heat transfer rates, which is calculated using a matrix of thermal resistances between nodes. As shown in Section 5.2 the radiative connection between PCBs, and between solar panels and the satellite body for example, can be significant and should be included in the simulation, These radiative heat transfers had to be manually handled in the

simulation software, and could not be easily input into the program in the same way the conductive connections could. This is a definite area for improvement for future versions of this software.

The simulation was only verified with one set of data, from one satellite, due to the lack of availability of more flight data. The only way of further improving accuracy and testing the simulation for edge cases would be to use flight data from other satellites and to compare results.

Ultimately the simulation tool could provide information of sufficient accuracy, for varying orbits, with varying load, for varying satellite attitude, so that the thermal design of a satellite could be analysed, and useful lessons could be learned about the design. Based on these results, it can be concluded that all goals for this study were achieved successfully.

References

- [1] H. Heidt, J. Puig-Suari, A. S. Moore, S. Nakasuka, and R. J. Twiggs, "CubeSat: A new Generation of Picosatellite for Education and Industry Low-Cost Space Experimentation," in *AIAA/USU Conference on Small Satellites*, 2000, pp. 1–19.
- [2] CalPoly, "Cubesat design specification," 2005, Online: http://www.cubesat.org/images/developers/cds_rev12.pdf%5Cnh..
- [3] S. L. University, "CubeSat Database." [Online]. Available: <https://sites.google.com/a/slu.edu/swartwout/home/cubesat-database/>.
- [4] C. Nieto-Peroy and M. R. Emami, "CubeSat Mission: From Design to Operation," *Appl. Sci.*, vol. 9, no. 3110, 2019.
- [5] A. Alanazi and J. Straub, "Engineering Methodology for Student-Driven CubeSats," *Aerospace*, vol. 6, 2019.
- [6] S. Rossi and A. Ivanov, "Thermal model for CubeSat: A Simple and easy model from the SwissCube's thermal flight data," in *64th IAC*, 2013.
- [7] S. J. Kang and H. U. Oh, "On-orbit thermal design and validation of 1 U standardized CubeSat of STEP cube lab," *Int. J. Aerosp. Eng.*, 2016.
- [8] P. Reiss, M. Macdonald, and L. Charlotte, "New methodologies for the thermal modelling of cubesats," in *26th Annual AIAA-USU Conference on Small Satellites*, 2012, no. August.
- [9] M. M. Garzon, "Development and Analysis of the Thermal Design for the Osiris-3U CubeSat," M.Sc Thesis, The Pennsylvania State University, 2012.
- [10] G. F. Fernandes, M. B. Santos, V. D. Silva, J. S. Almeida, and P. R. M. Nogueira, "Thermal Tests for CubeSat in Brazil: Lessons learned and the challenges for the future," in *67th AIC*, 2016.
- [11] J. Friedel and S. Mckibbon, "Senior Project Thermal Analysis of the CubeSat CP3 Satellite," Senior Report, California Polytechnic State University, 2011.
- [12] S. Jos, "THERMAL MODELING OF NANOSAT A Thesis Presented to The Faculty of the Department of Mechanical and Aerospace Engineering," 2012.
- [13] J. Bauer, S. Neu, and T. Shaffer, "Mechanical , Power , and Thermal Subsystem Design for a CubeSat Mission," B.Sc Project, Worcester Polytechnic Institute", 2012.
- [14] J.-R. T. Lee-Her Hu, Ming-Shong Chang, "Thermal Control Design and Analysis for a Picosatellite-YamSat," *Trans. Aeronaut. Astronaut. Soc. Repub. China*2, vol. 35, no. 3, pp. 227–233, 2003.

- [15] J. Yoo *et al.*, “Thermal Analysis of TRIO-CINEMA Mission,” *J. Astron. Sp. Sci.*, vol. 29, no. 1, pp. 23–31, 2012.
- [16] V. Baturkin, “Micro-satellites thermal control - Concepts and components,” *Acta Astronaut.*, vol. 56, no. 1–2, pp. 161–170, 2005.
- [17] C. G. Justus, G. W. Batts, B. J. Anderson, and B. F. James, “Simple Thermal User’s Guide Environment Model (STEM).”, Marshall Space Flight Center, NASA, 2001
- [18] M. Furukawa, “Practical method for calculating radiation incident upon a panel in orbit,” *J. Thermophys. Heat Transf.*, vol. 6, no. 1, pp. 173–177, 1992.
- [19] H. K. Kim and C. Y. Han, “Analytical and numerical approaches of a solar array thermal analysis in a low-earth orbit satellite,” *Adv. Sp. Res.*, vol. 46, no. 11, pp. 1427–1439, 2010.
- [20] J. R. Wertz and W. J. Larson, *Space Mission Analysis and Design*, 3rd Editio. Microcosm Press & Kluwer Academic Publishers, 1999.
- [21] “Wikipedia - Two-line element set.” [Online]. Available: https://en.wikipedia.org/wiki/Two-line_element_set.
- [22] “Celestrak.” Online: www.celestrak.com, .
- [23] H. Maui, “Parametric Characterization of SGP4 Theory and TLE positional accuracy,” in *AMOS SSA Conference*, 2014.
- [24] J. Meeus, *Astronomical Algorithms*, 1st ed. Virginia: Willmann-Bell Inc., 1991.
- [25] “ASTM Solar Spectrum,” *ASTM*. [Online]. Available: <https://www.astm.org/Standards/G173.htm>.
- [26] B. Anderson, C. Justus, and G. Batts, “Guidelines for the selection of near-earth thermal environment parameters for spacecraft design.”, Alabama: Marshall Space Flight Centre, 2001
- [27] R. Peyrou-Lauga, “Using real Earth albedo and Earth IR flux for spacecraft thermal analysis,” in *Proceedings of the 47th International Conference on Environmental Systems*, 2017, no. ICES-2017-142.
- [28] A. J. Juhasz and R. C. Tew, “An analysis and computational procedure for determining space environmental sink temperatures.”
- [29] J. Claricoats and S. M. Dakka, “Design of Power, Propulsion, and Thermal Sub-Systems for a 3U CubeSat Measuring Earth’s Radiation Imbalance,” *Aerospace*, vol. 5, no. 2, p. 63, 2018.
- [30] ASM, “Aerospace Specification Metals Inc.” [Online]. Available: <http://www.aerospacemetals.com/contact-aerospace-metals.html>.

- [31] Renesas, “Thermal Considerations in Package Design and Selection,” Application Note AN-842, Rev A, 2019.
- [32] V. G. A.F Mills, *Heat Transfer*, 2nd Editio. Pearson Education, 2003.
- [33] K. B. Narayana, “View factors for parallel rectangular plates,” *Heat Transf. Eng.*, vol. 19, no. 1, pp. 59–63, 1998.
- [34] H. D. Young, *University Physics*, 7th Editio. Addison Wesley, 1992.
- [35] J. Holman, *Heat Transfer*. McGraw-Hill Kogakusha Ltd, 1976.
- [36] A. K. Ismail, M. Z. Abdullah, A. A. Aljubouri, and J. Abdul Aziz, “Thermal contact resistance for hard and soft mating materials in a vacuum environment,” in *17th International Symposium on Transport Phenomena*, 2006.
- [37] Y. A. Cengel, *Fundamentals of Thermal-Fluid Sciences*. McGraw-Hill, 2012.
- [38] T. R. Ogden, “Thermal conductivity of hard anodized coatings on aluminum,” *AIAA/ASME/SAE/ASEE 23rd Jt. Propuls. Conf. 1987*, 1987.
- [39] R. Grilli, “Conversion coatings for aluminium alloys : a surface investigation for corrosion,” Ph.D Thesis, University of Surrey, 2010.
- [40] J. H. Henninger, “Solar Absorptance and Thermal Emittance of Some Common Spacecraft Thermal Control Coatings,” NASA, 1884.
- [41] J. P. . Lindfield, *Solutions of Differential Equations*, 4th Editio. Academic Press, 2019.
- [42] T. Totani, H. Ogawa, R. Inoue, T. K. Das, M. Wakita, and H. Nagata, “Thermal design procedure for micro-and nanosatellites pointing to earth,” *J. Thermophys. Heat Transf.*, vol. 28, no. 3, pp. 524–533, 2014.
- [43] “Multi-layer Insulation (MLI),” Meyer Tool MFG. Online: <https://www.mtminc.com/multi-layer-insulation.html>.

Appendix A: Thermal node and resistance listing

A-1: Lumped-Capacitance Thermal Nodes

Table 31: Full list of thermal nodes

Identifier	Name	Mass	c_v	k
1	STRUCT_ZM1_1	6.9	0.96	130
2	STRUCT_ZM1_2	6.9	0.96	130
3	STRUCT_ZM1_3	6.9	0.96	130
4	STRUCT_ZM1_4	6.9	0.96	130
5	STRUCT_ZM2_1	6.9	0.96	130
6	STRUCT_ZM2_2	6.9	0.96	130
7	STRUCT_ZM2_3	6.9	0.96	130
8	STRUCT_ZM2_4	6.9	0.96	130
9	STRUCT_ZP1_1	6.9	0.96	130
10	STRUCT_ZP1_2	6.9	0.96	130
11	STRUCT_ZP1_3	6.9	0.96	130
12	STRUCT_ZP1_4	6.9	0.96	130
13	STRUCT_ZP2_1	6.9	0.96	130
14	STRUCT_ZP2_2	6.9	0.96	130
15	STRUCT_ZP2_3	6.9	0.96	130
16	STRUCT_ZP2_4	6.9	0.96	130
17	STRUCT_YP1_1	2.9	0.96	130
18	STRUCT_YP1_2	2.9	0.96	130
19	STRUCT_YM1_1	2.9	0.96	130
20	STRUCT_YM1_2	2.9	0.96	130
21	STRUCT_YP2_1	2.9	0.96	130
22	STRUCT_YP2_2	2.9	0.96	130
23	STRUCT_YM2_1	2.9	0.96	130
24	STRUCT_YM2_2	2.9	0.96	130
25	STRUCT_YP3_1	2.9	0.96	130
26	STRUCT_YP3_2	2.9	0.96	130
27	STRUCT_YM3_1	2.9	0.96	130
28	STRUCT_YM3_2	2.9	0.96	130
29	STRUCT_YP4_1	2.9	0.96	130
30	STRUCT_YP4_2	2.9	0.96	130
31	STRUCT_YM4_1	2.9	0.96	130
32	STRUCT_YM4_2	2.9	0.96	130
33	ROD_YPZM1_1	1	0.5	17.5
34	ROD_YPZM1_2	1	0.5	17.5
35	ROD_YPZM1_3	1	0.5	17.5
36	ROD_YPZM1_4	1	0.5	17.5
37	ROD_YPZM1_5	1	0.5	17.5
38	ROD_YPZM1_6	1	0.5	17.5
39	ROD_YPZM1_7	1	0.5	17.5
40	ROD_YPZM1_8	1	0.5	17.5
41	ROD_YMZM1_1	1	0.5	17.5
42	ROD_YMZM1_2	1	0.5	17.5
43	ROD_YMZM1_3	1	0.5	17.5
44	ROD_YMZM1_4	1	0.5	17.5
45	ROD_YMZM1_5	1	0.5	17.5
46	ROD_YMZM1_6	1	0.5	17.5
47	ROD_YMZM1_7	1	0.5	17.5

Table 31: Full list of thermal nodes (Continued)

Identifier	Name	Mass	c_v	k
48	ROD YMZM1 8	1	0.5	17.5
49	ROD YMZP1 1	1	0.5	17.5
50	ROD YMZP1 2	1	0.5	17.5
51	ROD YMZP1 3	1	0.5	17.5
52	ROD YMZP1 4	1	0.5	17.5
53	ROD YMZP1 5	1	0.5	17.5
54	ROD YMZP1 6	1	0.5	17.5
55	ROD YMZP1 7	1	0.5	17.5
56	ROD YMZP1 8	1	0.5	17.5
57	ROD YPZP1 1	1	0.5	17.5
58	ROD YPZP1 2	1	0.5	17.5
59	ROD YPZP1 3	1	0.5	17.5
60	ROD YPZP1 4	1	0.5	17.5
61	ROD YPZP1 5	1	0.5	17.5
62	ROD YPZP1 6	1	0.5	17.5
63	ROD YPZP1 7	1	0.5	17.5
64	ROD YPZP1 8	1	0.5	17.5
65	ROD YPZM2 1	4	0.5	17.5
66	ROD YPZM2 2	4	0.5	17.5
67	ROD YMZM2 1	4	0.5	17.5
68	ROD YMZM2 2	4	0.5	17.5
69	ROD YMZP2 1	4	0.5	17.5
70	ROD YMZP2 2	4	0.5	17.5
71	ROD YPZP2 1	4	0.5	17.5
72	ROD YPZP2 2	4	0.5	17.5
73	PCB ANT	85	0.95	N/A
74	PCB CMC	80	0.95	N/A
75	PCB EPS	220	0.7	N/A
76	PCB BOB	30	0.95	N/A
77	PCB COMP	60	0.6	N/A
78	PCB COIL	50	0.95	N/A
79	PCB SENSE	80	0.95	N/A
80	PCB CONTROL	165	0.95	N/A
81	PCB GECKO	480	0.95	N/A
82	PCB GRAV	20	0.95	N/A
83	PCB FIPEX	660	0.95	N/A
84	PANEL SOLXM	26	0.95	N/A
85	PANEL SIDEYM 1	4	0.96	130
86	PANEL SIDEYM 2	4	0.96	130
87	PANEL SIDEYM 3	4	0.96	130
88	PANEL SIDEYM 4	4	0.96	130
89	PANEL SIDEYM 5	4	0.96	130
90	PANEL SIDEYM 6	4	0.96	130
91	PANEL SIDEYP 1	4	0.96	130
92	PANEL SIDEYP 2	4	0.96	130
93	PANEL SIDEYP 3	4	0.96	130
94	PANEL SIDEYP 4	4	0.96	130
95	PANEL SIDEYP 5	4	0.96	130
96	PANEL SIDEYP 6	4	0.96	130
97	PANEL SIDEZM 1	64	0.38	109
98	PANEL SIDEZM 2	64	0.38	109
99	PANEL SIDEZM 3	64	0.38	109

Table 31: Full list of thermal nodes (Continued)

Identifier	Name	Mass	c_v	k
100	PANEL_SIDEZM_4	64	0.38	109
101	PANEL_SIDEZM_5	64	0.38	109
102	PANEL_SIDEZM_6	64	0.38	109
103	PANEL_SIDEZP_1	64	0.38	109
104	PANEL_SIDEZP_2	64	0.38	109
105	PANEL_SIDEZP_3	64	0.38	109
106	PANEL_SIDEZP_4	64	0.38	109
107	PANEL_SIDEZP_5	64	0.38	109
108	PANEL_SIDEZP_6	64	0.38	109
109	PANEL_DEPYP	160	0.96	N/A
110	PANEL_DEPYM	160	0.96	N/A

A-2: Lumped-Capacitance Thermal Resistances

Table 32: Full list of thermal resistances in model

Identifier	Node 1	Node 2	R
1	1	2	69.7
2	2	3	38.3
3	3	4	69.7
4	1	4	38.3
5	5	6	69.7
6	6	7	38.3
7	7	8	69.7
8	5	8	38.3
9	9	10	69.7
10	10	11	38.3
11	11	12	69.7
12	9	12	38.3
13	13	14	69.7
14	14	15	38.3
15	15	16	69.7
16	13	16	38.3
17	1	17	0.5
18	2	19	0.5
19	3	23	0.5
20	4	21	0.5
21	5	25	0.5
22	6	27	0.5
23	7	31	0.5
24	8	29	0.5
25	9	18	0.5
26	10	20	0.5
27	11	24	0.5
28	12	22	0.5
29	13	26	0.5
30	14	28	0.5
31	15	32	0.5
32	16	30	0.5
33	17	18	54.4
34	19	20	54.4

Table 32: Full list of thermal resistances in model (Continued)

Identifier	Node 1	Node 2	R
35	21	22	54.4
36	23	24	54.4
37	25	26	54.4
38	27	28	54.4
39	29	30	54.4
40	31	32	54.4
41	29	33	1
42	33	34	5.5
43	34	35	7.8
44	35	36	3.5
45	36	37	5
46	37	38	2.6
47	38	39	2.6
48	39	40	2.9
49	25	40	32.5
50	31	41	1
51	41	42	5.5
52	42	43	7.8
53	43	44	3.5
54	44	45	5
55	45	46	2.6
56	46	47	2.6
57	47	48	2.9
58	27	48	32.5
59	32	49	1
60	49	50	5.5
61	50	51	7.8
62	51	52	3.5
63	52	53	5
64	53	54	2.6
65	54	55	2.6
66	55	59	2.9
67	56	28	32.5
68	30	57	1
69	57	58	5.5
70	58	59	7.8
71	59	60	3.5
72	60	61	5
73	61	62	2.6
74	62	63	2.6
75	63	64	2.9
76	26	64	32.5
77	21	65	15.9
78	65	66	32.7
79	17	66	13.5
80	23	67	17.1
81	67	68	33.7
82	19	68	14.9
83	24	69	17.8
84	69	70	34.7
85	20	70	15.6
86	22	71	16.8

Table 32: Full list of thermal resistances in model (Continued)

Identifier	Node 1	Node 2	R
87	71	72	35.7
88	18	72	14.4
89	33	73	100
90	41	73	100
91	49	73	100
92	57	73	100
93	73	74	400
94	34	74	100
95	42	74	100
96	50	74	100
97	58	74	100
98	74	75	400
99	35	75	80
100	43	75	80
101	51	75	80
102	59	75	80
103	75	76	400
104	36	76	100
105	44	76	100
106	52	76	100
107	60	76	100
108	76	77	400
109	37	77	50
110	45	77	50
111	53	77	50
112	60	77	50
113	77	78	400
114	38	78	100
115	46	78	100
116	54	78	100
117	61	78	100
118	78	79	200
119	39	79	100
120	47	79	100
121	55	79	100
122	62	79	100
123	79	80	200
124	40	80	100
125	48	80	100
126	56	80	100
127	63	80	100
128	65	81	50
129	67	81	50
130	69	81	50
131	71	81	50
132	66	82	100
133	68	82	100
134	70	82	100
135	72	82	100
136	17	83	60
137	18	83	60
138	19	83	60

Table 32: Full list of thermal resistances in model (Continued)

Identifier	Node 1	Node 2	R
139	20	83	60
140	29	84	40
141	30	84	40
142	31	84	40
143	32	84	40
144	32	85	0.5
145	31	86	0.5
146	24	87	0.5
147	28	87	0.5
148	23	88	0.5
149	27	88	0.5
150	20	89	0.5
151	19	90	0.5
152	85	86	3.9
153	85	87	3.9
154	86	88	3.9
155	87	88	3.9
156	87	89	3.9
157	88	90	3.9
158	89	90	3.9
159	30	91	0.5
160	29	92	0.5
161	22	93	0.5
162	26	93	0.5
163	21	94	0.5
164	25	94	0.5
165	18	95	0.5
166	17	96	0.5
167	91	92	3.9
168	91	93	3.9
169	92	94	3.9
170	93	94	3.9
171	93	95	3.9
172	94	96	3.9
173	95	96	3.9
174	2	97	0.5
175	1	98	0.5
176	3	99	0.5
177	6	99	0.5
178	4	100	0.5
179	5	100	0.5
180	7	101	0.5
181	8	102	0.5
182	97	98	5.1
183	97	99	5.1
184	98	100	5.1
185	99	100	5.1
186	99	101	5.1
187	100	102	5.1
188	101	102	5.1
189	102	103	0.5
190	9	104	0.5

Table 32: Full list of thermal resistances in model (Continued)

191	11	105	0.5
192	14	105	0.5
193	12	106	0.5
194	13	106	0.5
195	15	107	0.5
196	16	108	0.5
197	103	104	5.1
198	103	105	5.1
199	104	106	5.1
200	105	106	5.1
201	105	107	5.1
202	106	108	5.1
203	107	108	5.1
204	109	96	60
205	109	94	30
206	109	92	60
207	110	90	60
208	110	88	30
209	110	86	60
210	111	112	120
211	112	101	90

A-3: Surface Model

Surface Member	Connected Node	Area	e	a	CoP X	CoP Y	CoP Z	n X	n Y	n Z	V0 X	V0 Y	V0 Z	V1 X	V1 Y	V1 Z	V2 X	V2 Y	V2 Z
zm0	97	3500	0.8	0.8	35	25	50	0	0	1	0	0	50	70	0	50	70	50	50
zm1	98	3500	0.8	0.8	35	-25	50	0	0	1	0	-50	50	70	-50	50	70	0	50
zm2	99	3500	0.8	0.8	105	25	50	0	0	1	70	50	50	70	0	50	140	0	50
zm3	100	3500	0.8	0.8	105	-25	50	0	0	1	70	-50	50	140	-50	50	140	0	50
zm4	101	3500	0.8	0.8	175	25	50	0	0	1	140	50	50	140	0	50	210	0	50
zm5	102	3500	0.8	0.8	175	-25	50	0	0	1	140	-50	50	210	-50	50	210	0	50
ym0	90	3500	0.8	0.8	35	50	25	0	1	0	0	50	50	70	50	50	70	50	0
ym1	89	3500	0.8	0.8	35	50	-25	0	1	0	0	50	-50	0	50	0	70	50	0
ym2	88	3500	0.8	0.8	105	50	25	0	1	0	70	50	50	140	50	50	140	50	0
ym3	87	3500	0.8	0.8	105	50	-25	0	1	0	70	50	-50	70	50	0	140	50	0
ym4	86	3500	0.8	0.8	175	50	25	0	1	0	140	50	50	210	50	50	210	50	0
ym5	85	3500	0.8	0.8	175	50	-25	0	1	0	140	50	-50	140	50	0	210	50	0
zp0	103	3500	0.8	0.8	35	25	-50	0	0	-1	0	0	-50	0	50	-50	70	50	-50
zp1	104	3500	0.8	0.8	35	-25	-50	0	0	-1	0	0	-50	70	0	-50	70	-50	-50
zp2	105	3500	0.8	0.8	105	25	-50	0	0	-1	70	0	-50	70	50	-50	140	50	-50
zp3	106	3500	0.8	0.8	105	-25	-50	0	0	-1	70	0	-50	140	0	-50	140	-50	-50
zp4	107	3500	0.8	0.8	175	25	-50	0	0	-1	140	0	-50	140	50	-50	210	50	-50
zp5	108	3500	0.8	0.8	175	-25	-50	0	0	-1	140	0	-50	210	0	-50	210	-50	-50
yp0	96	3500	0.8	0.8	35	-50	25	0	-1	0	0	-50	0	70	-50	0	70	-50	50
yp1	95	3500	0.8	0.8	35	-50	-25	0	-1	0	0	-50	-50	70	-50	-50	70	-50	0
yp2	94	3500	0.8	0.8	105	-50	25	0	-1	0	70	-50	50	70	-50	0	140	-50	0
yp3	93	3500	0.8	0.8	105	-50	-25	0	-1	0	70	-50	-50	140	-50	-50	140	-50	0
yp4	92	3500	0.8	0.8	175	-50	25	0	-1	0	140	-50	50	140	-50	0	210	-50	0
yp5	91	3500	0.8	0.8	175	-50	-25	0	-1	0	140	-50	-50	210	-50	-50	210	-50	0
xp0	83	10000	0.8	0.8	0	0	0	-1	0	0	0	-50	50	0	50	50	0	50	-50
xm0	84	10000	0.8	0.8	210	0	0	1	0	0	210	-50	50	210	-50	-50	210	50	-50

Figure 83: Screenshot of surface builder data editor

Appendix B: Datasheet Extracts

B-1: GomSpace Nanopower P31U Datasheet

Table 33: P31U Electrical Characteristics

Parameter	Condition	Min.	Typ.	Max.	Unit
Battery					
- Voltage	Battery connection 2 cells in series	6.0	7.40	8.40	V
	Battery connection 4 cells in series	(*12.0)	(*14.9)	(*16.80)	V
- UVD	Under voltage detection		1600		us
- Current, charge	(Depends on battery configuration)				A
- Current, discharge	Overcurrent protection threshold ***		4***	6.00	A
- OCD (I_Sys)	Over current detection	1	580****	1400	us
PV inputs					
- Voltage	Photo-voltaic inputs (Customer selectable)	0	4.2	8.5	V
		(*0)	(*8.4)	(*17)	V
- Current, charge		0.00		2.00	A
Charge Pin					
- Voltage	Battery charge input 5 V => 0.9 A charge, 4 V => 0 A	4.10	5.00	5.00	V
- Current, cont	@5 V		0.9	1.1	A
OUT-1,2,3,4,5,6					
- Voltage	Latch-up protected outputs Configurable		3.3/4.98		V
- Current limit	Current cut-off limit (Cust. select)	0.5	Select	2.5	A
+5 V					
- Voltage	5 V regulated output (always on)	4.89	4.98	5.05	V
- Current, cont. **	Total current including output channels	0.005		4.00	A
+3.3 V					
- Voltage	3.3 V regulated output (always on)	3.29	3.34	3.39	V
- Current, cont.	Total current including output channels	0		5.00	A
V_BAT					
- Voltage	Raw battery voltage (Depends on battery configuration)	6.0		8.40	V
		(*12.15)		(*16.80)	V
- Current out			4		A
Power consumption	Power consumed by P31u		160		mW
			(*260)		mW
Off current	Current consumed with separation switch OFF		35	60	μA
Shell-life	Period until batteries are fully discharged when separation switch is OFF. (Depends on battery configuration)	700	1400		Days

Table 34: P31U Physical Characteristics

P31u with battery

Description	Value	Unit
Mass (With high stack connector)	200	g
Size	89.3 x 92.9 x 25.6	mm

P31u without battery

Description	Value	Unit
Mass (With low stack connector)	100	g
Size	89.3 x 92.9 x 15.3	mm

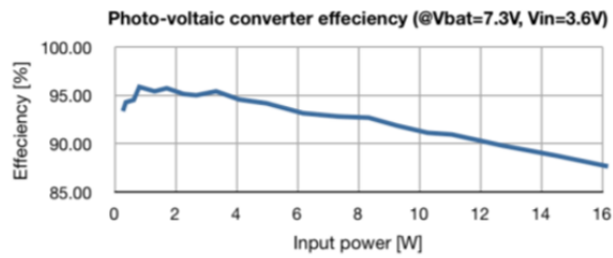


Figure 84: P31U PV converter efficiency

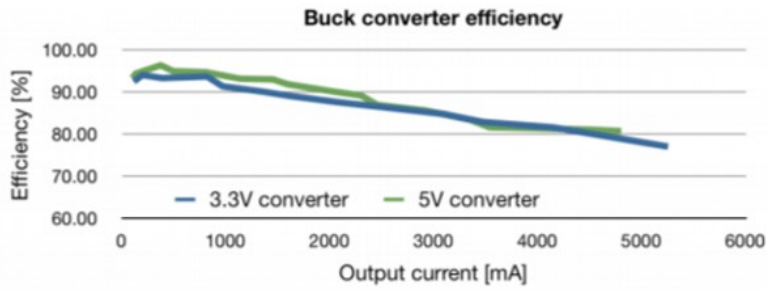


Figure 85: P31U Buck converter efficiency

B-2: GomSpace Battery Datasheet

Table 35: GomSpace Battery Specifications

Parameter	Condition	Min.	Typ.	Max	Unit
Voltage		3.0	3.7	4.2	V
Current - Charge	0 – +45 °C		1000	2500	mA
Current - Discharge	-20 – +5 °C +5 – +60 °C		1000	1250 3750	mA mA
Temperature - Storage	80% recovery after: 3 months 12 months	-20 -20		45 20	°C °C
Temperature - Operating	Charge Discharge	0 -20		45 60	°C °C
Internal impedance				70	mΩ
Cycle Life (20% capacity loss)	DOD: 100%, Temp 25°C Charge/discharge: 1C/1C		350		cycles

Mass: 48 g

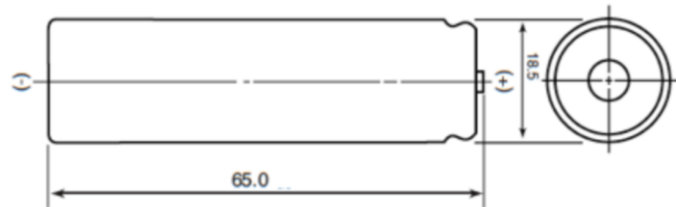


Figure 86: GomSpace Battery Physical Dimensions

B-3: GomSpace Solar Panel Datasheet

Table 36: P110 series physical specifications

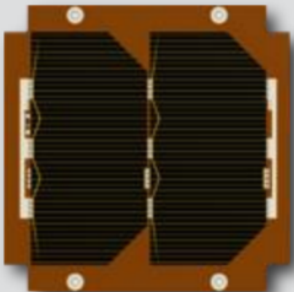
Panel Models		
<p>P110A 2 pcs. 3G30A SCA Blocking diode Coarse Sun sensor Temperature sensor Mass: 26 g PCB thickness: 1.1 mm</p>	<p>P110UA 2 pcs. 3G30A SCA Blocking diode Magnetorquer Coarse Sun sensor Temperature sensor Mass: 57 g PCB thickness: 1.6 mm</p>	
<p>P110B 2 pcs. 3G30A SCA Blocking diode Coarse Sun sensor Temperature sensor Mass: 26 g PCB thickness: 1.1 mm</p>	<p>P110UB 2 pcs. 3G30A SCA Blocking diode Magnetorquer Coarse Sun sensor Temperature sensor Mass: 57 g PCB thickness: 1.6 mm</p>	
<p>P110C 2 pcs. 3G30A SCA Blocking diode Coarse Sun sensor Temperature sensor Mass: 29 g PCB thickness: 1.1 mm</p>	<p>P110UC 2 pcs. 3G30A SCA Blocking diode Magnetorquer Coarse Sun sensor Temperature sensor Mass: 65 g PCB thickness: 1.6 mm</p>	

Table 37: P31U Electrical Characteristics

Parameter	Condition	Min	Typ	Max	Unit
Solar Cell string <ul style="list-style-type: none"> Voltage Current Power Efficiency 	Full sunlight in LEO Optimal voltage Current at optimal voltage Maximum power	4.64 490 2270 29.8	30	4.84 508 2400 30.2	V mA mW %
Course Sun Sensor Current Cosine error	Short current at 1367 W/m ²		930 1.85	3.5	μA °
Temperature Sensor <ul style="list-style-type: none"> Range Resolution Vcc Current Temperature coefficient 		-55 1.5 0.21	3.3 260 0.233	+150 3.5 490 0.25	°C °C V μA %/°C
Magnetorquer <ul style="list-style-type: none"> Area Resistance Current Dipole momentum 	Absolute maximum rating Dipole momentum at 3.3 V	120 0.034	1.55 135 0.038	150 1 0.043	m ² Ω A A m ²

B-4: QIOptic Cover glass Datasheet

Table 38: QIOptic Cover glass transmission specifications

Minimum Coverglass Transmission specifications with 0.10mm thick CMX, CMG and CMO glass types

		350 - 400nm	400 - 450nm	450 - 700nm	600 - 800nm	650 - 900nm	450 - 1100nm	900 - 1800nm	IR Cut-off	Min Emittance	Front Surface Resistance
CMX	Uncoated	73.5	91.5	94.0	95.0	95.0	95.0	95.0		0.88	
CMG		83.5	92.5	94.5	95.0	95.0	95.0	95.0		0.88	
CMO		88.0	94.0	94.5	95.0	95.0	95.0	95.0		0.88	
CMX	AR	73.5	93.0	96.5	97.5	97.5	96.5	96.5		0.88	
CMG		83.5	94.0	97.0	97.5	97.5	96.5	96.5		0.88	
CMO		88.0	95.5	97.0	97.5	97.5	96.5	96.5		0.88	
CMX	Conductive	73.5	94.0	96.5	97.0	97.0	96.5	96.0		0.86	<10M Ohms
CMG	AR	83.5	95.0	97.0	97.0	97.0	96.5	96.0		0.86	<10M Ohms
CMO		88.0	96.0	97.0	97.0	97.0	96.5	96.0		0.86	<10M Ohms
CMX	Conductive	71.0	89.0	94.0	95.0	95.0	94.5	94.5		0.84	<5K Ohms
CMG		80.0	89.0	94.0	95.0	95.0	94.5	94.5		0.84	<5K Ohms
CMO		80.0	89.0	94.0	95.0	95.0	94.5	94.5		0.84	<5K Ohms
CMX	UV Reflector	73.5	92.0	96.0	96.5	96.5	96.0	94.0		0.86	
CMG		83.5	93.0	96.5	96.5	96.5	96.0	94.0		0.86	
CMO		88.0	94.5	96.5	96.5	96.5	96.0	94.0		0.86	
CMX	AR/IRR Silicon	73.5	89.0	96.0	96.0	96.0	95.0		1165+/-	0.86	
CMG	Blue Red Silicon	83.5	90.0	96.0	96.0	96.0	95.0		50nm	0.86	
CMO		88.0	92.0	96.0	96.0	96.0	95.0			0.86	
CMX	UVR/IRR	73.5	92.0	96.5	96.5	96.5	95.0		1315+/-	0.86	
CMG	Triple Junction	83.5	93.0	96.5	96.5	96.5	95.0		35nm	0.86	
CMO	(PS 703)	88.0	88.0	96.5	96.5	96.5	95.0			0.86	